

https://dspace.org/

Evaluation of radiation detector systems for mammography x-ray units

Mavunda, Risimati Dazmen

2009-03-25T08:48:38Z
http://hdl.handle.net/10539/6793

Downloaded from a DSpace repository. https://dspace.org/

Chapter 1

GENERAL INTRODUCTION

1.1 Historical background

The report of an estimated 400600 deaths from breast cancer; the world Health Organization's prediction of more than 1.2 million new breast cancer cases globally; the report of breast cancer as the second highest cause of cancer deaths in women (after lung cancer) (Globacan, 2000**)**, and an observation that X-ray mammography screening may induce breast cancer (Denotter et al., 1996) has changed the World wide focus on cancer today and necessitates an urgent study on the available diagnostic and monitoring tools.

Early diagnosis of breast cancer play a leading role in improving the patient's prognosis, and, with proper management, would reduce the mortality rate (Siemen, 2004). Analysis of the physical characteristics of the tools available for screening protocols, having in mind the risk versus benefit, is imperative for overcoming the limitations of the screen film mammography such as, dynamic range, contrast and lack of convenient options for post-processing of images (Albagli et al., 2000). These needs, coupled with the optimization of breast cancer screening protocols and risk versus benefits, were analyzed (Jansen et al., 1997)

In newly developed mammography X-ray units, the detector materials with high atomic number where the photoelectric effect is the dominant type of X-ray interaction are still being used (Yaffe et al., 1997). Due to the thickness and high atomic number of the phosphor material, the energy resulting in low conversion efficiency and high scatter radiation, it is suspected, may induce cancer (Land, 1980).

As mammography is considered to be the most important method for the diagnosis of breast cancer, and that a screening program would decrease the mortality rate of breast cancer patients (Schmidt et al., 1995). The accuracy and sensitivity of a mammography X-ray unit must be high in determining breast cancer (Gregoire et al., 1992). The screening procedures to be employed must be simple, acceptable, of reasonable cost and the sensitivity must be adequate (Dodd, 1993).

Amongst the modalities that have been used for the detection of breast cancer are: - Magnetic Resonance (Kaiser, 1993, Umschaden et al., 1997), Ultrasound (Vanoord et al., 1991), Nuclear Medicine applied Single Photon Emission Computerised Tomography (SPECT) technique, where gamma cameras are used (Hess et al., 1994, DeVincentis et al., 1997 and Prats et al., 1999), Dual Energy Subtraction Mammography (Asaga et al., 1995) and Digital Mammography (Nawano, 1995, Bazzocchi et al., 1998). These modalities however cannot be used for routine breast screening due to limitations of cost and time.

1.2 X-ray mammography technique

Mammography is a radiographic technique that uses X-rays produced from molybdenum, rhodium or tungsten or a combination of any two of them as anode or target materials with an exit window of beryllium or glass. Some older machines have only glass as exit window.

The mammography X-ray beam is generated when high velocity electrons from the cathode collide with the target or anode material. Only one percent of the energy of the streams of electrons is transformed directly into X-ray energy production, bremsstrahlung and characteristic X-rays. The remaining ninety-nine percent of the energy of the electrons is converted into heat and dissipated away. To avoid excessive heat at one point of the anode material surface and cause irreparable damage to the anode material, most modern mammography machines have rotating anodes. The X-ray tube is mounted on tube housing which provides mechanical support and also serves as a container to store oil used to cool the anode during operation. The mammography machine is designed such that the generated X-ray beam is directed through a window by a primary beam and then passed through a filter.

A filter is a material inserted in the X-ray beam to alter the quality of the beam by removing unwanted energy which does not contribute to image information but increases patients radiation dose. The filter material commonly used in mammography is molybdenum, rhodium and aluminium. The filtered beam is collimated to desired dimensions for patient imaging.

Xeromammography is hardly used for mammography imaging whilst screen-film mammography is most commonly used for screening and diagnosis of breast cancer. Screening involves the examination of asymptomatic women with the aim of detecting an early stage lesion before it becomes palpable. Diagnostic mammography on the other

hand is done on women who, through physical findings or symptoms, may show that they are considered to already have breast cancer.

1.2.1 Xeromammography unit and the screen film unit

While xeromammography units employ tungsten as target or anode and aluminium as filter material, screen-film mammography consists of a molybdenum target and a molybdenum filter usually of thickness 4 μm.

Again while xeromammography techniques are usually operated at peak kilo-voltage (kVp) ranging between 40 and 55 kVp, tube current of 30 mA and image receptor made of a thin sheet of photo-conducting amorphous selenium, (a vitreous material, glass-like with the atoms in random positions); with the X-ray images of the breast recorded on uniformly charged selenium plate held in light proof cassette. The selenium plate is developed by use of a fine dust medium on the plate itself. This image is then transferred to a more permanent medium before the selenium plate is reused. The screen film has its X-ray image recorded on a film cassette that consists of a single fluorescent high-detail intensity screen in close proximity with a single-emulsion film.

1.2.2 X-ray mammography requirements

The usual operating voltage of an X-ray mammography unit is 25 to 32 kVp but the unit used in this work operates at lower kilo-voltage peaks of 22 to 40 kVp. With the molybdenum target, the mammography X-ray beam consists of bremsstrahlung and a

significant component of molybdenum characteristic X-ray photons between 17.5 and 19.5 keV (c.*f*. Fig 1.1 and Fig. 1.2).

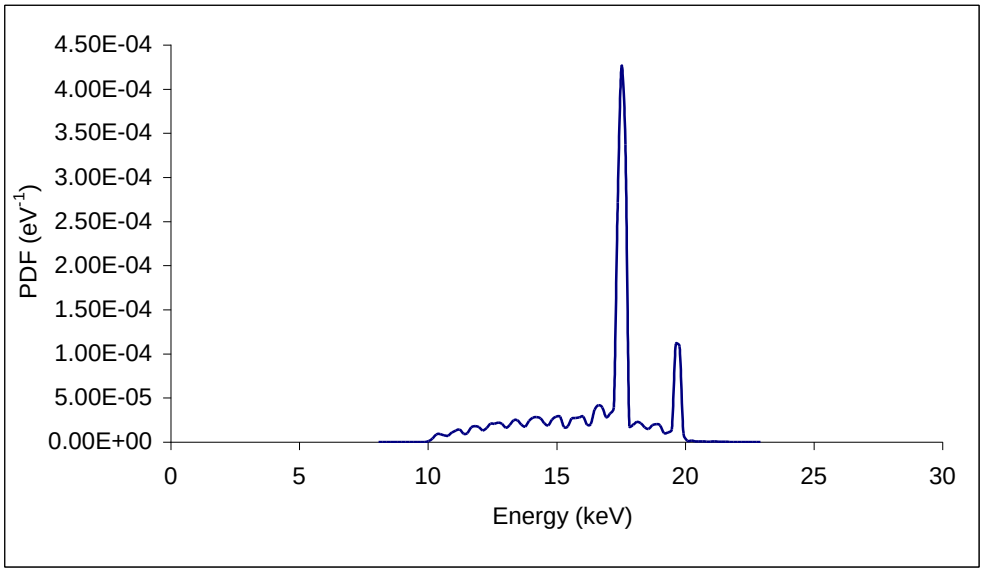


Figure 1.1: PENELOPE simulated X-ray spectrum from a molybdenum target at 22 keV (for details refer to Chapter6)

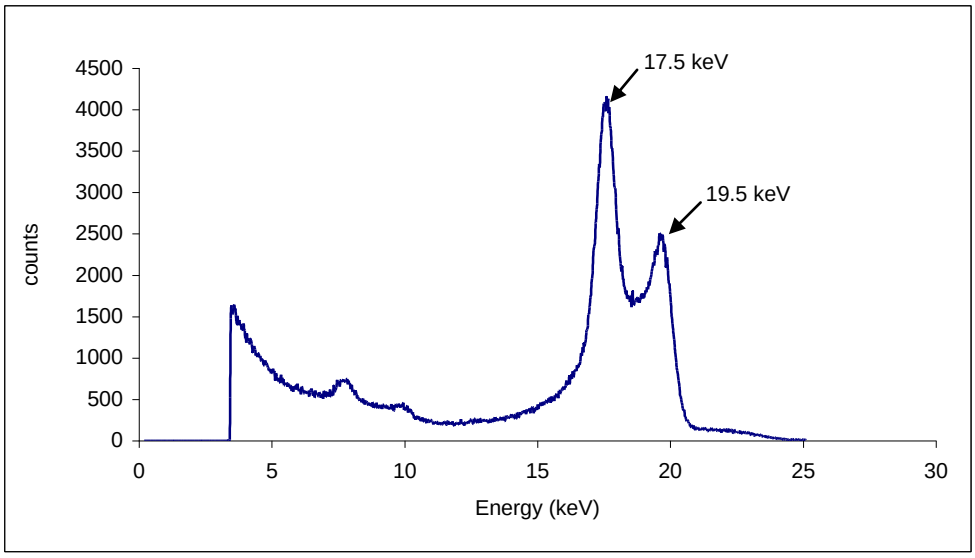


Figure 1.2: X-ray spectrum from a molybdenum target at 25 keV acquired using germanium detector (for detail refer to Chapter 4)

The production of high-contrast, high resolution and low noise images with the lowest radiation dose possible is the goal of mammography for a clinically useful information. Several investigations were carried out for the optimization and improvement of the mammography techniques (Fahrig, 1994, Yaffe, 1997, Lado et al., 1997, Bhat et al., 1998a, Bhat et al., 1998b, Anastasio et al., 1998 and Kallergi et al., 1999). Dose and image quality in mammography studies was conducted (Young et al., 1996), a review of mammography techniques and evaluation of real cost and benefits ratios was also carried out (Simonetti et al., 1998) and concluded that conventional mammography remains the most sensitive tool for breast cancer diagnosis.

In previous exposure investigations using conventional mammography in routine screening for breast malignancy, some theoretical assumptions have been made. Examples are found in areas such as: - simulation of the X-ray spectra (Johnson et al., 1980); simulation of the differential beam hardening effect of filters (Lee, 1997); optimization of spectral shapes (Fahrig et al., 1994), and simulation of the detector response to photon energy (Chen et al., 1980). The anode spectral model using interpolating polynomials of the target material has been found important when calculating X-ray dose to the tissue (Boone et al., 1997). Compilation of individual photon interaction processes is described (Hubbell, 1999a, Hubbell, 1999b and Berger et al., 1987).

Conventionally, breast screening is achieved by detecting the contrasting light intensity that is proportional to the interacting photon intensity. This is achieved with a fluorescent

screen that is an integral component in a cassette that holds a recording film or by using digital techniques (silicon as detector material, coupled to a computer). These detector/recording materials have limitations such as low radiation stability, are chemically reactive, have to operate at low temperature and have low radiation sensitivity.

1.3 Theory of ionization and X-ray sources

Ionization is the process through which an orbital electron is ejected out of its orbit (Lederer and Shirley, 1978). This process can be caused by both charged particles (electrons, protons and alpha particles or uncharged photon (X-rays and gamma)) and uncharged neutron particles. X-rays are produced when a rapid moving electron strikes a solid target and its kinetic energy is converted into radiations whose wavelengths are dependent on the energy of the incident electron. An electron which is removed from one of the inner shells of the atom (target) is replaced by an electron from an outer shell and energy (photon) equal to the difference in binding energies between the two shells is released. The energy (photon) released has exact characteristic value of the element (target) hence the photon emitted is called characteristic X-rays (radiation). X-rays are emitted mostly by heavy elements like molybdenum, tungsten etc (Sorenson, 1938).

1.3.1 A review of X-ray interaction with matter

X-rays (like gamma rays) are electromagnetic ionizing radiations with wavelength range from 10^{-9} m to 10^{-11} m (i.e., 1 keV to in excess of 100 keV**).** There are a number of possible interactions of X-rays or photons with matter such as photoelectric absorption,

Coherent or Rayleigh scattering, incoherent or Compton scattering, Pair production and photonuclear interactions. The important radiation interactions in radiation measurements, which lead to partial or complete transfer of photon energy to electron energy which consequently imparts energy into matter, are photoelectric absorption, Compton scattering and pair production. Rayleigh scattering is an elastic scattering and involves the redirection of photon through a small angle with no energy loss. When the photon energy is in excess of a few MeV, the photonuclear interaction becomes significant (Attix, 1986). The energy of the incident photon and the physical properties of the target material such as atomic number, Z, and density determine the kinetics and the interaction probability or interaction coefficients during photon interaction with matter.

1.3.2 Alpha particle properties and sources

Alpha particles are positively charged ionizing radiation consisting of helium nuclei (two protons and two neutrons) and emitted from the nucleus of an unstable element. They are a highly ionizing form of particle radiation and have low penetration. The α-particle mass is 6.644657×10^{-27} kg. Because of their charge and large mass, α-particles are easily absorbed by materials and can travel only a few centimeters in air. They can be absorbed by tissue paper or the layers of the human skin (about 30 μm). Some of the alpha emitters are Polonium-210 and Americium-241.

1.3.3 Review of alpha particle interaction with matter

High-energy charged particles such as α-particles, loose energy (only about 0.5 % of their emitted energy is lost for each collision) and slow down as they pass through matter as a consequence of collisions with atoms and molecules. Energy is transferred to the

absorbing matter in the process, with the principal result of ionization and excitation of atoms and molecules. Most of this energy ultimately is degraded into heat (atomic and molecular vibrations). The ionization effect is the underlying mechanism for most radiation detectors. The collision that occurs between charged particles and atoms or molecules involves electrical forces of attraction or repulsion rather than actual mechanical content. A less close encounter between a charged particle and an atom may result in an orbital electron being raised to an excited state which results in small energy losses dissipated as molecular vibrations, atomic emission of infrared, visible or UV radiation etc. Such collision losses caused by ionization and excitation are different from the radiation losses which are due to bremsstrahlung production when the heavy charged α-particle penetrates the orbital electron and collides with the nucleus. Such losses are usually very small for α-particle interactions because bremsstrahlung production is inversely proportional to the mass of the incident charged particle. The charged particle track in soft tissues and materials of similar density are typically about 100 μm (Sorenson, 1938).

The increase in use of radiation as clinical diagnostic tool coupled with the need for improved monitoring of the radiation beam to allow greater control of each treatment protocol is the ab-initio motivation of this study.

1.4 Semiconductor for radiation detectors

Researchers have performed investigations on a number of semiconductor materials as radiation detectors. It has been demonstrated that semiconductors with a significant band-

gap (e.g., greater than 1.5 eV) could reduce the bulk-generated leakage current so that use at room temperature would be possible (Knoll, 1989). Semiconductors such as Si, Ge, CaTe, GaAs and Bi_2S_3, which have band-gaps of 1.12 eV, 0.74 eV, 1.47 eV, 1.42 eV and 1.3 eV respectively, cannot be operated at room temperature. In comparison PbI_2, GaSe, AlSb, CdSe, HgI_2 and diamond have band-gaps of 2.6 eV, 2.03 eV, 1.62 eV, 1.75 eV, 2.13 eV and 5.5 eV respectively, and are suitable therefore for operation at room temperature (Knoll, 1989). Most high-Z semiconductor materials with wide band-gaps that are suitable for operation at room temperature unfortunately tend to have low mobility (particularly for holes) compared with silicon and germanium (Knoll, 1989). It has been indicated that germanium and silicon detectors must always be operated at low temperature to reduce thermally generated leakage current (Knoll, 1989). A disadvantage of the use of some cadmium telluride (CaTe) detectors is the phenomenon of polarization. This leads, under certain conditions of operation, to a time-dependent decrease in the counting rate and charge collection efficiency (Bell et al., 1974, Malm et al., 1974, Siffert et al., 1976). With mercuric iodide (HgI_2) at room temperature operation, the preamplifier shows an increase in the full width at half maximum (FWHM) because of the added contribution of thermally generated electronic noise (Knoll, 1989); thus decreasing the resolution. Israel et al. (1971) define resolution as the FWHM and given in terms of keV. They indicated that the line width is proportional to the average energy required to produce an ion pair i.e., 2.8, 3.2, 22, and 500 eV in germanium, silicon, xenon, and sodium iodide, respectively. Gallium arsenide (GaAs) has the limitation of having only available high-purity crystals of less than 1mm-thickness and exhibit experimental problems with abnormal leakage currents and intermittent burst noise (Knoll, 1989).

Armantrout et al. (1977) indicated that most compounds lack the availability in practical crystal sizes. Diamond, by comparison, is an insulating material with a very large band-gap (5.6 eV) and can be operated as a simple conduction counter by applying ohmic contacts to opposite faces of the crystal (Knoll, 1989). Type IIa diamond radiation detectors have low sensitivity to visible light owing to the wide band-gap (Tanaka et al., 2001). A synthetic type IIa diamond single crystal has a suppressing polarization phenomenon (Kaneko et al., 1999), which suppresses an increase in leakage current of the detectors (Tanaka et al., 2001). In addition, diamond has radiation hardness i.e. it cannot be easily damaged by radiation, high thermal conductivity (2000 $Wm^{-1}.K^{-1}$), high electrical resistivity (>10^{12} Ω.cm), high breakdown field (10^7 $V.cm^{-1}$), lower dielectric constant (5.7), electron mobility of 1800 $cm^2.V^{-1}.s^{-1}$, hole mobility of 1200 $cm^2.V^{-1}.s^{-1}$, carrier saturation of 220 $\mu m.ns^{-1}$, energy to create an e-h pair of 13.2 eV and mass density of 3.5 $g.cm^{-3}$ (Zhang et al., 2004).

1.5 Classification of diamonds

Natural diamond is classified into four types, i.e. Ia, Ib, IIa and IIb. Type IIa refers to as pure stones with the nitrogen impurity level ~1 ppm and cannot be optically detected by infra-red light (IR). In type IIb diamond, boron is the dominant impurity and shows semiconductor properties caused by the presence of uncompensated single substitutional boron receptor ($\left(B_s^0\right)$. In contrast, type, Ia, Ib, and IIa crystals exhibit no measurable conductivity at ambient conditions (Iakoubovskii and Stesmanns 2002). CVD diamond appears distinct from other types of diamond in that it exhibits significant concentrations of bulk impurities/defects involving hydrogen, silicon, nitrogen and tungsten

(Iakoubovskii and Stesmanns 2002). Defects can appear in different forms in CVD diamond crystal such as:

- Point defect : the Schottky defect where an atom is missing from a lattice site and takes a normal position at a surface of the lattice site and the Frenkle defect where an atom moves away from a lattice and assumes a position between the lattice sites
- Line defects extend over substantially larger than the atom spacing and are generally important factors in the electrical behaviour of semiconductor devices since they influence trapping and scattering sites in the lattice
- Edge dislocation corresponds to an extra plane inserted orthogonal to the growth direction of a crystal
- Screw dislocation are from an extra plane of an atoms appearing at the surface
- The last line defect appear when there is defacing of the arrangement of the lattice atoms which form a boundary
- Stacking faults results when an extra, small area plane (platelet) of atoms occurs within the larger crystal
- Grain boundaries appear when two growing microcrystal with different crystallographic orientations merge, leaving a line of defects along the plane separating the two crystalline lattices

During crystal growth of CVD diamond, impurities are incorporated into the semiconductor crystal lattice unintentionally replacing carbon atoms at lattice sites and are called substitutional impurities such as H, O, N and Si. Those introduced intentionally (dopends) are Li, B, S and P. Dangling bond are found at defect/impurity sits leading to

degradation in the performance of CVD diamond as detector, hence careful growth and fabrication conditions is important to minimize degradations to occur (Tewksbury, 1995).

1.6 Diamond detectors

The history of diamond detector dates back to 1940's when attempts were made to develop pulse-counting crystals. Diamond has properties most suited for pulse counting detection (Van Heerden, 1954). In 1947 Wooldridge detected α-particles using a diamond in pulse counting mode, whilst Curtiss and Brown (1947) detected γ-radiation with a pulse counting diamond detector. Other researchers describing pulse counting diamond radiation detectors are: Wouters and Christian (1947), McKay (1948), Hofstandedter (1948, 1949), Willardson and Danielson (1950), Cotty (1956), Champion and Wright (1957), Kennedy (1959), Urlau (1960) and Vermeulen (1965). These researchers experienced problems with the selection of pulse counting diamonds. Curtiss and Brown (1947) reported that only two diamonds types were able to detect γ-rays. The result of identifying specific diamond was to identify the defects and impurities and remove the cause of space charge (Fallon et al., 1990 and 1992). The first space charge free pulse counting diamond detector was reported by Konorova and Kozlov (1971). They claimed that the removal of the space charge effect by creating a 'hole injection' contact enabled the detection of α-particles with a good energy resolution. It is known that, saturation of irradiation-induced current in diamond (Konorova et al., 1966) can be due to complete charge collection and decrease of charge carrier mobility in high electric field (Konorova et al., 1967). In 1977 Kozlov et al. performed a study using diamond detector immersed in an alpha emitting solution. A good linear response and high

stability was demonstrated. Nava et al. (1979) demonstrated the transport properties of natural diamond when used as nuclear particle detector over a wide temperature range.

Charge carriers freed by radiation interactions can be trapped at trapping centers in the diamond, and are released if the diamond is heated. The released charge carriers can combine at luminescent centers in the diamond, producing light (thermoluminescence) when the diamond is heated. The emitted light is a measure of the amount of radiation, which was incident on the diamond (Eliseev et al., 1988, Nam 1987, Nam et al., 1991). Ionization by interacting radiation increases the electrical conductance of diamond, and can be measured by placing diamond in a simple direct current resistance measuring circuit (Kozlov et al., 1977, Burgemeister 1982, Keddy et al., 1987). Kovalchuk et al. (1994) indicated that, diamond detectors have characteristics as a neutron spectrometer and have some advantages over a silicon detector. Araikum (1993) demonstrated photo-excitation and photo-stimulated luminescence properties of diamonds, which were synthesized primarily for thermoluminescence dosimetry.

The production of the CVD synthetic diamonds with controlled amount of impurities, reproducible, and with improved carrier life-time, provides the impetus to characterize the properties needed to fabricate detectors with the required performance characteristics. Synthetic Chemical Vapour Deposition (CVD) diamond detectors have been used for different applications. It has been noted that a diamond radiation detector has several merits (Tanaka et al., 2001), in terms of high temperature (Nava et al., 1979), high radiation resistance (Kozlov et al., 1975) and high chemical resistance (Kozlov et al.,

1977). The principle of synthesis of CVD diamond detectors is based on deposition of carbon onto oriented crystalline silicon using Microwaves. Plasma assisted Chemical Vapour Deposition (MW-CVD) technique was described by Bergmaier et al. (1996). This technique required a specific amount of nitrogen in the process gas, namely about 1.3% in relation to carbon.

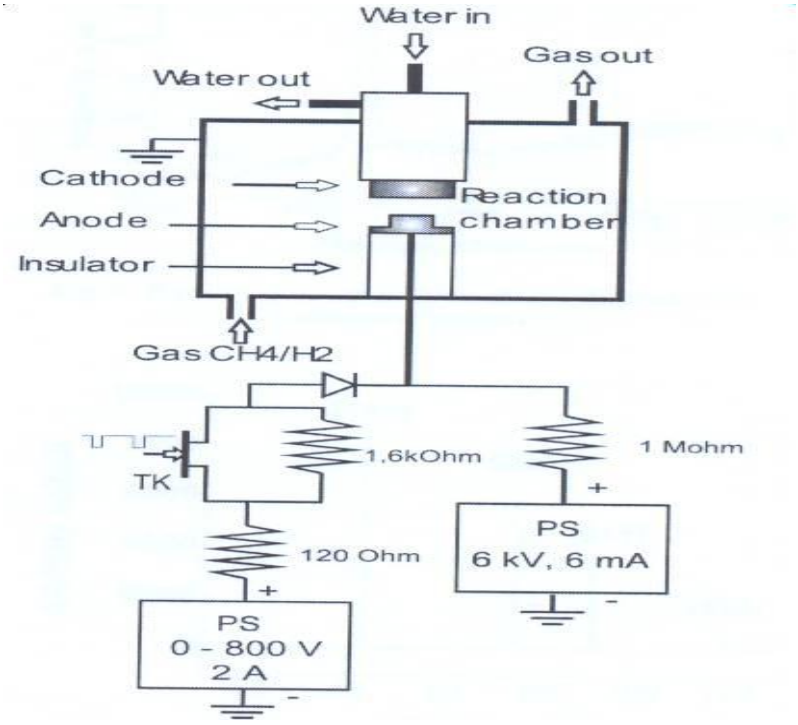


Figure 1.1: Schematic diagram of CVD diamond production Akulinichev et al., (2003)

1.7 Application of diamond detectors

Application of diamond as a detector of electro-magnetic radiation has been extensively described. Pillon et al. (1995) used a type IIa diamond detector as a neutron spectrometer to measure neutron spectra. In plasma diagnosis, diamond radiation detectors have been applied to detect charge exchange atom during spectrometry (Kovalchunk et al., 1994). A dosimeter for radiotherapy was described by Ramkumar et al. (2001) using CVD grown

diamond. The high sensitivity and the near biological tissue equivalence of diamond make it a material suitable as detector for on-line dosimetry (Bruzzi et al., 2000). In on-line configuration, detector-grade high-purity CVD diamond showed sensitivities almost four orders of magnitude higher than that of ionization chamber (Bruzzi et al., 2000). Whitehead et al. (2000) supported the statement by Ramkumar et al. (2001) that diamond is potentially a very suitable material for use as a radiation dosimeter in biological environments (Assiamah et al., 2004).

Diamond can be operated as a simple conduction counter in either conventional pulse mode or in current mode in a high radiation field (Kozlov et al., 1977). Energy resolution of 82 keV at room temperature spectroscopy of alpha particles was reported by Canali et al. (1979). Because of their wide band-gap, diamond detectors are well suited for operation at elevated temperatures (Konorova et al., 1971, Nava et al., 1979). It has also been demonstrated that ionization by interacting radiation will produce electrical conductance in CVD diamond crystal (Konorova et al., 1971). Although the scintillation properties of diamond and its use as indirect detector of radiation have been reported in synthetic crystals (Nam, 1987), scintillation properties in CVD diamond is yet to be reported. An investigation into the exposure geometry of the diamond sensor that will produce maximum absorption of the incident X-ray beam was conducted (Assiamah et al., 2006). It has also been frequently reported that both the response and sensitivity of CVD diamond to X-ray photons are susceptible to the presence of defects within the crystal and in addition some diamonds due to presence of trapping centers are light sensitive e.g. (Assiamah et al., 2006). A systematic investigation into the type of CVD

diamond grade that would respond most sensitively and linearly to mammography X-rays has not yet been undertaken. The main objective of this work is therefore to assay the CVD diamond type wafer in terms of impurities and defect levels against the characteristic performance with the view to narrow the motive for use as dosimeters or spectrometers. This is with a view to guide the selection of parameters needed to fabricate CVD wafers, which would, as a quality control tool, be easily and routinely used for dose determination in mammography X-ray diagnoses and screening for cancer.

1.8 Monte Carlo (PENELOPE) code

The accuracy and exactness of the Monte Carlo (PENELOPE) code has been tested to a degree for which physical parameters are known to have sufficient statistics and superior accuracy over deterministic and analytical methods. A new version of Monte Carlo (MC) code PENELOPE (PENetration and Energy Loss of Positrons and Electrons), was released to the NEA Data Bank for general distribution in 2006. This is one of the powerful and well established MC code systems for Monte Carlo simulation of electrons and photons transport. PENELOPE performs Monte Carlo simulation of coupled electron-photon in arbitrary material for a wide energy range, from a few hundred electron volts to 1GeV. Photon transport is simulated by the conventional detailed method in which all interaction events experienced by a particle is simulated in chronological succession. This is in view of the fact that photons undergo a limited number of interactions before they are locally absorbed. Electron and positrons are generated on the basis of mixed procedures which combine detailed simulation of hard events with condensed simulation of soft interactions. A geometry package called

PENGEOM permits the generation of electron photon shower in material systems consisting of homogeneous bodies limited by quadric surfaces (Baro et al., 1994; Salvat et al., 1996; Sempau et al., 1997).

The PENELOPE code has been benchmarked against experimental data and found to be in good agreement for a wide range of energy and materials, as well as the most accurate means of predicting dose distribution (Baro et al., 1995; Salvat et al., 1996; Sempau et al., 1997). Mammography X-ray beam absorbed dose has also been assessed with Monte Carlo simulations. Doi and Hean-ping in 1980 evaluated mammography absorbed dose using MC simulation. Dance (1980) also calculated integral radiation dose in xeromammography with MC code. Some investigations on mammography techniques using MC code are: Backscatter factors for mammography calculated with MC methods by Kramer et al. (2001); MC simulation of X-ray spectra generated by keV electrons by Llovet et al. (2003).

1.9 Introductory description of study

This thesis aims at bringing out the influence of defects and impurities on CVD diamond detectors for a choice of a CVD diamond detector that can be used as dosimeter and spectrometer. The work's initial focus was on the interaction of α-particles on CVD diamonds. Their response to charge particle surface interactions when used as detectors and spectrometers in relation to their physical characteristics are presented. Subsequently the responses of the CVD diamonds to interactions of X-rays in relation to the same physical parameters were analyzed. Evaluation of the results analytically and

experimentally were conducted firstly with an X-ray spectrum obtained from a germanium detector as well as the X-ray response rate of the CVD diamond when used as dosimeters. The presence of the various physical factors and their possible influence on the detector response when exposed to X-rays was analyzed. For validation of the experimental results the Monte Carlo (PENELOPE) code, was used.

1.9.1 Overview of characterization of CVD diamond detectors

In Chapter 2 of this thesis, the CVD diamond detectors were characterized in order to evaluate their behaviour as radiation detector using single substitutional nitrogen concentration (ESR), Raman broadening, ultra violet (UV), thermo-luminescence (TL) and current leakage. The influence of single substitution nitrogen, UV, Raman and thermo-luminescence (TL) as well as the current leakage for each CVD diamond detector forms the basis for a quantitative analysis of the impurity concentration and defect levels for each of the CVD diamonds analyzed either individually or as groups (grade). The Chapter presents an in-depth analysis of the performance of each of the CVD type diamond wafers when exposed to surface interacting alpha particles against the influence of the impurities found in each of the specimens. The prime objective being an understanding of the influence the impurity presence has in the matrix that is exposed to radiation. The secondary objective is the laying out of the criteria required for selecting the diamond material for use as an alpha particle dosimeter or spectrometer. The results of the analysis has been accepted for publication and made available on line (Mavunda et al., 2008). A copy of the paper is bound with this thesis.

1.9.2 Overview of alpha spectroscopy

When alpha particles interact with the diamond wafer, a number of e-h pairs are produced which follow its track, and are proportional to the energy loss in diamond samples (Angelone et al., 2004). The charge (Q_0) produced by the ionized particle is given by

$$Q_0 = eE_i/13.2 \text{ eV} \quad (1.1)$$

where e is the electron charge (1.6022×10^{-19}C), E_i is the energy (in eV) of the detected ionizing particle and 13.2 eV is the energy which produces an electron-hole pair (Angelone et al., 2004). The collected charge is related to the detector thickness (L). The charge (Q_c) can be expressed as

$$Q_c = ex/L \quad (1.2)$$

where x is the thickness of diamond traveled by the carrier before trapping (Angelone et al., 2004). Chapter 3 of this work is a further analysis on the CVD diamond performance as alpha spectral sensor discussed in Chapter 2, theoretically carried out with a view to evaluate the exact and reported alpha spectral resolutions of CVD diamond. The absolute efficiency, energy peak efficiency, energy peak resolution of the detector, the stopping power and the alpha particle range in the CVD diamond detectors were calculated. The experimental spectra of the detector's were analytically stripped of the background fluctuations and noise for a true and comparative performance analysis using ORIGIN 6.1 is discussed.

1.9.3 Overview of detector calibration

An applied bias voltage on the detectors creates an electric field in them, such that the ion pairs created from in-coming ionizing radiation are swept to their respective electrodes by

the electrical field. The pulses formed and collected through a pre-amplifier to the amplifier ultimately to the multi-channel analyzer to generate a spectrum or to a counter where counts are collected. In of this work, a germanium detector was used as a standard detector. Calibration was (using Am-241, Ba-133 and Co-57 reference sources) performed and correction for attenuation by different material used is described in Chapter 4. Efficiency of the detector was used to correct for background counts from both intrinsic and extrinsic effect using the stripping technique by Fewell et al. (1977) and Seelentag et al. (1979) from the acquired spectra. The computer code PENELOPE (PENetration and Energy LOss of Positron and Electrons), was used to simulate the spectra which was analytically compared with the detected spectra obtained from a germanium detector. The stripping technique has been published in the article presented in Chapter 4 (Mavunda et al., 2004).

1.9.4 Overview of CVD diamond detectors response to X-rays

In this section the fact that for ohmic contact on CVD diamonds, the charge collection (response) is proportional to the electric field and saturates (Toshisuke et al., 2006) at higher applied electric field was observed. The response of CVD diamonds to low energy X-rays is presented in Chapter 5. The diamond response to X-rays was also related to the presence of defects levels and impurity concentrations discussed in Chapter 2. The differences in resistivity of the CVD diamonds were also analyzed and its impact on their overall performances to X-rays is presented.

1.9.5 Overview of evaluation of detector response to X-rays using PENELOPE

In Chapter 6 the application of Monte Carlo (PENELOPE) simulation was performed to validate the observed response of the CVD diamond to X-rays. Simulated X-ray spectra for low peak voltages using the geometry file PENSLAB as a sub-route of PENELOPE were presented and used for this part of the study. Different thicknesses (0.5 cm to 2.0 cm) of pure diamond were used in the simulation, taking into account the geometry as well as the filters used during the experiment. Attenuation to the X-ray beam apertures needed to cover the detector surface area form part of the analysis.

The general conclusions from the work and the techniques used are summarized and presented in Chapter 7.

1.10 References

Akulinichev SV, LebedevSG and Vyalov GN 2003. *Moscow Meson Factory, Atomic Energy* **94** 49

Albagli D, Han S, Tkaczyk EJ, Landberg CE, Opsahl-Ong B, Granfors PR, Levis I, D'Orrsi CJ, and Hendrick RE 2000. *Med. Phys*. **27(3)** 558

Anastasio MA, Yoshida H, Nagel R, Nishikawa RM and Doi K 1998. *Med. Phys*. **25(9)** 1613

Angelone M, Pillon M, Marinelli M, Milani E, Paoletti A, Tucciarone A, Pucella G and Verona-Ranati G 2004. *Radiat. Prot. Dosim*. **110(1-4)** 233

Araikum S 1993. *MSc thesis, University of the Witwatersrand, Johannesburg, South Africa*

Armantrout GA, Swierkowski SP, Sherohman JW and Yee JH 1977. IEEE Trans. *Nucl. Sci.* **NS24 (1)** 121

Asaga T, Masuzawa C, Yoshida A and Matsuura H 1995. *Journal of digital imaging* **8(1)** 70

Assiamah M 2004. *PhD thesis. University of the Witwatersrand, Johannesburg, South Africa, 87*

Assiamah M, Nam TL and Keddy RJ 2006.Appl. *Radiation and Isotopes* **65** 545

Attix, F.H., 1986. *Introduction to Radiological Physics and Radiation Dosimetry. Wiley, New York, pp. 292*

Baró J, Sempau J, Fernández-Varea JM and Salvat F 1994. Nucl. Instrum. *Methods Phys. Res.* **B100** 31

Bazzocchi N, Zuiani C and Facecchia I 1998. *Phys. Medica*. **14(2)** 1

Bell RO, Entine G and Serreze HB 1974. *Nucl. Instrum. Meth*. **117** 267

Berger MJ and Hubbell JH 1987. XCOM: *Photon cross-sections on A Personal Computer. NBSIR 87-3597, U.S. DEPARTMENT OF COMMERCE National Bureau of standards Gaithersburg MD 20899*

Bergmaier A, Dollinger G, Faestermann T, Frey CM, Ferguson M, Guttler H, Schulz G and Willerscheid 1996. *Diamond and Related Materials* **5** 995

Bhat M, Pattison J, Bibbo G and Caon M 1998a. *Med. Phys.* **25(1)** 114

Bhat M, Pattison J, Bibbo G and Caon M 1998b. *Med. Phys*. **25(2)** 303

Boone JM, Fewell TR and Jennings RJ 1997. *Med. Phys*. **12(24)** 1863

Bruzzi M, Bucciolini M, Cirrone GAP, Cuttone G, Guasti A, Mazzocchii S, Pirollo S, Sabini MG and Sciortino S 2000. *IEEE 121*

Bruzzi M, Bucciolini M, Cirrone GAP, Cuttone G, Mazzocchi S, Pirollo S and Sciortino S 2000. *Nucl. Instrum. and Meth. in Phys. Res.* **A454** 142

Burgemeister AE 1982. *Proc. Eighth Symposium on Microdosimetry 998*

Canali et al.1979. *Nucl. Instrum. Meth*. **160** 73

Canberra Nuclear Products Group. *Edition Eight. Canberra Industries. Inc. One State Street Mariden. CT06450*

Champion FC and Wright SB 1957. *Proc. Phys. Soc*.**73** 385

Chen CS, Doi K, Vyborny C, Chan HP and Holji G 1980. *Med. Phys.* **7(6)** 627

Cotty WF 1956. *Nature.* **177** 1075

Curtiss LF and Brown BW 1947. *Phys. Rev*. **72** 643

Dance RD 1980. Phy. Med.Biol. 25 25

Denotter W, Merchant TE, Beijerinck D and Koten JW 1996. *Anticancer research* **16(B5)** 3173

DeVincentis G, Scopinaro F, Pani R, Pellegrini R, Soluri A, Ierardi M, Ballesio L, Weinberg IN and Pergola A 1997. *Preliminary study* **17(3)** 1627

Dodd GD 1993. *Screening for breast-cancer* **16(3)** 1038

Doi K and Heang-Ping C 1980. *Radiology* 135 199

Eliseev AP, Sobolev EV and VinsVG 1988. *Sov. J. of Superhard Materials (Sverkhtverdye Materially)* **10(1)** 11

Fahrig R and Yaffe MJ 1994. *Med. Phys*. **21(9)** 1473

Fahrig R, Rowlands JA and Yaffe MJ 1996. *Med. Phys*. **23(4)** 557

Fallon PJ, Nam TL and Keddy RJ 1992. *Diamond and Related materials* **1** 1185

Fallon PJ, Nam TL, Keddy RJ, Burns RC and Grabbelaar JH 1990. *Appl. Radiat. Isot.* **41(1)** 35

Fewell, T.L. and Shuping, R.E., 1977. *Med. Phys*. **4(3)**187

Globacan (2000). *Cancer incident, mortality and prevalence worldwide, version 1.0, IARC Cancer Base No.5. Lyon, IARC Press*

Gregoire A, Bernard C, Levallee G, Morin C and Philie M 1992. *Mammography* **121(4)** 239

Hess T, Knop MV, Hoffman U, Brix G, Junkermann H, Zuna T, Vonfournier D and Vankaick G 1994. *Pharmacokinetic analysis of GD-DTPA enhancement in dynamic MR of breast – carcinoma* **160(6)** 518

Hofstandedter R 1948. *Phys. Rev*. **73** 631

Hofstandedter R 1949a. *Phys. Rev*. **4(4)** 2

Hubbell JH 1999a. *Phys. Med. Biol*. **44** R1

Hubbell JH 1999b. *X-ray Spectrum*. **28** 215

Israel HI, Lier DW and Storm E 1971. *Nucl. Instrum. And Meth. In Phys. Res.* **A91** 141

Jansen JTM and Zoetelief J 1997. *Optimization of mammographic breast cancer screening using a computer simulation model* **24(2)** 137

Johnson GA and O'Foghludha F 1980. *Med. Phys*. **7(3)** 189

Kaiser WA 1993. *Radiology* **33(5)** 292

Kallergi M, Carney GM and Gaviria J 1999. *Med. Phys*. **26(2)** 267

Kaneko J and Katagiri M 1996. *Nucl. Instrum. and Meth. in Phys. Res.* **A383** 547

Kaneko J, Katagiri M, Ikeda Y and Nishitani T 1999. *Nucl. Instrum. and Meth. in Phys. Res.* **A422** 211

Keddy RJ, Nam and Burns RC 1987. *Phys. Med. Biol*. **32 (6)** 751

Kennedy PJ 1959. *Proc. Roy. Soc. Of London* **A253** 37

Knoll GF 1989. *Radiation detection and measurement. Second edition. John wiley & Sons*

Konorova EA and Kozlov SF 1971. *Sov. Phys. Semicond* **4(10)** 1600

Konorova EA and Schevchenko SA 1967. *Phys. Tech. Semicond*. **1** 364

Konorova EA, Kozlov SF and VaVilov V.Sov 1966. *Phys. Solid State* **8(1)** 1

Kovalchuk VD, Trotsik VI and Kovalchuk VD 1994. *Nucl. Instrum. and Meth. in Phys. Res.* **A351** 590

Kozlov SF, Konorova EA, Kuznetsov YA, Salikov YA, Redko VI, Grinberg VR and Meilman ML 1977. *IEEE Trans. Nucl. Sci*. **NS24(1)** 235

Kozlov SF, Stuck EA, Hage-Ali M and Siffert P 1975. *IEEE Trans.Nucl. Sci*. **NS22** 160

Kramer R, Drexler G, Petoussi-Henss N, Zankl M, Ragulla D, and Paner W 2001. *Phys. Med. Biol.* **46** 771

Lado MJ, Tahoces PG, Souto M, Mendez AJ and Vidal JJ 1997. *Med. Phys*. **24(9)** 1385

Land CE 1980. *Cancer* **46** 868

Lederer C.M. and Shirley V.S. 1978. *Table of Isotopes. (7th Edition) ed.), Wiley, New York pp. 802*

Lee PC 1997. *Med. Phys*. **24(9)** 1485

Llovet X, Sorbier L, Compos CS, Acosta E and Salvet F 2003. *J. applied Phy*. **93(7)** 3844

Maidment ADA and Yaffe MJ 1994. *Med. Phys*. **21(6)** 721

Malm HL and Martini M 1974. *IEEE Trans. Nucl. Sci*. **NS21 (1)**322

Mavunda RD, Assiamah M, Nam TL and Keddy RJ 2004. *Radiation Physics and Chemistry* **71** 991

Mavunda RD, Zakari YI, Nam TL and Keddy RJ 2008. *Appl. Radiation and Isotopes* **66** 1128

McKay KG 1948. *Phys. Rev*. **74** 1606

Mole RH and Path FRC 1978. *The British Journal of Radiology* **51** 401

Momosa A, Takeda T and Itai Y 1995. *Rev. Sci. Instrum*. **66(2)** 1434

Mukoyama T 1975. *Nucl. Instrum. Meth*. **125** 289

Nam TL, Fallon PJ, Keddy RJ, van Rijn HJ and Andrews JF 1987. *Int. J. Appl. Isot*. **40** 657

Nam TL, Karfunkel U and Keddy RJ 1991. *Radiation Effects and defects in solids* **116** 233

Nava F, Canali C, Artute M, Gatti E and Manfredi PF 1979. *IEEE Transactions on Nucl. Science* **26(1)** 308

Nawano S 1995. *Journal of digital imaging* **8(1)** 67

Pillon M, Angelone M and Kransilnikov AV 1995. *Nucl. Instrum. and Meth. in Phys. Res.* **B101** 473

Prats E, Aisa F, Abos MD, Villavieja L, Garcialopez F, Asenjo MJ, Razola P and Banzo J 1999. *Mammography and Tc-99m scintimammography in suspected breast cancer* **40(2)** 296

Ramkumar S, Buttar CM, Conway J, Whitehead AJ, Sussmann RS, Hill G and Walker S 2001. *Nucl. Instrum. and Methods Phys. Res*. **A460** 401

Salvat F, Fernández-Varea JM, Baró J and Sempau J 1996. *Ciemat (Centro de Investigaciones Energéticas, Medioambientales y Technológicas) Technical Report no.799*

Schmidt RA and Nishikawa RM 1995. *Journal of digital imaging* **8(1)** 74

Seelentag, W.W. and Panzer, W 1979. *Phys. Med. Biol*. **24(4)**767

Sempau J, Acosta E, Fernández-Varea JM, Baró J and Salvat F 1997. *Nucl. Instrum. Methods Phys. Res.* **B132** 377

Siemens Medical Solutions Website 2004. *http://www.med.siemens.com/*

Siffert P, Berger J, Scharager C, Cornet A, Stuck R, Bell RO, Serreze HB and Wald FV 1976. IEEE Trans. *Nucl. Sci.* **NS23 (1)** 159

Simonetti G, Cossu E, Montanaro M, Caschili C and Giuliani V 1998. *European Journal of Radiology* **27** S234

Sorenson AJ 1938. "Physics in nuclear medicine" edition Grune and Stratton Inc. New York 10003

Sumiya H and Satoh S 1996. *Diamond and Related Materials* **5** 1359

Tanaka T, Kaneko J, Takeuchi D, Sumiya H, Katagiri M, Nishitani T, Takeuchi H, Lida T and Ohkushi H 2001. *Review of scientific instruments* **72(2)** 1406

Toshisuke K, Kinya H, Hisashi K, Kunishino M, Shoji O, Takeshi T, Yukio U, Kaori Y and Kenji Y 2006. *IEEE Transactions on Nuclear Science* **53(2)** 630

Tewksbury SK 1995. *Microelectronic Systems Research Centre Dept. of Electrical and Computer Engineerin, West Virginia University, Morgantown. WV 26506* **304** 297

Umschaden HW and Haselbach H 1997. *ACTA medical Austriaca* **24(2)** 39

Urlau RR 1960. *PhD thesis , University of the Witwatersrand*

Van Heerden PJ 1954. "*The crystal counter", thesis, Utrecht*

Vanoord JC, Vandervliet AM, Thyn CJP, Mak and Hoogeboom GJ 1991. *Fortschritte AUF geebiete der rontgenstrahlen und der neuen bildgebenden verfahren* **155(1)** 63

Vermeulen LA 1965. *PhD thesis, University of the Witwatersrand*

Whitehead AJ, Airey R, Buttar CM, Conway J, Hill G, Ramkumar S, Scarsbrook GA, Sussmann RS and Walker S 2000. *Nucl. Instrum. and meth. in Phys. Res*. **A460** 20

Willardson RK and Danielson GC 1950. *Phys. Rev*. **77** 300

Wooldridge ED, Ahearn AJ and Burton JA 1947. *Phys. Rev*. **71** 913

Wouters LF and Christian RS 1947. *Phys.Rev*. **72** 1127

Wu X, Barnes GT and Tucker DM 1991. *Radiology* **179** 143

Yaffe MJ and Rowlands JA 1997. *Med. Phys*. **42** 1

Young KC, Ramsdale ML and Rust A 1996. *The British Journal of Radiology* **69** 555

Young KC, Ramsdale ML and Rust A 1996. *The British Journal of Radiology* **69** 555

Zhang M, Xia Y, Wang L and Gu B 2004. *J.Phys. D: Appl. Phys. **37** 3198*

Chapter 2

THE PRESENCE OF DEFECTS IN, AND THEIR INFLUENCE ON THE PERFORMANCE OF, CVD DIAMOND AS AN α-PARTICLE RADIATION SENSING ELEMENT

2.0 Abstract

Three types of diamonds produced by Chemical Vapour Deposition (CVD) and broadly classified as Detector Grade (DG), Optical Grade (OG) and Single Crystal (SC) were evaluated in terms of their response to α-particle radiation when used as detection elements. It is well known that the presence of defects in diamond, including CVD specimens, not only dictates but affects the response of diamond to radiation in different ways. In this investigation tools such as electron spin resonance (ESR), thermo-luminescence (TL), Raman spectroscopy and ultraviolet (UV) spectroscopy were used to probe each of the samples which were then graded on their performance as α-particle radiation detectors. This Chapter discusses the presence of defects identifiable by the techniques used and correlates the radiation performances of the three types of crystals to their presence.

2.1 Introduction

Recent advances in homoepitaxial synthesis of a single crystal diamond have invigorated the already growing interest in chemical vapour deposition (CVD) diamond crystal for use as a radiation probe. In general epitaxy, on foreign substrates, leads to a polycrystalline diamond, with detector and optical properties of grain boundaries that precludes its use in some of the desired applications. Some progress has been made in recent years in growing CVD diamond on Iridium (Schreck et al., 2001).

Single crystal CVD diamond with the reported carrier transport properties (Isberg et al., 2002), could surpass other wideband gap materials for power and high frequency electronics application. The electronics and optical properties of CVD diamonds are determined by intrinsic defects and extrinsic contaminants or dopands, most prominently nitrogen, silicon, boron and phosphorus as well as different structural morphologies (Davies, 1999). The nominally un-doped polycrystalline CVD diamond has characteristics of both electrons and holes contributing to transient photocurrents. The combined charge mobility (electrical behaviour) depends on the film quality, carrier density, grain size, higher growth temperature and purity of the diamond film (Nebel, 2003). The life-time of photo-generated carriers in the conduction and valence bands is short with a time constant in the range 340-550 pico seconds. The density (N_T) of traps is calculated from the expression

$$N_T = \frac{1}{\tau \upsilon_{th} \sigma_{cap}} \qquad 2.1$$

Where τ is the deep trapping lifetime ($\cong$ 340-550 ps), υ_{th} is the thermal velocity of carriers ($\cong 10^7$ cm s^{-1}) and σ_{cap} is the capture cross section ($10^{17}cm^{-3}$). Based on these parameters a trap density of $10^{17}cm^{-3}$ was realized as the density of trapping centers most likely present in grain boundaries (Nebel, 2003). Grain boundaries are believed to act as charge trapping and recombination centers in polycrystalline CVD diamond (Manfredotti et al., 1996) but absent in single crystal CVD diamond (Hammersberg et al., 2001; Sellin et al., 2007). The interaction of photon generated carriers with traps and defects in the band gap of diamond has been investigated. When an electric field is applied to a

semiconductor exposed to radiation, the electron-hole pair generated separates and drifts towards opposite electrodes. Charge trapping and recombination may however prevent some carriers from being collected by the electrodes (Hecht et al., 1932; Gerrish, 1995; Sciortino, 1999). The interstitial nitrogen which is non-bonded to CVD diamond crystal exhibits a very low activation barrier and may diffuse out of the bulk at low temperatures (Kuo et al., 2001).

High pressure/high temperature (HPHT) diamond with single substitutional nitrogen (Ns) has a recombination efficiency which compromises the response (Nam, 1989). However high single substitutional nitrogen concentration was also observed to lower the electron trap levels when compared with specimens synthesized with lower single substitutional nitrogen concentrations (Nam et al., 1991). Whilst the concentration of single substitutional nitrogen can be accurately determined by electron spin resonance (ESR), nitrogen complexes are normally determined by UV absorption (Davies, 1999; Nam et al., 1991). Kuo et al., (2000) has shown that incorporation of nitrogen leads to a chemical shift and a reduction in Raman peak intensity. UV visible absorption results show that compared to undoped film, nitrogen doped films have a higher relative intensity of UV absorption (Kuo et al., 2001). Thermo-luminescence (TL) occurs in crystal due to the radiative recombination of previously trapped charge carriers, at luminescence centers. The larger the concentration of these centers, the higher the thermo-luminescence yield. A large number of solids exhibit the presence of centers with which carriers can only recombine non-radiatively (Araikum, 1993) in this case single substitutional nitrogen centre (N_S). The TL is mainly dominated at broad (~0.5 eV width) signal referred to as

band-A emission (Iakoubovskii et al., 2002) which is generated via strain-induced broadening from a vibronic side band. Band-A type luminescence originates either from dislocations or boron related impurities (Ruan et al., 1992). The TL is explained by the donor-acceptor (DA) pair recombination model (Dean, 1965).

In this Chapter the characteristics of nine CVD diamond samples classified as Detector grade (DG), Optical Grade (OG) and Single Crystal (SC) were analyzed for use as a radiation probe. These CVD diamond samples were characterized to obtain information about their levels of impurities including nitrogen and consequently to establish the material quality.

The tools commonly used in diamond characterization are electron spin resonance (ESR) which enables the identification of the concentrations of single substitutional nitrogen, hydrogen and other impurities (Nebel, 2003). Ns-V-Ns complexes could be from the aggregation of single nitrogen atoms or N_2 incorporation followed by the capture of a vacancy. The aggregation is temperature activated and depends on the crystal orientation (Doverspike et al., 1993; Lin et al., 1996; Snail et al., 1992; and Taylor et al., 1996). Ultra violet (UV) spectroscopy can be used to identify the diamonds with such nitrogen complexes and the nearest neighbour nitrogen substitutional forms $(N_s\text{-}N_s)^o$ (Davies, 1999; Iakoubovskii et al., 2000). Raman spectroscopy was used to identify the purity of diamond material, to establish how much stress/strain the CVD diamond material was under, and the orientation of the crystal of the material i.e., polarization of the scattered light in the material (e.g. crystallinity of the CVD diamond) (Herzberg, 1945).

It is a well known fact that defects in diamond, including CVD specimens, affects the response of diamond to radiation in different ways. The research described in this Chapter was aimed at correlating the α-particle radiation detection performance characteristics of CVD diamonds to the defects identified by the above mentioned tools.

2.2 Electron spins resonance (ESR)

The ESR technique exploits the paramagnetic nature of diamond due to the evenly distributed anti-bonding orbital (C-N) of unpaired electrons of nitrogen in diamond (Fallon, 1989). The interaction between the spin angular momentum of an unpaired electron and the magnetic field are used as the source of the measured signal in ESR. The degeneracy of the spin state of the unpaired electron is lifted in magnetic fields and the transitions between the spin levels are induced by radiations of appropriate frequency. The observation of the ESR signal relies on maintaining the population difference between the spin levels, which in turn depend on the relaxation times during the measurement. The relaxation time of low nitrogen concentration is long and the population difference between the single spin become smaller and hence more difficult to measure the ESR transitions. The absorbed spectra are the indicators of electron spin resonance (ESR) or electron paramagnetic resonance (EPR) observed when the spin state splits by an amount proportional to the magnetic field. The transition energy is expressed in terms of the applied magnetic field, the electron spin g-factor and the Bohr magnetron (a constant U_B) (Wertz et al., 1986). Electron spin resonance applied to CVD diamond reveals a number of defect centers involving the concentration of the single substitutional

nitrogen atoms (Ns centers). Single substitution nitrogen concentration is determined by dipolar interactions between the two successive line-widths of the single substitutional lines. Most CVD diamond samples studied so far by ESR are polycrystalline films with random orientation of the grain (Iakoubouskii et al., 2002). Using the ESR in monocrystalline and natural diamonds the single substitutional nitrogen concentration center has been thoroughly characterized and assigned to the neutral single substitutional nitrogen concentration centers (Ns) (Davies, 1999). The experiments indicate the intrinsic angular momentum and magnetic moment as the property of an electron spin. Thus diamond specimen placed in a magnetic field exhibits Para-magnetism due to the unpaired electron spins.

2.2.1 Experimental measurement of single substitutional nitrogen concentration in CVD diamond with ESR

Adopting the rapid scan technique each of the diamond specimens was placed in a resonating cavity and a variable magnetic field applied perpendicular to the microwave field. The experimental values of each of the samples from the three classified diamond types was assayed, first by placing each sample in the magnetic field of a Bruker microwave bridge ESP 380-1010 (Fig. 2.1) coupled to a ESP 380-1020 controller and an ESP 300E electron spin resonance (ESR) spectrometer unit at a frequency of 9 GHz. The sample weight was entered into the acquisition program. The exhibited paramagnetic properties of the unpaired electrons of the single substitutional nitrogen content of the diamonds were measured. The concentration of each sample was determined by a comparison of its signal with a signal from a calibrated reference sample. The single

substitutional nitrogen concentration was determined from the dipole interaction between the two nitrogen centers in ppm, by measuring the relative amplitude of an acquired spectrum of the ESR (Fig. 2.2). The single substitutional nitrogen concentration in CVD diamond were calculated using the spin Hamiltonian equation (Iakoubovskii and Stesmans 2002):

$$H = \mu_e S.g.B + \sum (S.A_i I_i + g_{N\,i}\mu_N I_{i.}B) + S.D.S \qquad (2.2)$$

where, μ_e and μ_N are the electron and nuclear magnetons, respectively, and g_N is the nuclear g-factor ((Iakoubovskii and Stesmans 2002). The first term in (Eq. 2.2) describes the electron Zeeman interaction of an electron system of spin S with the applied magnetic field B via the electronic g-tensor ((Iakoubovskii and Stesmans 2002). The second term (Eq.2.2) account for hyperfine (hf) interaction of the electronic spin system with nuclei of spin I_i via hf matrix A_i (Iakoubovskii and Stesmans 2002). The third term is due to interaction of nuclear spin with the magnetic field (Iakoubovskii and Stesmans 2002). The small value of the product $g_N \mu_N$ for most nuclei gives only higher-order corrections to the electronic terms (Iakoubovskii and Stesmans 2002). The fourth term in (Eq. 2.2) characterizes spin-spin interaction via a traces matrix D (Iakoubovskii and Stesmans 2002). The spectrum Fig 2.2 is obtained from this interaction and the area under the curve represents the number of unpaired electrons which of the single substitutional nitrogen concentration.

The results of the diamond samples analyzed are presented in Table 2.1.

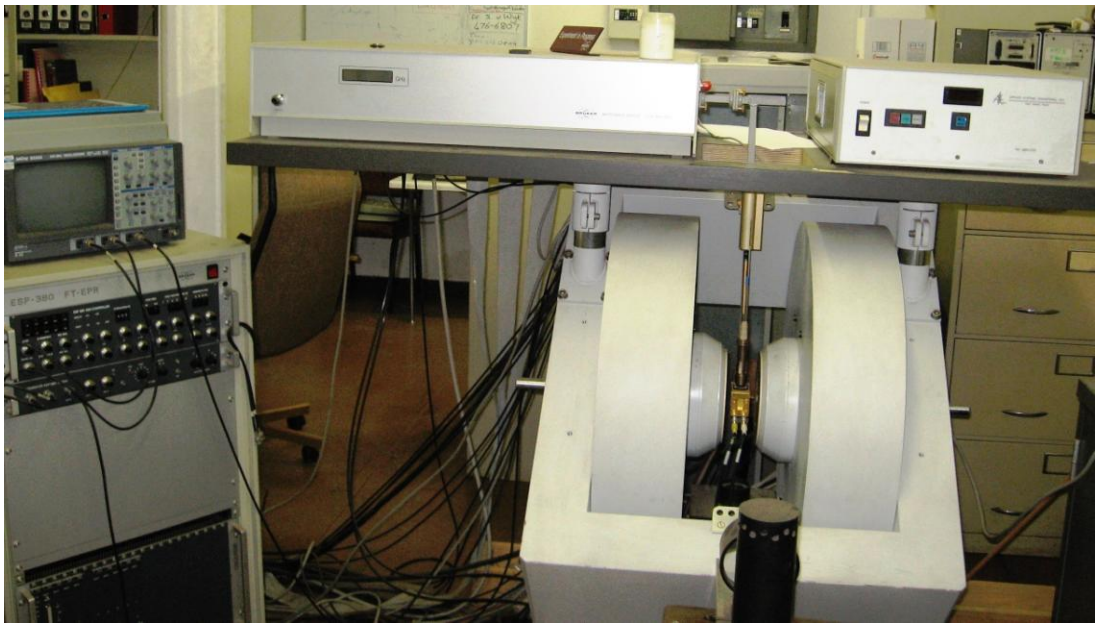


Figure 2.1: Illustration of the Bruker microwave bridge ESP 380-1010 used for measuring single substitutional nitrogen concentration

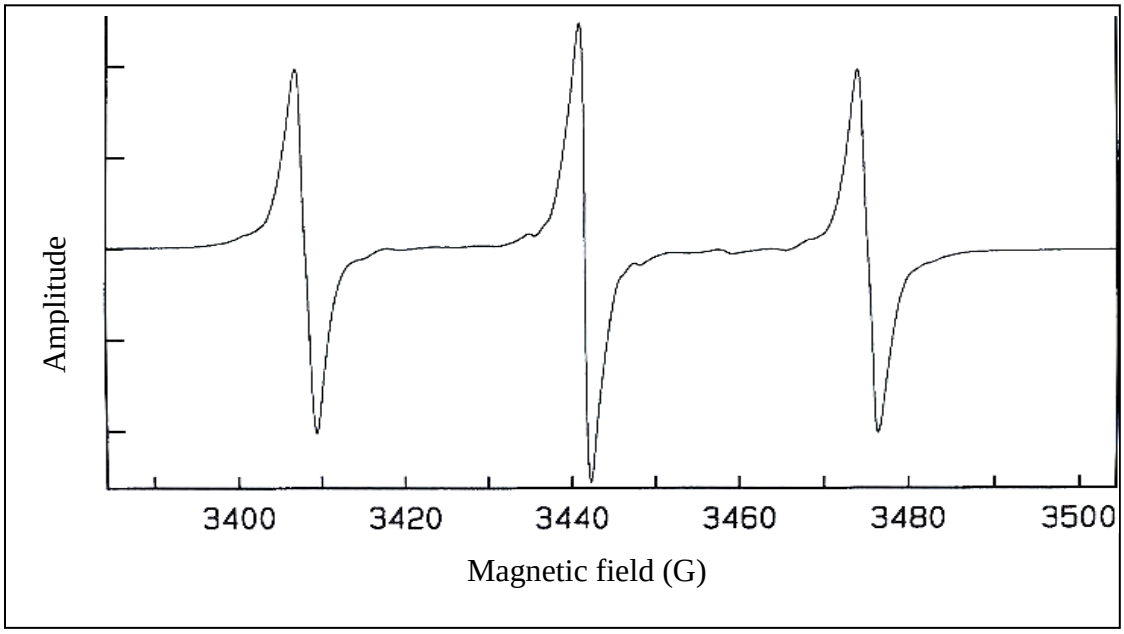


Figure 2.2: A typical ESR graph which was used to determine the single substitutional nitrogen concentration

Table 2.1 Characterization results of CVD diamond

Sample	Raman spectral broadening FWHM (cm^{-1})	TL response (arbt.unit)	ESR: single substitution nitrogen (ppm)	UV absorption (cm^{-1})	Total alpha counts (cps)	Absolute Efficiency %	Energy peak Efficiency %	Alpha FWHM (keV)
DG1	2.64±0.17	1147	3.5	0.51±0.06	32969	68	80	1010.59±27.03
DG2	2.57±0.17	881	4	1.93±0.13	31327	65	80	693.41±11.16
DG3	2.63±0.15	2024	5	1.03±0.08	29834	62	81	64.14±0.8
DG4	2.55±0.16	814	5.3	1.9±0.05	32732	68	80	672.55±5.46
OG1	2.59±0.15	155	42.9	3.86±0.05	50314	104	60	7465.39±90.4
OG2	2.78±0.24	83	71	3.52±0.09	49010	101	60	5975.00±34.99
OG3	2.76±0.24	141	53.6	3.48±0.11	49397	103	60	7050.34±124.8
OG4	2.81±0.22	93	62.5	3.59±0.11	39046	81	60	7245.66±60.48
SC	2.32±0.03	25	<1	0.88±0.02	25401	52	80	85.28±0.9

2.3 Raman broadening

In a Raman spectroscope, a single-wavelength of light source (a laser) produces light which is directed to a microscope. This light illuminates and interacts with the sample. The interacting light photon is absorbed, transmitted and scattered. A light filter is used to remove the elastic scattering i.e. no change in its wavelength (Rayleigh scatter) and only the inelastic scattering (Raman scatter) is transmitted through and measured. The energy of the scattered radiation is less than the incident radiation for the Stokes line, upon collision with a molecule a photon may lose some of its energy. Both absorption and radiation (emission) of energy are unique characteristics of a particular molecule (structure) during the fluorescence process. The electrons remain in the excited state for about 10^{-8} seconds (this number varies depending on the atom or molecule in question) then, assuming all of the excess energy is not lost to the conduction band, the electron returns to the ground state (Lakowicz, 1983). The Raman scatter is dispersed by a beam splitter and is grated into a spectrum (Herzberg, 1945).

The energy increase or decrease from the excitation is related to the vibration energy spacing in the ground electronic state of the molecule and therefore the wave number of the Stokes and anti-Stokes lines are a direct measure of the vibration energies of the molecule. Hence, in Raman spectroscopy, only the more intense Stokes line is normally measured (Herzberg, 1945). To analyze the type of carbon atoms in a diamond film, the possible tool is the Raman spectroscopy.

2.3.1 Experimental measurement of Raman broadening effects in CVD diamond

For this work the 1st order scattering for the diamond samples in a sp^3 bonded form was assayed for the type of carbon atom before the samples were polished and cleaned. The Raman spectroscopy was conducted using a Jobin-Yvon T64000 Raman spectrometer (Fig.2.3) operated in single spectrograph mode with an Olympus microscope as micro-Raman attachment to acquire the spectrum. Excitation source of laser at a wavelength 514.5 nm from an argon ion laser was used to assay the diamond. Backscattered light was dispersed via 1800 grooves/mm grating onto a liquid nitrogen cooled charge collection detector (CCD). Laser spot size under the microscope was approximately 1.5 micron in diameter. The CVD samples were scanned with a 10x10 micron at 5 microns steps depth across the diamond. The results of the Raman measurements were fitted with a Lorentzian function to determine the Raman peak position and peak width at half height for each specimen. The FWHM of the acquired spectrum from the vibrations in the diamond with Raman peaks at 1332 cm^{-1} from a typical diamond spectrum such as that depicted in Fig. 2.4 the degree of the Raman broadening due to the absorption, transmission and scattering of the light illuminating the samples was calculated.

The wavenumber (N), in cm^{-1}, as a function of channel number x was calibrated (Genie 2000, 2006) as

$$N = C_0 + C_1 x + C_2 x^2 + C_3 x^3 \tag{2.3}$$

where C_0, C_1, C_2 and C_3 are the coefficients of the channel. C_0, represent the wavenumber offset, C_1 represents the "gain", and C_2 and C_3 account for the system

non-linearity. The Raman spectrum peak full-width at half maximum (FWHM in units of channels) as a function of per centimeter, indicate the broadening of Raman Peak due to grain boundaries effect in CVD diamond crystal, and the FWHM was calculated (Genie 2000, 2006) as

$$FWHM = \frac{F_0 + F_1\sqrt{E}}{C_1} \tag{2.4}$$

Where F_0 and F_1 are the coefficients of the FWHM equation

Samples with more defects/impurities show increase FWHM.

The results of Raman broadening full width at half maximum (FWHM) for each samples were recorded and tabulated in Table 2.1.

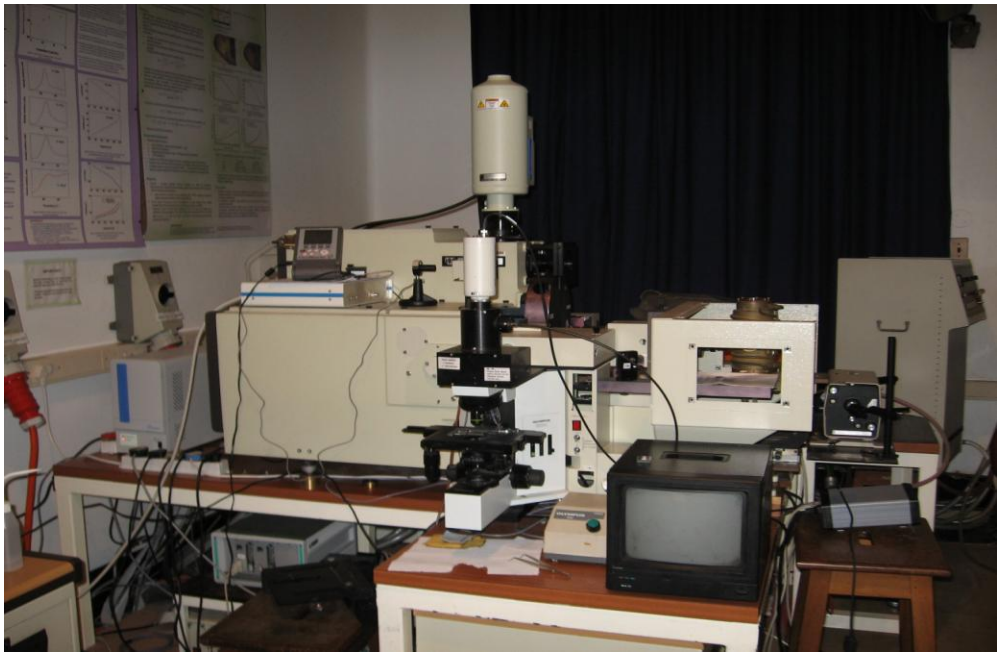


Figure 2.3: The laser and microscope system (Jobin-Yvon T64000,) for Raman spectroscopy

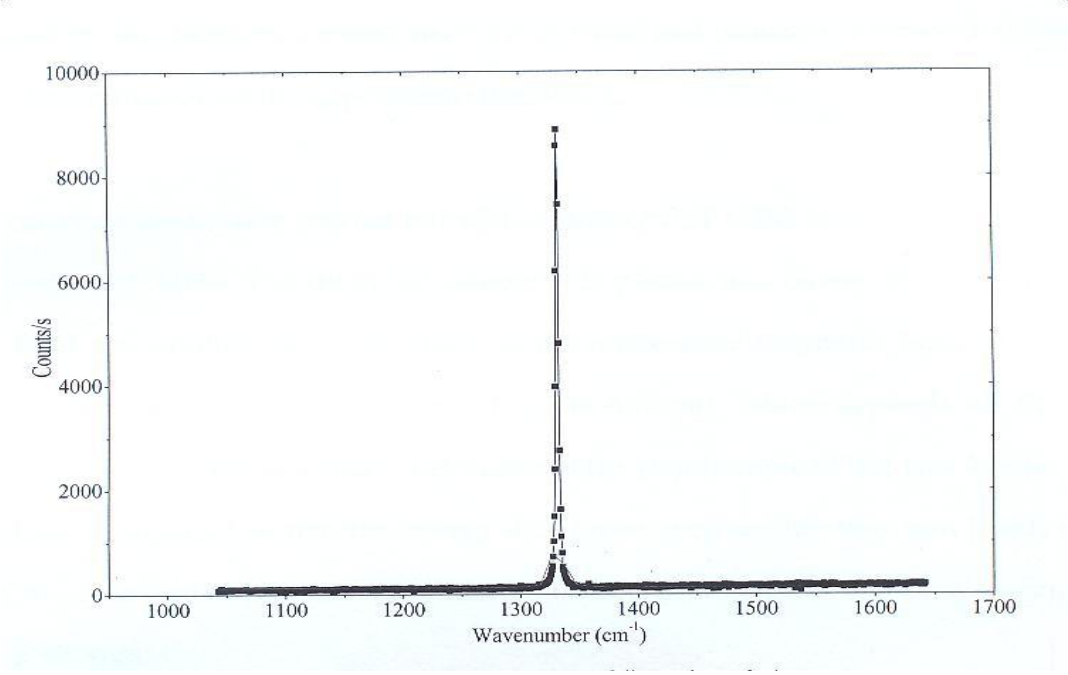


Figure2.4: A typical Raman spectrum showing the characteristic 1332 cm^{-1} of diamond

2.4 Thermo-luminescence (TL) emissions in crystals

When ionizing radiation interacts with a thermo-luminescence (TL) phosphor it causes electrons or holes in the crystal's atoms to move to higher energy states, where they stay trapped due to impurities in the crystal, until heated. Heating the crystal causes the trapped electrons to return to their normal ground state, releasing a light photon of energy equal to the energy difference between the trap state and the ground state (Khan, 2003). The energy states of electrons in the diamond samples, viz. the band structure, was derived from the solution of Schrödinger's equation for a periodically varying potential (Kittel, 1986), which characterizes the crystal lattice. The Krönig-Penney model assumes a potential to characterize the perfect lattice, revealing that electrons in the perfect crystalline solid can exist in allowed energy states (bands) while other energy values for electrons constitute forbidden zones (bands) (Araikum, 1993). The Fermi-Dirac

distribution $f(E)$ describes the occupancy of each electronic band, in terms of energy E, which relates the density of energy states, $D(E)$, to the density of available states, $Z(E)$, at given temperature, T, measured on the absolute scale (Araikum, 1993),

$$D(E) = Z(E)f(E) \tag{2.5}$$

$$f(E) = \frac{1}{\exp[(E-\mu)/kT]+1} \tag{2.6}$$

where μ is the chemical potential of the system and is a function of the temperature and the number of particles in the system. k is the Boltzmann constant. The Fermi energy ($E_f = \mu$ at absolute zero) level provides the demarcation level for the occupied energy states. All energy states below E_f are occupied while those above E_f are empty at absolute zero. At high temperature limit where $E - \mu >> kT$, The Fermi-Dirac distribution reduces to the Maxwell or Boltmann distribution (Araikum, 1993),

$$f(E) = \exp(\mu - E)/kT \tag{2.7}$$

For no transfer of charge particles between phosphor and heat reservoir

$$f(E) = \exp\left(-\frac{E}{kT}\right) \tag{2.8}$$

Equation 2.7 describes thermally stimulated processes such as thermo-luminescence and phosphorescence. Transition of electrons from one energy state to the other can be radiative and non-radiative (Seitz, 1938). This transition occurs sequentially by a charge carrier termed a phonon assisted transition**.**

The process of luminescence is illustrated in Fig. 2.5

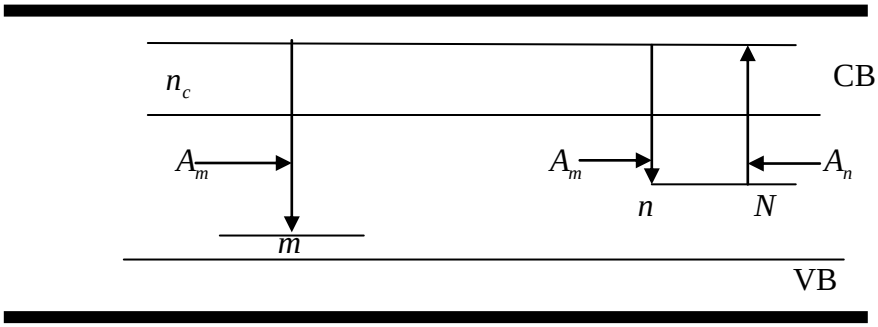


Figure 2.5: Energy level diagram concerning phosphorescence decay according to Adirovitch 1956

Where m, is the concentration of recombination centers (holes in centers), (cm^{-3});

n, is the number of trapped electrons in the material; (cm^{-3})

A_m, is the recombination probability ($cm^3.s^{-1}$);

A_n, is the de-trapping probability ($cm^3.s^{-1}$);

N, is the total number of trapped electrons; (cm^{-3})

n_c, is the number of free electrons; (cm^{-3})

VB is the valence band;

Assuming that the trap is far from saturation i.e. $m >> n$, I is described (Adirovitch 1956) as

$$I = \frac{dn}{dn} = \frac{mA_m ns \exp\left[-\frac{E}{kT}\right]}{NA_n} \qquad (2.9)$$

under the condition $m = n$ i.e. the concentration of recombination center is equal the concentration of electrons in traps

$$I = \frac{n^2 A_m ns \exp\left(-\frac{E}{kT}\right)}{NA_n} \tag{2.10}$$

As using

$s' = sA_m / NA_m$

$$I = -\frac{dn}{dt} = n^2 s' \exp\left(-\frac{E}{kT}\right) \tag{2.11}$$

Where T is the temperature, s is the frequency factor (s^{-1}) and the maximum value of s corresponds to the lattice vibration frequency; i.e. 10^{12}–10^{14} s^{-1}., E is the activation energy and k is the Boltzmann's constant.

In thermo-luminescence, the trapped electrons are released following the first order kinetics and single depth theory of Randall-Wilkins which describes TL intensity, I, at any temperature and is directly proportional to the de-trapping rate:

$$I = -c\left(\frac{dn}{dt}\right) = cpn \tag{2.12}$$

Where c is a constant which can be set to unit and the linear heating rate and p is the probability rate that an electron will escape. If the material is heated at a uniform rate β where $\beta = dT / dt$, from which $dt = \frac{dT}{\beta}$ or $\frac{dn}{dt} = -\beta \frac{dn}{dT}$

from equation 2.11

$$-\beta \frac{dn}{dT} = n^2 s' \exp\left(-\frac{E}{kT}\right) \text{ or } \frac{dn}{dT} = \frac{n^2 s'}{\beta} \exp\left(-\frac{E}{kT}\right) \tag{2.13}$$

from which

$$n = n_0 \int_{\tau_0}^{\tau} -\frac{s'}{\beta} \exp\left(-\frac{E}{kT}\right) dT \tag{2.14}$$

Where n_0 = number of trapped carriers at $t = 0$

from 2.8, 2.12, 2.14

$$I(t) = cnp$$

$$= cns \exp\left(-\frac{E}{kT}\right)$$

$$= cn_0 s \exp\left(\frac{-E}{kT}\right) \int_{\tau_0}^{\tau} -\frac{s'}{\beta} \exp\left(\frac{-E}{kT}\right) dT \tag{2.15}$$

A plot of I against T, the glow curve yields a bell shaped curve with a maximum intensity at a characteristic temperature known as the glow peak.

The integrated light sum (S)

$$S = \int_0^{\infty} I dt$$

$$= \int_0^{\infty} -p \frac{dn}{dt} dt$$

$$= \int_{n_0}^{n} -pdn = pn_0 \tag{2.16}$$

As long as p remain constant, the integrated light sum is proportional to the initial number of trapped charges.

2.4.1 Experimental measurement of Thermo-luminescence (TL) emissions from CVD diamond

The diamond samples were each irradiated with the Sr-90 within a controlled exposure time of 1 minute. The thermo-luminescence (TL) measurements were carried out by placing the irradiated samples into a TLD reader; model Toledo 654 TLD (Fig.2.6). The temperature was ramped up to 300^{o}C for the luminescence emission to be measured. The integrated response from each sample was recorded as arbitrary counts.

The TL emission results are shown in Table 2.1.



Figure 2.6: The TLD reader, model Toledo 654 TLD Thermo-luminescence unit

2.5 Ultraviolet (UV) absorption in diamond

The dipole moments of the atoms of CVD diamond changes due to absorption of light of certain energies, and the transitions occur due to absorption of ultra violet radiation. Ultra violet spectroscopy was used to classify the diamond with nearest neighbour nitrogen

substitution forms Ns-N_s^o that forbids light photon absorption measurements (Iakoubovskii et al., 2002) and the 4Ns-V complexes determined by UV absorption with a sensitivity of approximately 1 ppm. The UV absorption is associated mainly with the planar <100> defects of unknown structure, which are determined by a high-resolution microscope as observed by Wight et al. (1971). In ultra violet (UV) measurements the dipole moments of the molecules changes due to absorption of light of certain energies, and the transition that occurs due to absorption of ultra violet radiation which happens if the transition integral is nonzero (Herzberg, 1945).

2.5.1 Experimental measurement of Ultraviolet (UV) absorption for characterization of CVD diamond

Ultraviolet (UV) measurements were undertaken using a Varian Cary UV-Vis-NIR Spectrometer (Fig. 2.7). Each of the samples were beam scanned covering the UV range between 200 nm and 350 nm and compared with a reference beam for each of the UV values. The relative absorbance values were recorded at an absorption edge of 230 nm. Figure 2.8 shows a typical UV scan plots from which UV absorption (A) values for each sample were obtained from equation 2.11.

$$A = \int_{band} \alpha_\nu \, d\nu = \frac{1}{pl} \int_{band} \ln\left(\frac{I_{o,\nu}}{I_\nu}\right) d\nu \qquad (2.11)$$

Where I_ν is the intensity of the transmitted light by the specimen (CVD diamond) of length l containing a gas at pressure p, $I_{o,\nu}$ is the intensity of the incident light, the amount of light of frequency (ν) and α_ν is the absorption coefficient for unit pressure. The integration was calculated at 230 nm frequency region of the band (Nakamoto 1922).

The results of which are tabulated in Table 2.1.



Figure2.7: Ultraviolet scanner model Varian Cary UV-Vis-NIR used for UV absorption

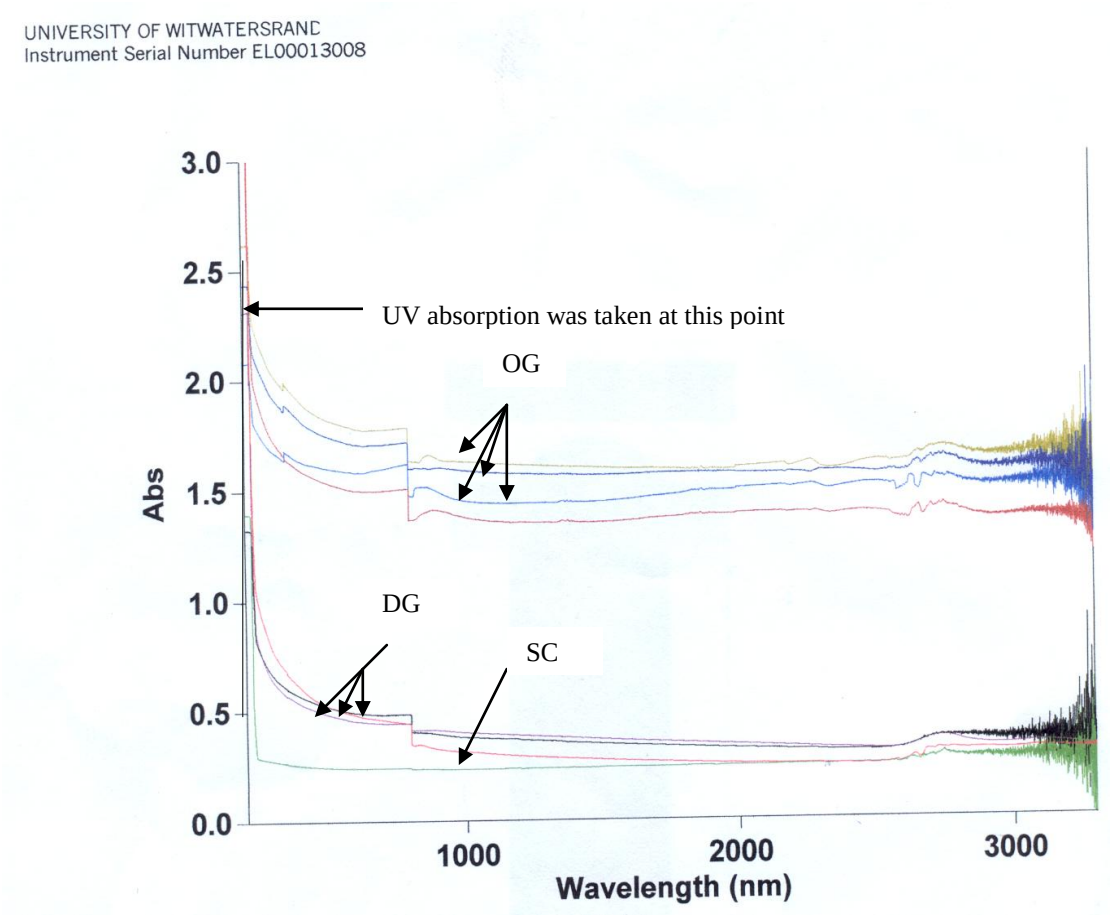


Figure 2.8: The UV scan graphs obtained from OG, DG and a SC CVD diamond wafers

2.6 Metallization of CVD diamond samples

The samples were acid cleaned before metallization was carried out with, in the order, titanium (strong carbide former), platinum (weak carbide former), and gold (non carbide former) i.e. Ti/Pt/Au layers, 200Å: 200Å: 2000Å in thickness respectively, to form ohmic contacts (Tachibana and Glass, 1993) on the two polished and opposite surfaces of the diamond. The diamonds were all in wafer form with the dimensions of 5 x 5 x 1 mm^3 and 5 x 5 x 0.5 mm^3, for the polycrystalline and single crystal respectively. Gold is chemically inert and prevents oxidation from occurring and thus preventing the chemical reaction between the contact and oxygen. The metalized samples were annealed in a ceramic vacuum furnace environment of 10^{-6} torr.

2.7 Measurement of alpha particle interaction with the CVD diamond detector

Finally the CVD diamond was placed 2.2 cm from a 3.7 x 10^6 $Bq.cm^{-2}$ Am-241 alpha source for the acquisition of the alpha spectrum using a PC based commercial software APTEC.

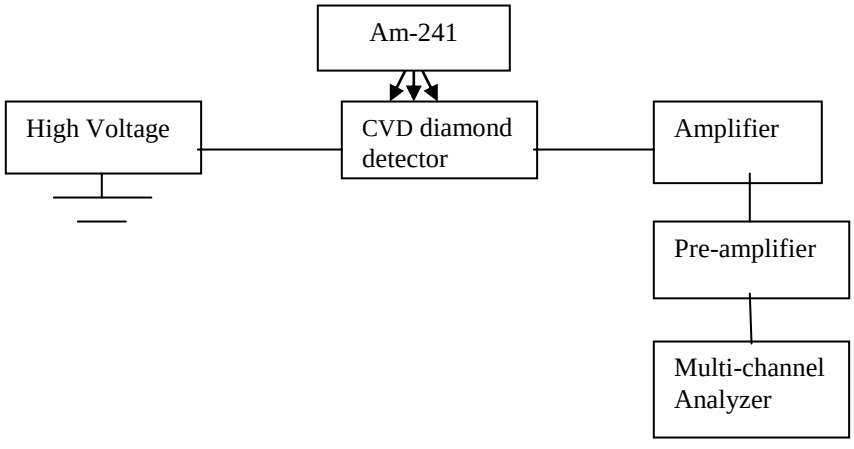


Figure 2.9: block diagram of the experimental set-up

The number of α-particles impinging on the surface of the wafer per second was estimated to be 4.84 x 10^4. The CVD diamond probe with bias voltage of 100 volts, applied across the opposing metalized surfaces (polarization or space charge occurred: space charge is removed by creating a 'injection hole' Konorova and Kozlov, 1971) was then connected to a locally designed and manufactured preamplifier (Fig. 3.2) and the whole system, including the alpha source, was placed in a vacuum chamber (Fig. 3.3). The preamplifier was coupled to an oscilloscope for a pre-assessment of the signal and a personal computer with the APTEC software for data acquisition, processing and analysis. The peak value of each spectrum was equated to the alpha energy peak (5.48 MeV) to evaluate the energy per channel for a plot of the calibrated graphs. The spectrum was used to analyze for resolution and for peak and absolute efficiency of the detectors using the total counts, FWHM and the area under the spectrum peak, and the results are tabulated in Table 2.1. A detailed description of the experimental setup as well as explanation of the method used in the analysis is discussed in Chapter 3.

2.8 Results and discussion

General observations of the results summarized in Table 2.1, Fig. 2.10 to 2.13 depicts the different spectral pattern from the different diamond types when exposed to α-particles. The UV values, single substitutional nitrogen concentration, TL values, to some degree the extent of Raman broadening, and values reflecting absolute efficiency results can be separated into three groups, which themselves can be associated with the different grades of detectors investigated as OG, DG and SC. The single substitutional nitrogen concentration in the polycrystalline specimens (3.5 - 71 ppm) is observed to be higher

than that observed in the single crystal specimen (below 1 ppm). The same variation in trend is observed in the UV absorption and Raman spectral broadening of the samples. The different grades of polycrystalline also indicate a difference in their single substitutional nitrogen contents, UV absorption and Raman spectral broadening. The Optical Grade CVD diamond was observed to have higher UV response (3.48-3.86 cm^{-1}) than the Detector Grade samples (0.51 – 1.93 cm^{-1}).

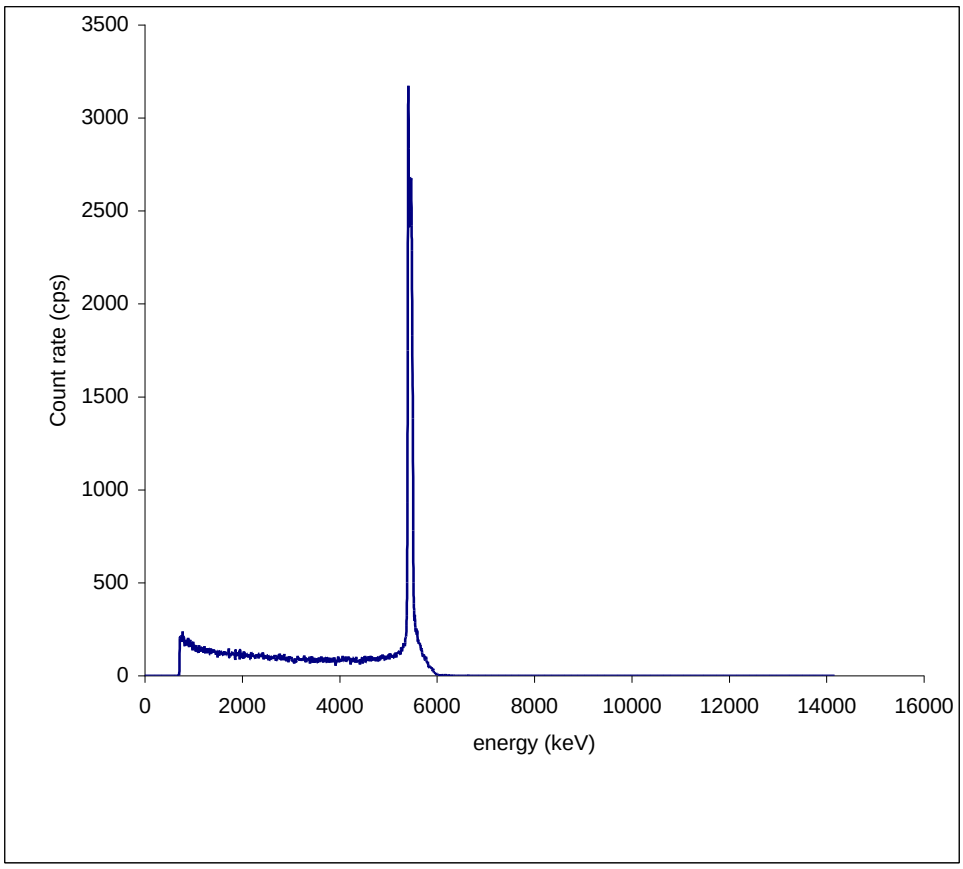


Figure 2.10: The α-spectrum from the Single Crystal CVD diamond detector

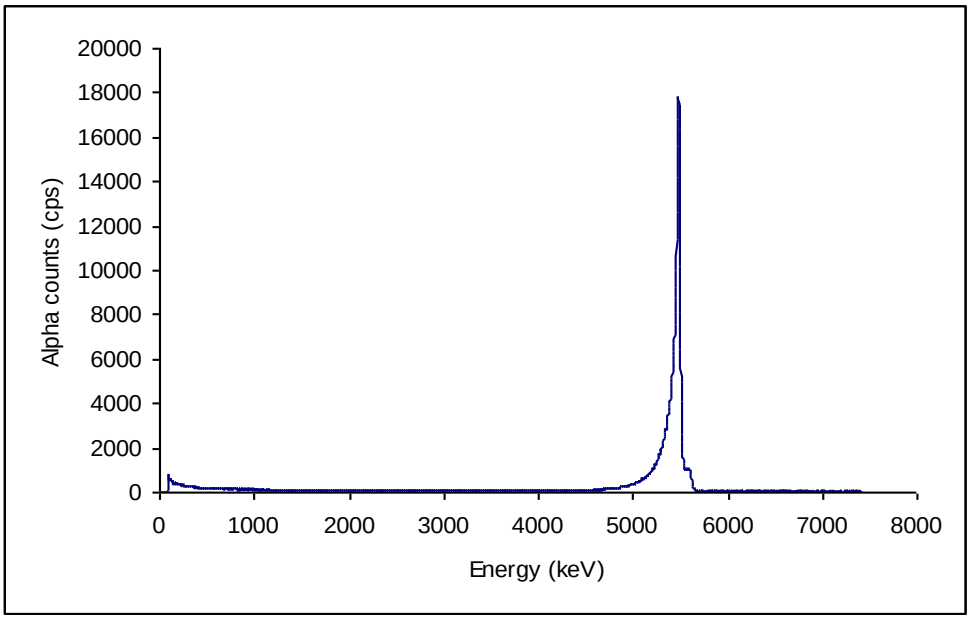


Figure 2.11: The α-spectrum from the (DG3) CVD diamond detector

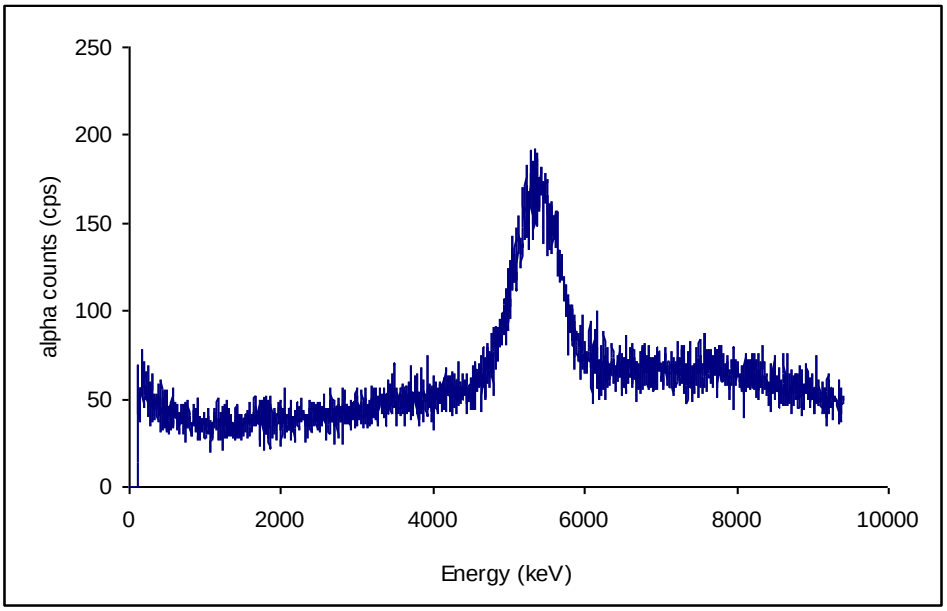


Figure 2.12: The α-spectrum from the Detector Grade CVD diamond

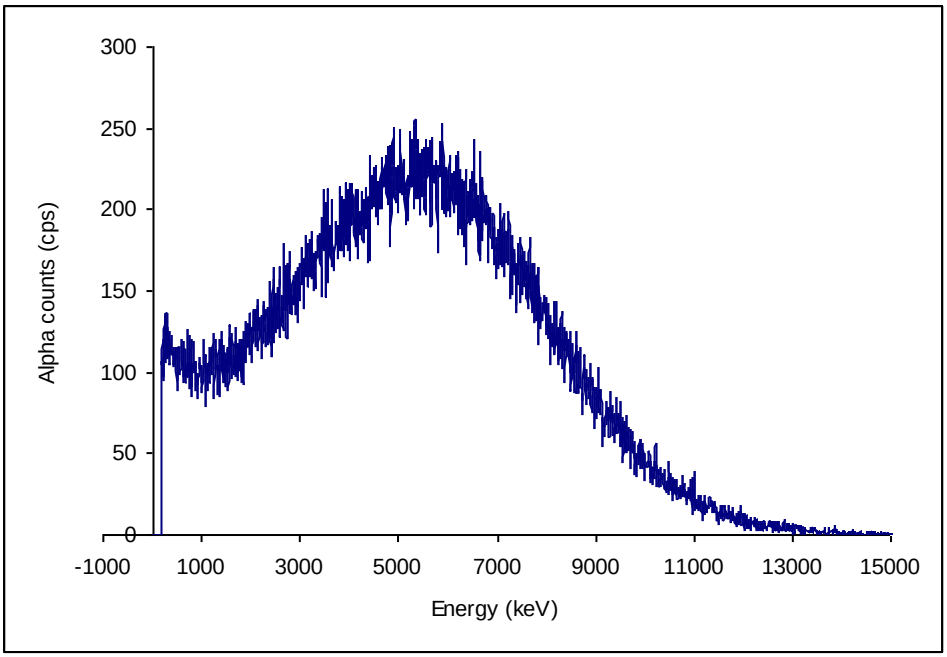


Figure 2.13: The α-spectrum from the Optical Grade CVD diamond detector

The TL response was an exception to the above trend, where the luminescence response of the Detector Grade was observed to be higher (814 – 2024 arb. units) than the luminescence response of the Optical Grade (83 -155 arb. units). Higher TL values generally indicate a larger number of the charge carriers created by the impinging alpha particles. These charge carriers are available for capture at trapping/luminescence centers and for collection should a field be applied across the detector. The observed improvement in energy resolution of the Detector Grade, in general, and DG3 in particular, with its relatively better alpha response can be attributed to their fewer defects and lower single substitutional nitrogen concentrations. The overall performance of the Single Crystal CVD diamond and the conclusions of Pomorski et al., (2006) support the importance of low defect levels. The Single Crystal CVD diamond maintained its comparatively lower response with the TL (25 arb. units) despite a relatively low

concentration of Ns centers. This may be attributed to the concomitant low levels of luminescence related defects in its matrix. It is suggested that the much higher TL values of DG3 reflects not only the availability of charge carriers but the effectiveness of the capture/release mechanism.

The alpha spectrum analysis performed with the full width half maximum (FWHM) value $\Delta E/E$ where ΔE is the spectrum width at half the maximum ordinate of the peak value and E is the value of the alpha spectral peak (5.484 MeV) was calculated. The energy resolution ΔE of the detector's spectrum is an indicator of the quality of the detector material, as it reflects the impurity and homogeneity of the crystal structure and is strongly related to the carrier life-time and thus the charge collection efficiency (Pomorski et al., 2006). The Single Crystal was observed to have FWHM (85.3 ± 0.9 keV) when compared with the polycrystalline FWHM of between 672.5 keV to 7465.9 keV with an exception of one Detector Grade member namely DG3 with a FWHM of 64.1 keV. This is as depicted in Fig. 2.8 for the Single Crystal and Fig. 2.9 for the polycrystalline Detector Grade CVD diamond DG3.

The alpha response of the polycrystalline also shows a difference between the Detector Grades Fig. 2.11 and the Optical Grades Fig. 2.12. The differences in peak resolution could partly be caused by the spread of the electric field along the material due to its polycrystalline nature having non-uniform geometry and thickness (Tromson et al., 2000). It could also be partly due to the capture/release mechanism of trapping levels inducing a space charge build up of internal electric fields leading to the observed

spectral broadening (Souw et al., 1997). The observed absolute efficiency of all Optical Grade detectors between 80 % to about 100 % is consistent with the observed broadening of their peak resolution above 100 %, and this, it is proposed a result of the polarization effects causing a build-up (pile-up) of e-h pairs, coupled with the greater thickness (500 μm) of the detectors used (Souw et al., 1997; Bergonzo et al., 2001; and Liechtenstein et al., 2004). This is supported by the observed drifting of the spectrum peak during spectra acquisition. Within the specimen, of the Optical Grade detectors is their comparatively lower charge carrier effect due to impurities in CVD diamond samples, as observed from their TL response and higher UV absorption effect.

The earlier observed better peak resolution of the detector grade CVD diamonds was also found to be consistent with their energy peak efficiencies of 80 %, and also consistent in performance with the Single Crystal (80 %) CVD diamond (DG3 in particular) as a spectrometer. The absolute efficiency calculated as the ratio of the total alpha counts from the detectors to the source strength within the area of the active zone was also used to study the characteristic performance of the CVD diamond detectors. The Single Crystal had fewer impurities and was the least efficient absolutely (52 %).

The Optical Grade diamonds, with the relatively higher number of impurities detected by both UV and ESR, indicated a higher efficiency of between 80 % to above 100 %. This is consistent with the reason for their poor peak resolution as a consequence of polarization effects causing the build-up of internal electric fields. For the Detector Grades the absolute efficiency of between 62 % and 68 % is consistent and is closely related to the

single crystal in their performances. In comparison to the Optical Grade CVD, this may be attributed to their lower defect/impurity levels with reduced resulting build-up effects. Of note is the observation that low single substitutional nitrogen levels were found to have no significant effect on the carrier life-time (Sellin et al., 2007). In comparison to the OG the observed lower efficiency of the Single Crystal (48 %) may be due to its overall lower defect concentration (Souw et al., 1997; Bergonzo et al., 2001).

The graphical (Fig. 2.14 to 2.22) results depict the correlation of the different methods used, and an examination of the correlation between the results of the Raman broadening, thermo-luminescence and electron spin resonance (single substitutional nitrogen) and with alpha counts of the CVD diamond film is reported. Figure 2.14 indicates a correlation with positive gradient between the UV absorption of the diamond samples and the total alpha counts. The UV absorption of the Optical Grade CVD diamond was found on the average to be approximately 3 times greater than that of the Detector Grade CVD diamonds with absorption at 1.3 ± 0.69 cm^{-1}. An appreciable amount of a non-diamond phase impurities and structural defects (nitrogen complexes or UV related impurities) that commonly exist in CVD could be ascribed to the different absorption response of diamond to UV absorption (Wang et al., 2005). The Raman broadening due to the N_S defect centers in each of the Optical Grade samples we believe can be related to the alpha response of Optical Grade CVD diamond detectors. This is shown in Fig. 2.15, where the observed correlation appears to be of a negative gradient is observed for the Optical Grade CVD diamonds.

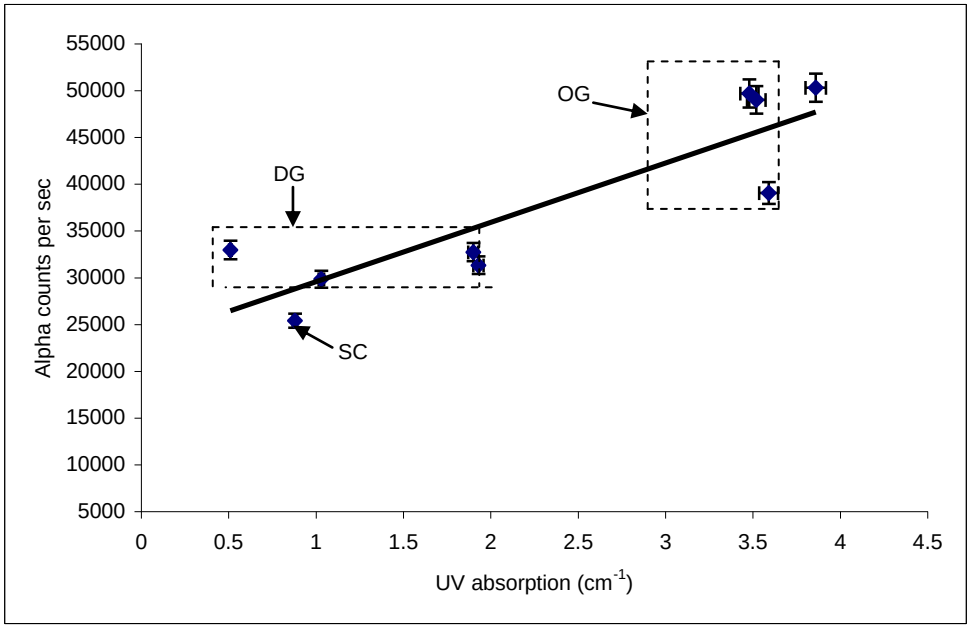


Figure 2.14: Variation of total alpha counts with UV absorption for Detector and Optical Grade CVD diamonds

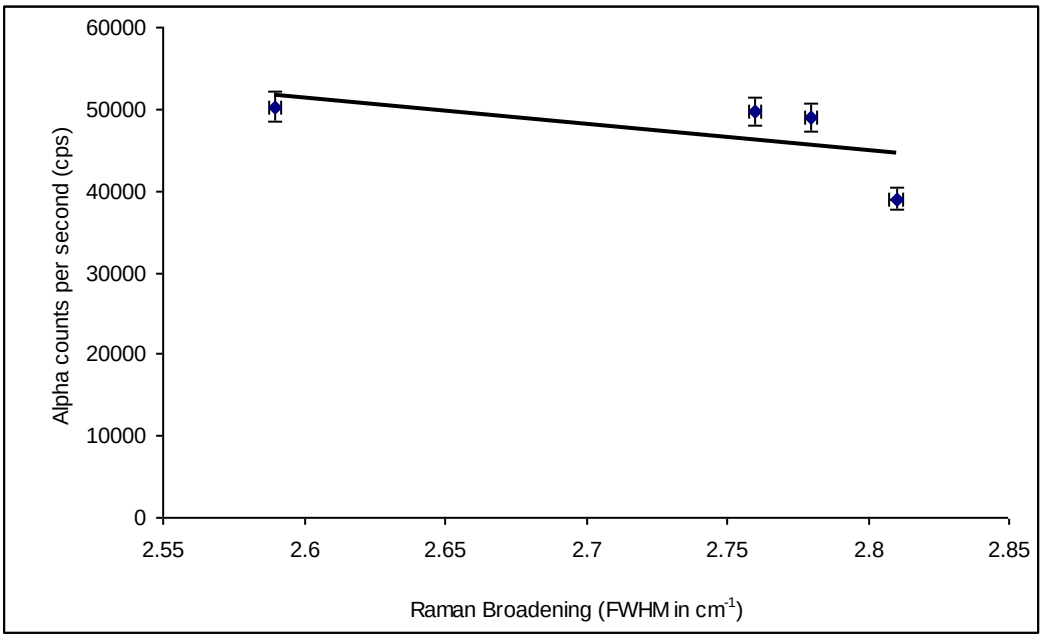


Figure 2.15: Variation of total alpha counts with Raman broadening for Optical Grade CVD diamonds

Variation of alpha counts with single substitutional nitrogen concentration of Detector Grade CVD diamond samples is depicted in Fig. 2.16. The correlation of the alpha count

with ESR (single substitutional nitrogen concentration**)** is with a negative gradient. This confirms the general trend of observations by Nam et al. (1991) that, for a class of crystals, the concentration of single substitutional nitrogen is inversely related to its response to the impinging radiation. Figure 2.17 shows an inverse relationship between Ns centers and UV absorption for the Optical Grade CVD diamonds, implying therefore the interplaying effect of that extra nitrogen introduced in the synthesis process has on the concentration of both the UV type impurities and Ns centers (Sellin et al., 2007; Souw et al., 1997). The consequence on the Optical Grade detectors in particular was the observed higher alpha counts. We were informed that extra nitrogen was added to the Optical Grade CVD diamond used in this investigation (private communication).

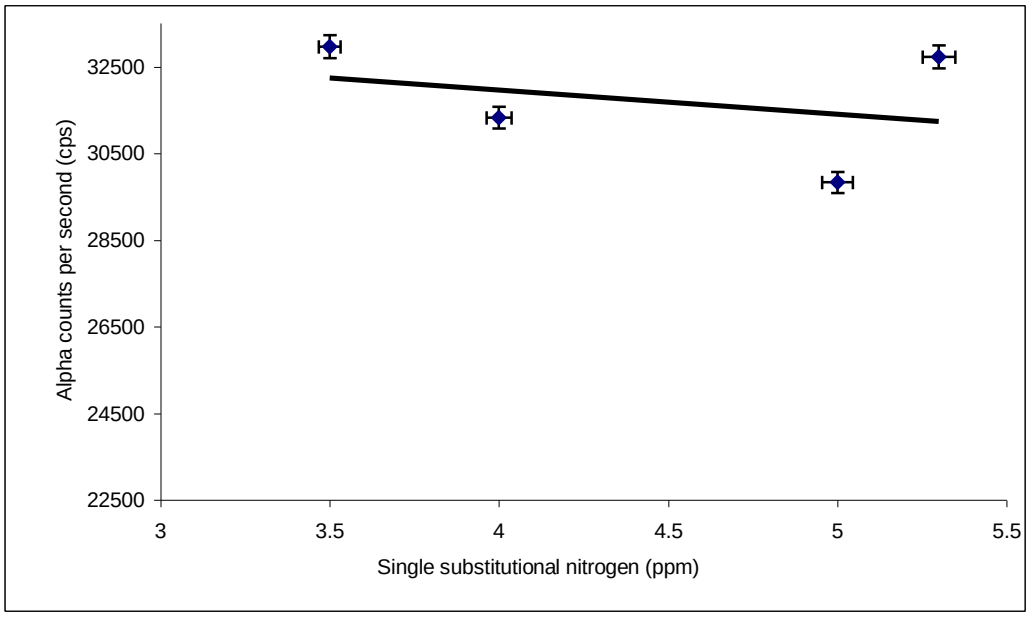


Figure 2.16: Variation of total alpha counts with TL response for Optical Grade CVD diamonds

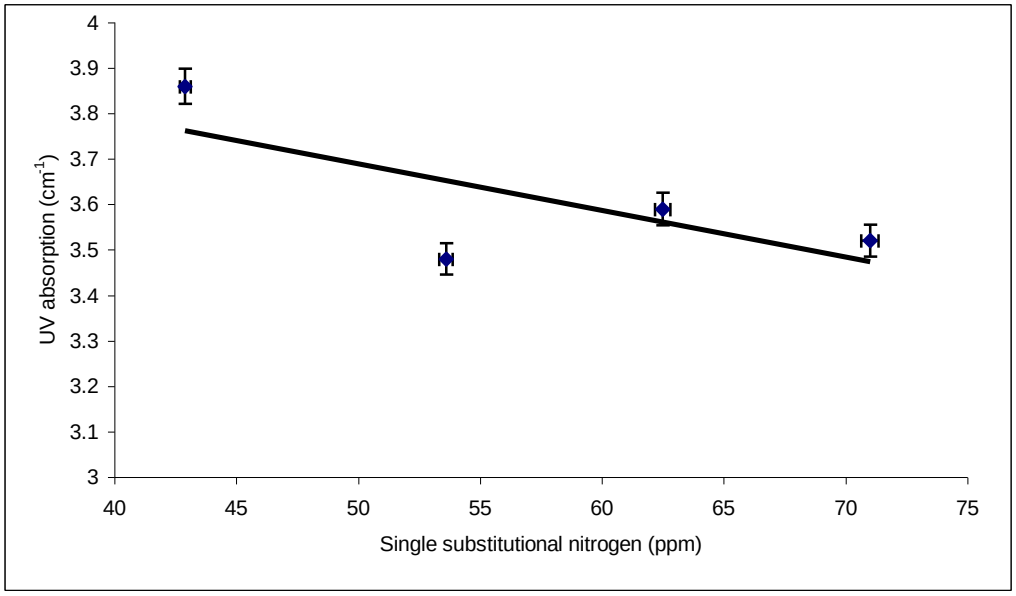


Figure 2.17: Variation of total alpha counts with single substitution nitrogen concentration (using ESR) for Detector Grade CVD diamonds

Figure 2.18: shows a spline function relation between the single substitutional nitrogen concentration and the thermo-luminescence response of the polycrystalline CVD diamonds. Behaviour similar to this was also observed by Benabdesselam et al., (2001). Figure 2.18 shows that the lower single substitutional nitrogen concentrations (ESR) results in the higher thermo-luminescence emission. The explanation of a lower TL response of optical grade CVD diamond is however believed to be due to the higher single substitutional nitrogen concentration which result in non-radiative recombination and not the number of trapping levels within the samples (Nam et al., 1991). The model explains the effect of decrease in Ns concentration in diamond to TL response in relation to other defects, traps and recombination, and the result is observed in this analysis.

The broadening of the spectrum leading to increased FWHM could be attributed to a combination of a more defective crystal lattice (trapping/de-trapping at grain boundaries) and higher concentration of nitrogen complexes (Fish et al., 1999).

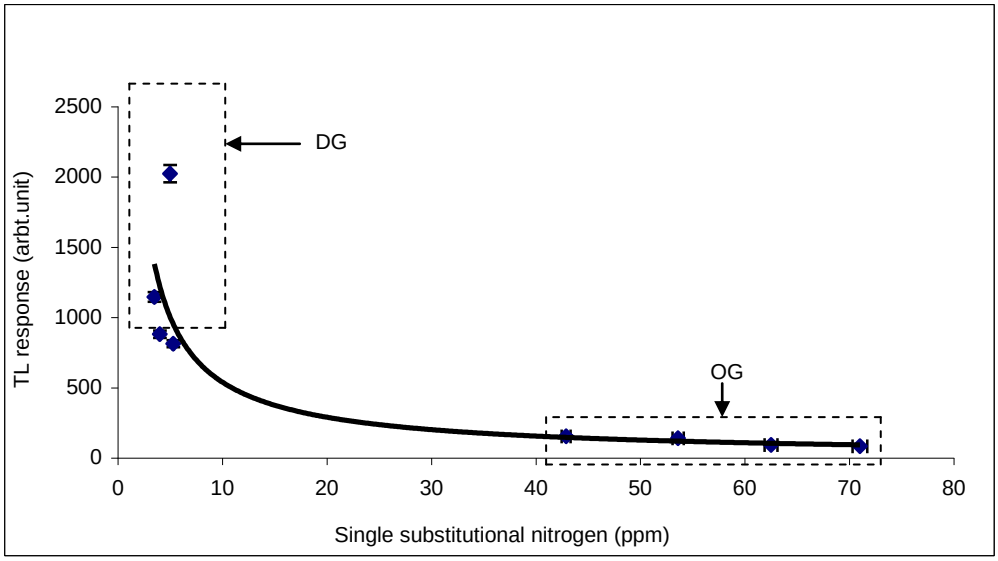


Figure 2.18: Variation of thermoluminescence response with single substitution nitrogen concentration (using ESR) for Detector and Optical Grade CVD diamonds

Figure 2.19 is a plot of TL emission in relation to Raman broadening for an Optical Grade detector, showing that as the Raman effect increases the TL response drops. This may be due to presence of traps and recombination at grain boundaries. The observed correlation of UV absorption and Raman broadening with FWHM of alpha peaks for all detectors Fig. 2.20 and Fig. 2.21 relates to the contributions of the defects associated with the UV absorption and defects giving rise to the Raman broadening and to the relatively larger broadening of the alpha spectra from the Optical Grade CVD diamonds. This shows the overall effect of the detector with FWHM having a positive gradient to

increase in the single substitutional nitrogen concentration as observed in Fig. 2.22 and implied in Fig. 2.17 with broad spectrum of the Optical Grade CVD diamond detectors.

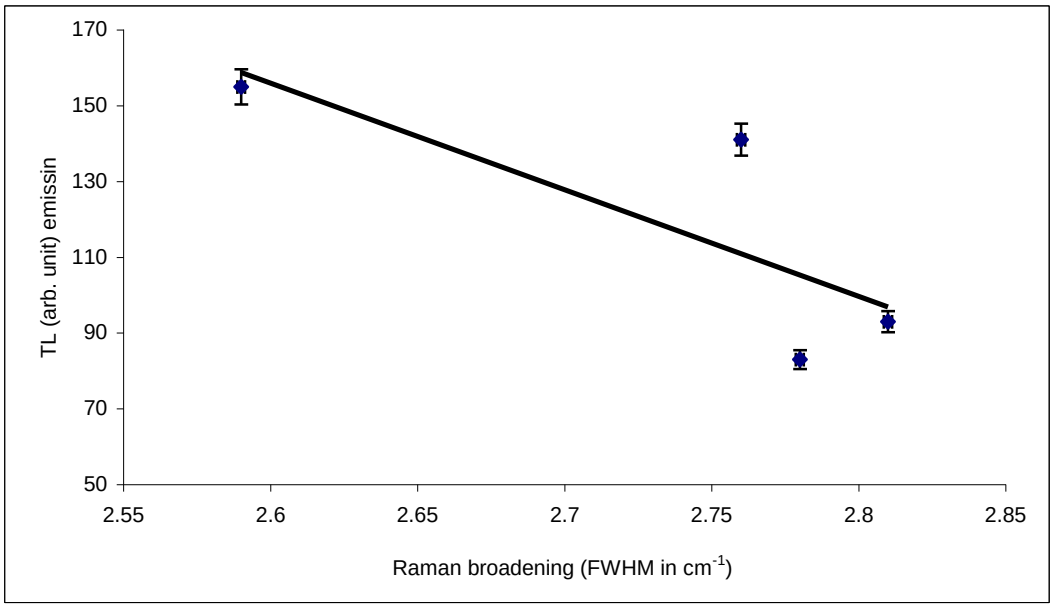


Figure 2.19: Variation of TL emission with Raman broadening for Optical Grade CVD diamonds

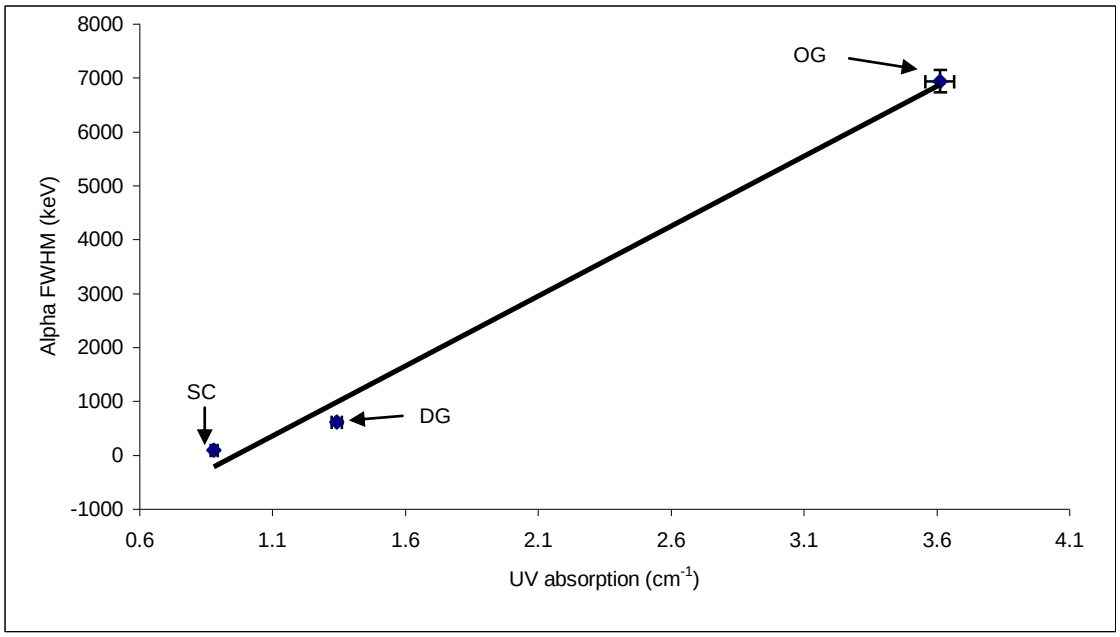


Figure 2.20: Variation of FWHM of alpha counts with averaged UV absorption values for both Detector and Optical Grade and Single Crystal CVD diamonds

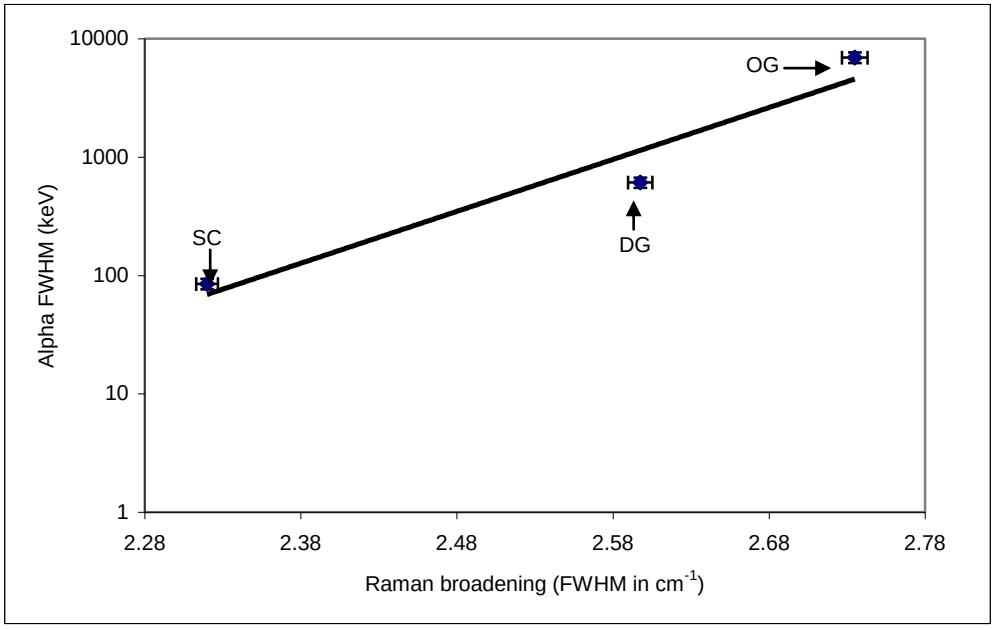


Figure 2.21: Variation of FWHM of total alpha counts with averaged Raman broadening values for both Detector and Optical Grade and Single Crystal CVD diamonds

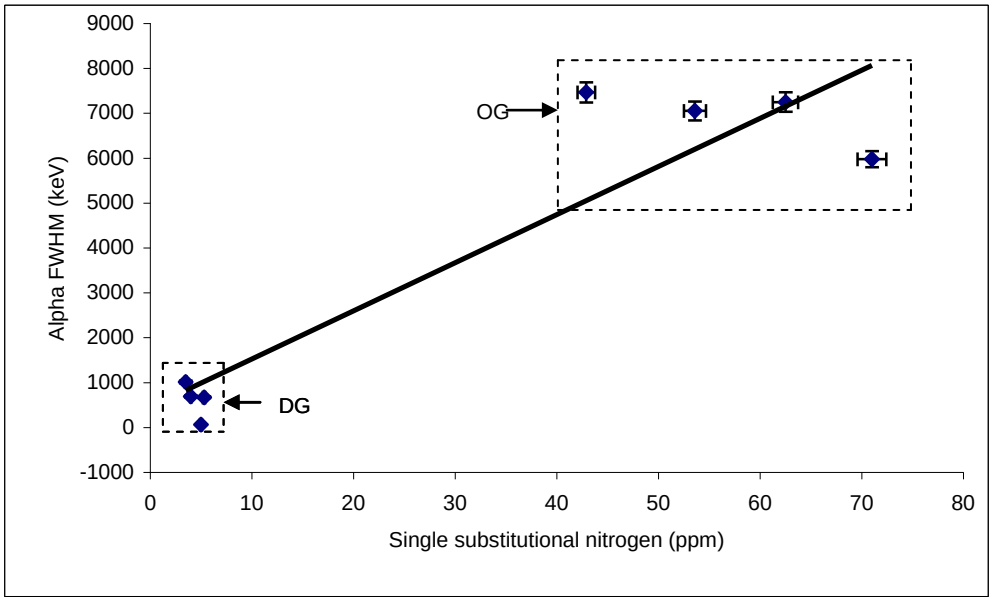


Figure 2.22: Variation of alpha FWHM with single substitution nitrogen concentration for Detector and Optical Grade CVD diamonds

2.9 Summary and conclusions

It is seen that there is a consistent trend of the alpha counts having a positive gradient with UV absorption and TL emission, but a negative gradient to the Raman broadening and single substitutional nitrogen concentration. The relatively high total alpha counts from the Optical Grade CVD diamond may be associated with a greater concentration of UV related defects and build-up effect. As in HPHT crystal, single substitutional nitrogen in CVD diamonds act as recombination centers. In general the higher sensitivity (counting efficiency) is associated with a lower concentration of single substitutional nitrogen and hence, contributes to the lowering of the alpha counts as observed in the Detector Grade, Optical Grade and Single Crystal CVD diamonds. For reasonable alpha spectroscopy this study shows that the value of nitrogen concentration, UV absorption and Raman broadening must be as low as possible, but the highest TL value. In general the SC Grade is the material of choice for general alpha spectroscopy (Pomorski et al., (2006). However, if one wants a detector of higher sensitivity, similar resolution, better peak efficiency and less expensive, selection of CVD materials using TL as a post selection tool may be the route to take; otherwise if the interest is not in spectroscopy but merely a sensitive alpha detector, CVD diamond of the Optical Grade is a material of choice.

2.10 References

Adirovitch EIA 1956. *J. Phys. Rad.* **17** 705

Araikum S 1993. *Masters thesis. University of the Witwatersrand, Johannesburg, South Africa*

Benabdesselam M, Iacconi P, Butler JE and Briand D 2001. *Diamond and Related Materials* **10** 2084

Bergonzo P, Tromson D, Mer C, Guizard B, Foulon F and Brambilla A 2001. *Phys. Stat. Sol.* **(a)185(1)** 167

Davies G 1999. Physica **B273** 15

Dean PJ 1965. *Phys. Rev.* **139** A588

Doverspike K, Butler JE and Freitas Jr. JA 1993. *Diamond and Related Materials* **2** 1078

Fallon PJ 1989. *MSc. Dessertation, University of the witwatersrand*

Fish ML, Massler O, Reid JA, MacGregor R, and Comins JD 1999. *Diamond and Related Materials, **8(8-9)*** 15114

Gerrish VM 1995. *Simiconductors Semimetals* **43** 493

Hammersberg J, Isberg J, Johansson E, Lundström T, Hjortstam O and Bernhoff H 2001. *Diamond and Related Materials* **10** 574

Hecht K 1932. *Z. Phys.* (Berlin) 235

Herzberg IG 1945. *Infrared and Raman Spectra of Polyatomic Molecules, Van Nostrand Reinhold, New York.*

Iakoubovskii K and Stesmans A 2002. *J. Phys.: Condens. Matter* **14** R467

Iakoubovskii K, Andriaenssens GJ and Cohra YK 2000. *J. Phys.: Condens. Matt**er*** **12** L519

Isberg J, Hammersberg J Hohansson E, Wilstrom T, Twitchen DJ, Whitehead AJ, Coe SE and Scarsbrook GA 2002. *Science* **297** 1670

Khan FM 2003 *The Physics of Radiation Therapy, Lippincott Williams & Wilkins*

Kittel C 1986. *Introduction to Solid State Physics John Wiley & Sons, New York*

Konorova EA and Kozlov SF 1971. *Sov. Phys. Semicond.*, **4(10)** 1600

Kuo MT, May PWGunn A, Ashford MNR and Wild RK 2000. *Diamond related Materials* **9** 1222

Kuo MT, May PW and Ashford MNR 2001. *Diamond related Materials* **10** 889

Lakowicz, J.R., 1983. *Fluorescence polarizatio. In: Principles of Fluorescence Spectroscopy. Plenum, New York*

Liechtenstein VKh, Eremin NV, Golser R, Kutschera W, Paskhalov AA, Priller A Steier P, Vockenhuber C and Winkler S 2004. *Nucl. Instrum. and Methods in Phys. Research* **A521** 203

Lin LTS, Popovici G, Mori Y et al., 1996. *Diamond and Related Materials* **5** 1236

Manfredotti C, Fizzotti F, Polesello P, Vittone E and Wang F 1996. *Phys. Stat. Sol.* **154** 327

Nakamoto K 1922. *Infrared and Raman Spectra of inorganic and coordination compounds.* A Wiley-*Internscience Publication. John Wiley & Sons. New york. Chichester. Brisbone. Toronto. Singapore*

Nam TL 1989. *PhD thesis, University of the Witwatersrand, Johannesburg, South Africa.*

Nam TL, Karfunkel U, Keddy RJ and Every AG 1991. *Radiation effect and defects in solids* **116** 233

Nebel CE 2003. *Semicond. Sci. Technol*. **18** S 1

Pomorski M, Berdermann E, Caragheopol A, Ciobanu M, KišM, Martemiyanov A, Nebel C and Moritz P 2006. *Physica Status Solidi* (**a)203(12)** 3152

Ruan J,Kobashi K and Choyke WJ 1992. *Appl. Phys. Lett.* **60(25)** 3138

Schreck M, Hörmann F, Roll H, Lindner JKN and Stritzker B 2001. *Appl. Phys. Letters* **78(2)**192

Sciortino S 1999. *Riv. Nuovo Cimento* **22** 1

Seitz F 1938. *J. Chem. Phys*. **6** 150

Sellin PJ, Lohstroh A, Davies AW, Galbiati A, Parkin J, Wang SG and Simon A 2007. Nucl. Instrum. and Methods in Phys. Res. **B260** 293

Snail KA, Vold CL Marks CM and Freitas Jr. JA 1992. Diamond and Related Materials **1** 180

Souw EK and Meilunas 1997. *Nucl. Instrum. and Methods in Phys. Research* **A400** *69*

Stern O 1922. *Z. Phys* **9** 353

Tachibana T and Glass JT 1993. Diamond Related Materials 2 963

Taylor WR, Canil D and Milledge HJ 1996. *Geochim. Cosmochim. Acta* **60** 4725

Tromson D, Brambilla A, Foulon F, Mer C, Guizard B, Barrett R, and Bergonzo P 2000. *Diam. Relat. Mater.* **9** 1850

Wang-L, Lou Y, Su Q, Shi W and Xia Y 2005. *Optics Express* **13 (12**) 8612

Wertz JE and Bolton JR 1986. *Electron Spin Resonance. Elementary Theory and Practical Applications. , Academic Press, London, New York.*

Wight DR, Dean PJ, Lightowlers EC and Mosby CD 1971. *J. Lumin.* **4** 169

Chapter 3

COMPARATIVE EVALUATION OF THE INHERENT SPECTROMETRIC PERFORMANCES OF CVD DIAMOND DETECTORS EXPOSED TO α-PARTICLES RADIATION AFTER SPECTRA BACKGROUND SUBTRACTION

3.0 Abstract

This Chapter reports on the outcome of the procedure used to remove the background noise levels from the 'as accumulated' experimental alpha spectra of nine Chemical Vapour Deposition (CVD) diamond wafers when used as detectors of impinging 5.48 MeV α-particles. The spectra, each with different spectrum width/peak broadening attributable to the presence of defect/impurity concentration were analyzed for statistical noise and fluctuations. The objective was to provide consistent spectra resolution necessary for a comparative spectrometric analysis to be performed on the detectors under investigation. The diamond wafers broadly classified as Detector Grade (DG), Optical Grade (OG) polycrystalline and Single Crystal (SC) CVD diamonds were in terms of impurities/defect levels characterized in Chapter 2. The detectors leakage current was measured and its contribution to the noise level analyzed. The poor spectra resolution was reported to be due not only to difference in defects concentration but also to background statistical effect and noise levels.

The observed effect of defects on the experimentally acquired spectrum was analyzed after the background subtraction. For spectrum background subtraction the software program Origin 6.1 was used. The full width half maximum (FWHM) and resolution of each spectrum was calculated from a Gaussian fit and the absolute efficiency analyzed.

3.1 Introduction

The experimental results of Chapter 2 not only highlighted the poor peak resolution but using the 'as accumulated' data, gave absolute peak efficiencies above 100 % for the

Optical Grade wafers. This was attributed not only to difference in defect concentration but also to background statistical effects, pile-up effect and noise levels. There is therefore the need to correct for these anomalies that would provide the bases for the performances of the different diamonds Grades when used as alpha particle probes, to be consistently evaluated.

3.2 Brief literature review

In this work diamond detector consists simply of a diamond (100-1000 μm thick) that is metallized on both sides with high voltage bias electrodes to collect the charge carriers (electrons and holes) produced by ionizing particles (Berdermann et al., 2001). In spite of the demonstrated poor detection characteristics as compared to silicon based devices, the extremely large band gap of about 5.5 eV, leading to low leakage current and resulting in extremely low noise, motivates a further test on diamond (Marinelli et al., 2001). Historically, natural diamonds with suitable electronic properties were used for radiation detection but the high cost and the difficulty in selecting a suitable detector limits the availability of the diamond (Kozlov et al., 1977).

The promising technology for synthesis of diamond material is the Chemical Vapour Deposition (CVD) technology. Most previous diamond particle detector designs were based on artificially grown polycrystalline CVD diamonds. These allowed relatively large (tens of mm^2) and reproducible detectors with count rate capability up to 10^8 particles/sec to be fabricated. The polycrystalline structure with crystallite size of about 10-20% of grown plates however, and crystallites boundaries acts as traps resulting in

decreases in charge collection efficiency (Bauer et al., 1996; Bacci et al., 1998). Also the ability to perform energy spectrometry with CVD detectors has been poor, because of trapping of charge carriers in the grain boundaries. As a result the energy resolution achieved for these detectors has typically been 70 % even for light ions at about 700 MeV. These restricted their application for beam monitoring. Recent advances on the development of single crystals, showed a much better performance as energy spectrometers, with resolution in the range 1-3 % for alpha particles (Kozlov et al., 1975). An estimated range of alpha particles in a CVD diamond was reported as ~13 μm (Akulinichev et al., 2003); with very low leakage current and high resistivity (10^{14} Ωm) reported (Toshisuke et al., 2006). Where the polycrystalline CVD diamond was shown to have much poorer performance when compared with Single Crystal CVD diamond the latter crystal was used to investigate for heavy ion spectroscopy and time of flight (ToF) measurements (Berdermann et al., 2004; and Pomorski et al., 2005).

Single Crystal CVD diamond has opened new application fields in nuclear detection and dosimetry in high energy physics (HEP) such as hadrons radiotherapy and neutron spectroscopy. An unprecedented performance displayed by single crystal where high resolution energy spectrometry of the heaviest elements at high count rate is demanded was reported (Steier et al., 2002; Manfredotti, 2005). Polycrystalline CVD diamond is an interesting radiation detector material for applications where high energy resolution is not required. The spectroscopic performance of CVD diamond radiation sensors is limited by low carrier drift lengths, caused by trapping at crystallite boundaries. An improved drift

length of up to 270 μm in a back-thinned sample (Schottky barrier) has been reported recently (Adam et al., 2003).

An excellent alpha energy resolution of 0.003 for the single crystal CVD diamond spectrum was reported while the highest quality polycrystalline CVD diamond was reported to have energy peak resolution of 0.65 (Berdermann et al., 2004; and Pomorski et al., 2005). Investigations on the effect of the film microstructure on the performance of diamond film as alpha particle detector was reported (Wang et al., 2005) to have a spectrum energy resolution of 1.1 %. Poor peak energy resolution was observed for a polycrystalline as alpha detector (Angelone et al., 2004). The polycrystalline nature of diamond films makes the detector performance strongly dependent on the microstructure of the CVD diamond films (Marinelli et al., 2001). Whilst the (in-grain) defects can be saturated by a pumping (priming) procedure, the boundary defects and shallow trap defects and their effects can only be reduced by improving the film quality (Angelone et al., 2004).

The direct result of a spectrometric measurement is a pulse height distribution not the photon spectrum. For an understanding of the difference, the possible interactions of an incident particle with the detector need to be considered. The general terms of spectroscopy refers to the application of a radiation detector to measure the energy distribution of the incident radiation. The difference in width of spectra reflects the fact that a certain amount of fluctuation was recorded from pulse to pulse even though the same energy was deposited in the detector for each event. If the amount of fluctuation is

reduced the peak approaches a sharp spike (Knoll, 2000). The cause of potential sources of fluctuations in the response of a given detector that results in an imperfect resolution are: the presence of drift in operating characteristics during measurement, sources of random noise within the detector and instrumentation system, as well as the statistical noise arising from the discrete nature of the measured signal itself. Pile-up occurs when two pulses that are close together, sum on top of each other to produce a single pulse with new amplitude. This distorts the energy information and contributes to counting loses (dead time) of the detector system (Sorenson, 1938).

The statistical noise is the most dominant source of fluctuation in signals which sets important limits on the detector performance. The response function should then have a Gaussian shape with the typically large number of charge carriers. The definitions of FWHM as the width of the distribution at a level that is just half the maximum ordinate of the peak and that of the energy resolution as the FWHM divided by the location of the peak centroid are based on the assumption that any background or continuum on which the peak may be superimposed is negligible or has been subtracted (Knoll, 2000). The energy resolution of the detector's spectrum is an indicator of the quality of the detector material, as it reflects the impurity and homogeneity of the crystal structure and is strongly related to the carrier life-time and thus the charge collection efficiency (Pomorski et al., 2006).

The increase in use of radiation as a clinical diagnostic tool in recent years coupled with the demand for improved measurement of the radiation beams to allow for greater control

over treatment motivated this work. In this work the observed experimental peak resolution and absolute efficiency above 100 % for the optical grade detectors (Chapter 2) were analyzed with a view to finding out the true and actual performance of the detectors. Effort is made analytically on improving the spectrum peak resolution by subtracting the background noise (fluctuations) and pile-up effect from the experimental spectrum. A spectrometric comparative analysis of the different Detector Grades is made in relation to their impurity concentration taking into account the alpha interaction (ionization and excitation) processes.

3.3 Experimental procedure

A spectrometer consists basically of a radiation sensing material (detector), a preamplifier (Fig. 3.1) (placed in a vacuum chamber Fig. 3.2), an amplifier system and a multi-channel analyzer connected to a 3.7 x 10^6 Bq.cm^{-2} Am-241 alpha source. A circuit diagram of the pre-amplifier used is shown in figure (3.3). The alpha spectra of 9 CVD diamonds identified by the supplier as Optical Grade samples OG1, OG2, OG3, OG4, Detector Grade samples DG1, DG2, DG3, DG4, polycrystalline and Single Crystal (SC) type wafers were assayed for their response when configured as detectors to impinging alpha particle radiation. Each of the specimens was in wafer form 1x5x5 mm^3 for the polycrystalline and 0.5x5x5 mm^3 for the single crystal.

The procedure for acquiring the experimental spectrum was reported in section 2.7 of Chapter 2. The peak value of each of the acquired experimental spectrum was equated to the alpha energy peak value (5.48 MeV) to evaluate the energy per channel for a plot of

the calibrated graphs to be analyzed. The experimental results of the detector's performance in relation to the effect of their defect were reported in Chapter 2. Using the Keithley 237 unit (Fig. 3.4) for biasing and measuring the output signal over the range 0-1000V, the leakage current of the diamond specimen was measured in order to analyze the differences in noise level of the detectors.



Figure 3.1: Locally designed preamplifier used for alpha spectroscopy

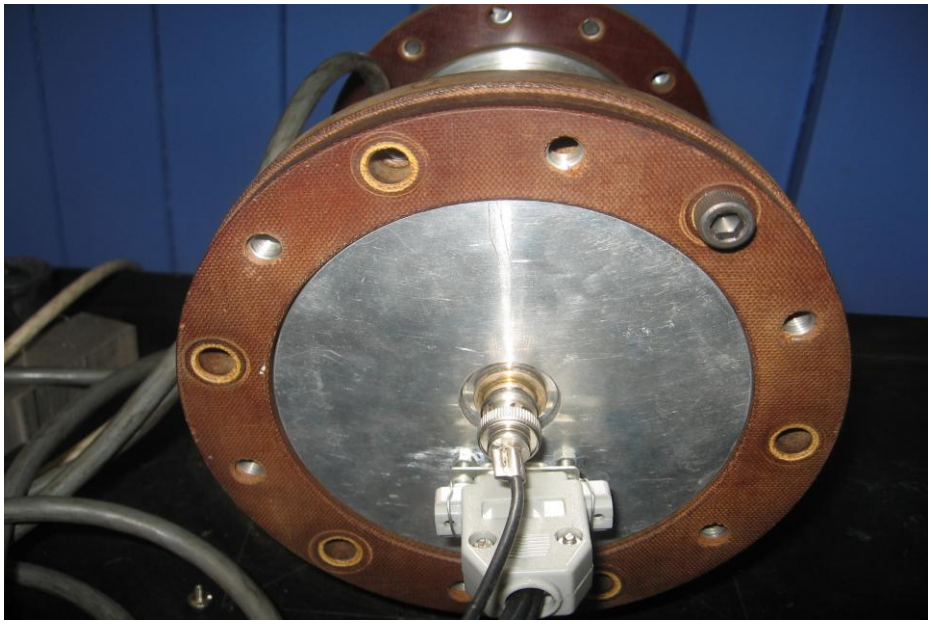


Figure 3.2: End view of the vacuum chamber with preamplifier and Am-241 source placed inside

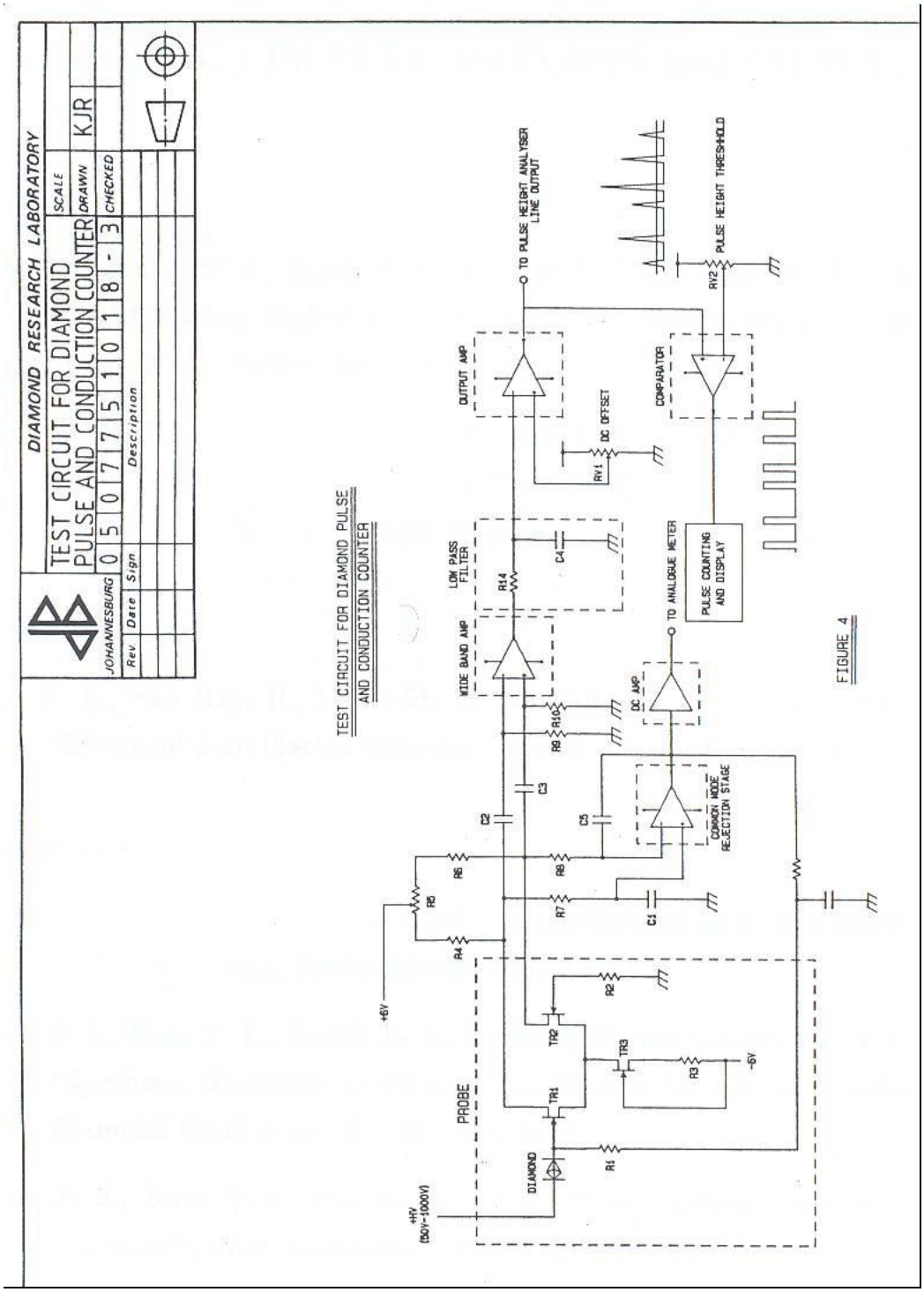


Figure 3.3: Custom built test circuit for diamond pulse and conduction counter (from Fallon, 1989 and Grobbelaar, 1988).



Figure 3.4: Keithley 237 unit and a Faraday cage used for current leakage measurements

3.4 Background subtraction

The observed spectral differences in spectrum broadening, peak resolution and sensitivity arising from the effect of their intrinsic impurities/defects and reported in Chapter 2 was used as an indicator of the quality of the detector material as it reflects the purity and homogeneity of the crystal structure to its performance as a spectrometer or as a dosimeter.

Further analysis on the experimental spectrum was taken to improve the peak resolution. This was done by subtracting baseline fluctuations (spectra continuum, B). In alpha particle interaction (excitation and ionization) with the detector, energy is lost in discrete amounts leading to the observed statistical fluctuations. The same stochastic factors that

lead to energy straggling at a given penetration distance also result in slightly different total path length for each particle (Sorenson, 1938).

3.5 Analytical method

Each experimentally obtained and calibrated alpha spectrum was plotted, analyzed for the total counts and the counts normalized by the time of irradiation. Due to the skewed nature of the spectrum obtained from polycrystalline CVD diamond a baseline was inserted and modified in order to provide for a better Gaussian fit. A background (B) subtraction from alpha spectrum, using the ORIGIN 6.1 software was undertaken by applying the equation (Genie 2000, 2006)

$$B = \sum_{i=1}^{N} \left(\frac{B_1}{n} + \frac{(B_2 - B_1)}{nG} \sum_{j=1}^{i} y_j \right) \tag{3.1}$$

where

y_j , is the counts per channel in channel, i ,

G , is the total sum of counts (gross) in the peak region of interest (ROI);

N , is the number of channels in the peak ROI;

n , is the number of continuum channels on each side of the spectral peak;

B_1, is the sum of counts in the continuum (background) region to the left of the peak; and

B_2 , $_{is}$ sum of counts in the continuum (background) region to the right of the peak.

Equation 3.1 removes statistical fluctuation (background, B) induced by alpha particles when it interacts with matter by photo-electric and Compton scattering.

The Gaussian fitted spectrum was then analyzed (using the ORIGIN 6.1) for spectrum area (S) under a Gaussian curve which was given by

$$S = hZ\sqrt{\pi} \tag{3.2}$$

where

h is the height of the peak, and

Z is a measure of the peak width ($Z^2 = 2\sigma^2$, where σ is the Gaussian width), FWHM (resolution) value as a weighted mean of the individual peak full width at half-maximum values (Genie 2000, 2006) of the calibration peaks was calculated as

$$F_{Av} = C_1 . \frac{\sum_{i=1}^{N} \frac{F_i}{\sigma_{F_i}^2}}{\sum_{i=1}^{N} \frac{1}{\sigma_{F_i}^2}} \tag{3.3}$$

where

F_{AV} is the weighted mean FWHM (in units of keV);

N is the number of calibration points used;

F_i is the FWHM (in channels) of the i^{th} calibration peak;

σ_{F_i} is the standard deviation of F_i; and

$$C_i = w\sqrt{\frac{B_i}{w}} \tag{3.4}$$

Where w is the window width in channels and C_i is the "gain" term from the energy calibration equation and height of the spectrum for calculating the peak efficiency and resolution (Genie 2000, 2006) at a given energy was defined as

$$\varepsilon(E) = \frac{S}{T_1 y A K_w U_f} \tag{3.5}$$

where

$\varepsilon(E)$, is the efficiency at energy E;

S, is the net peak area of the calibration peak;

T_1, is the live time of the measurement;

A, is the source activity at the source reference time (certificate time);

U_f, is a factor to convert the activity A from other activity units into units of Bq and

K_w, is the decay correction factor, to correct the decay of the activity A to the activity at the time of the start of acquisition (Genie 2000, 2006); that is

$$K_w = e^{\left(-\frac{\ln(2) t_w}{T_{1/2}}\right)} \tag{3.6}$$

Where t_w, is decay time of the calibration source (the elapsed time between the start of the acquisition and the time at which the calibration source activity was reported), and

$T_{1/2}$, is half-life of the calibration nuclide.

The results of the total counts, absolute efficiency, peak efficiency and peak resolution (FWHM) are tabulated in Table 3.1.

3.6 Data analysis and discussion

The spectrum relating to the variation in the experimental and analytical alpha counts/sec. with energy for each of the detectors is displayed in Fig. 3.4 to Fig. 3.13. Each of the figures shows two plots, namely that of the experimental plot and that a plot after baseline subtraction. The spectra of the Optical Grade CVD diamonds Fig. 3.6 to Fig. 3.9 are observed to be broad; each without a well defined peak value, while each of the spectra of the Detector Grades has a better and more pronounced peak value around that of the alpha peak energy 5.48 MeV. Of note is the observation that the background corrected values with improved peak resolution has slightly shifted from the alpha centroid for all the detectors.

The measured average leakage current of 5.2 pA for Single Crystal (SC); 21.5 pA for DG; and 54.2 pA for OG could be part of the reason for the observed higher noise (fluctuation) in the optical and detector grade polycrystalline. The fact that less of the noise was measured in the Single Crystal may be the reason for it better peak resolution and hence that of the wafer (DG3).

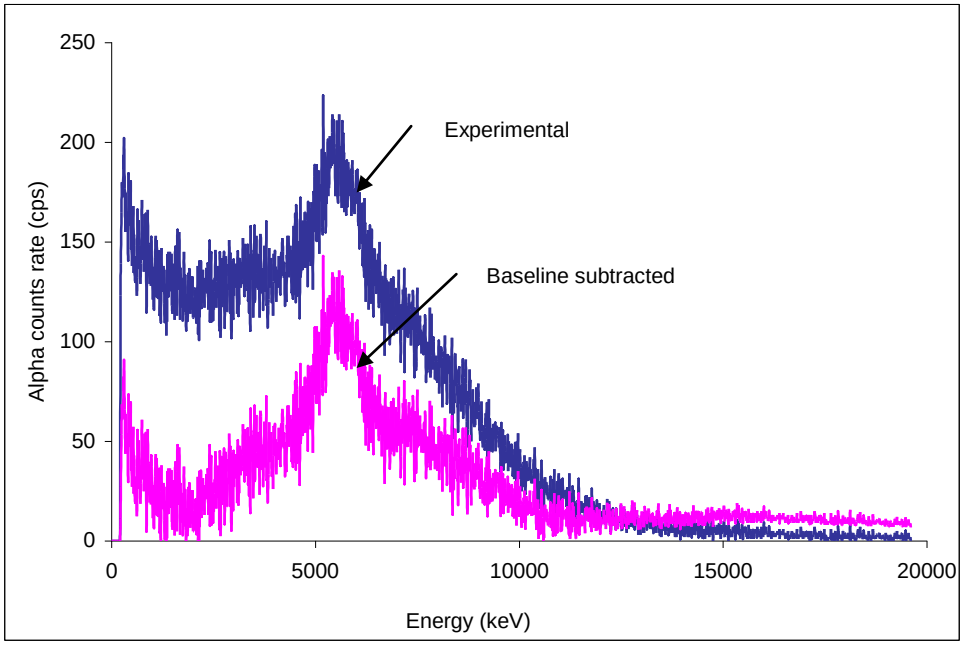


Figure 3.5: Variation of alpha count rate with energy for an Optical Grade CVD diamond (OG1)

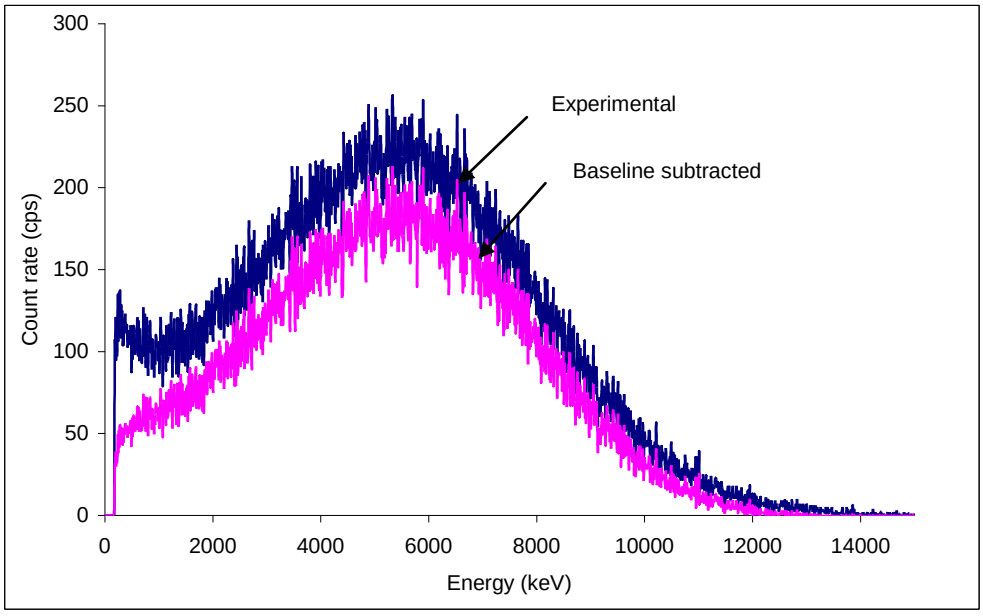


Figure 3.6: Variation of alpha count rate with energy for an Optical Grade CVD diamond (OG2)

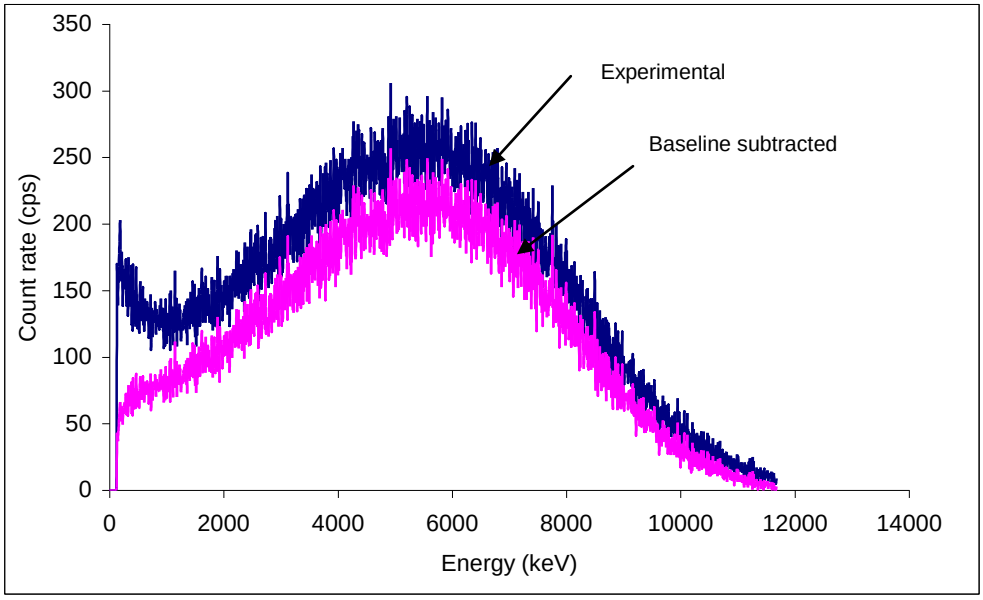


Figure 3.7: Variation of alpha count rate with energy for an Optical Grade CVD diamond (OG3)

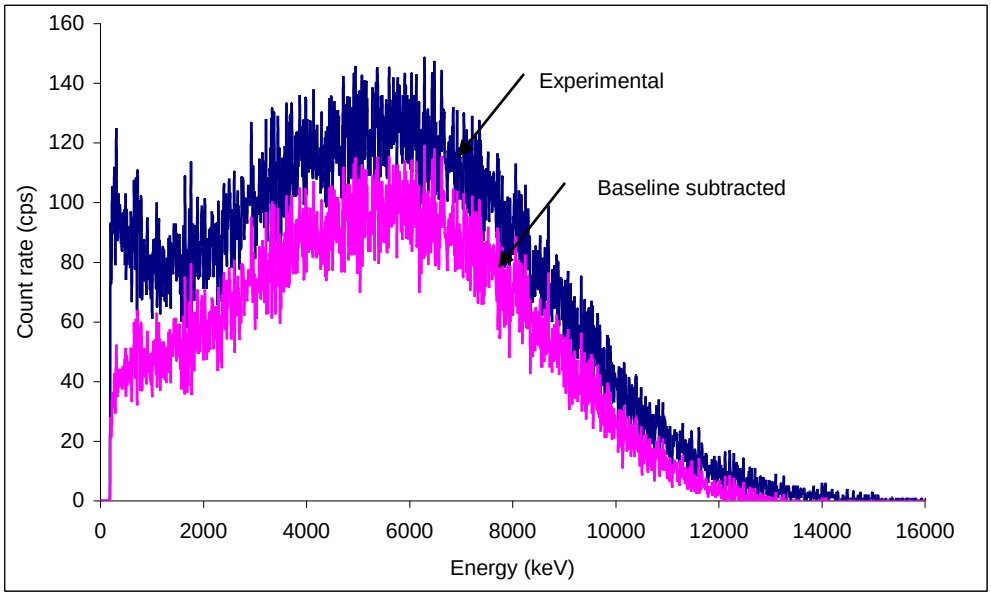


Figure 3.8: Variation of alpha count rate with energy for an Optical Grade CVD diamond (OG4)

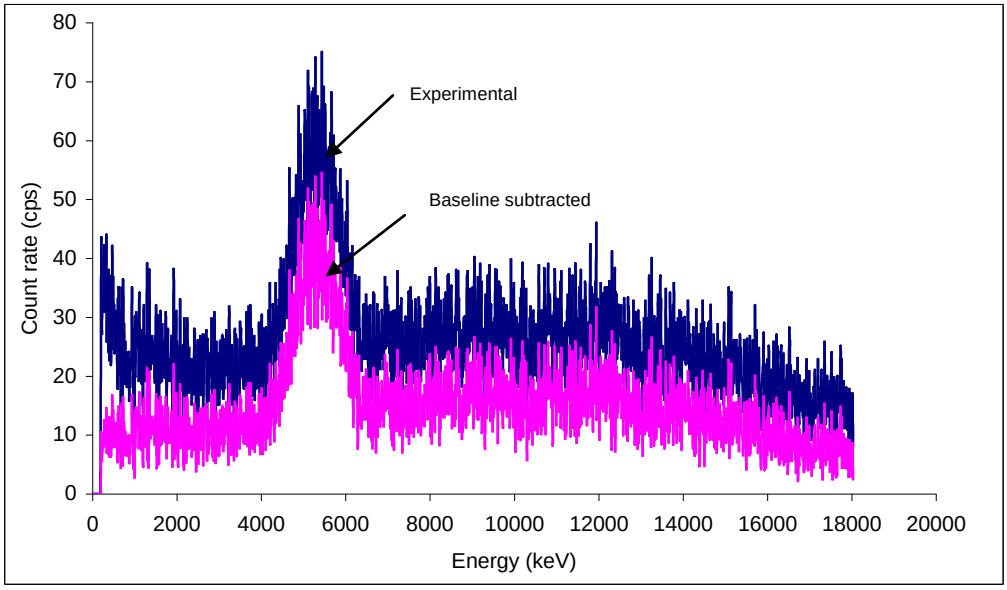


Figure 3.9: Variation of alpha count rate with energy for a Detector Grade CVD diamond (DG1)

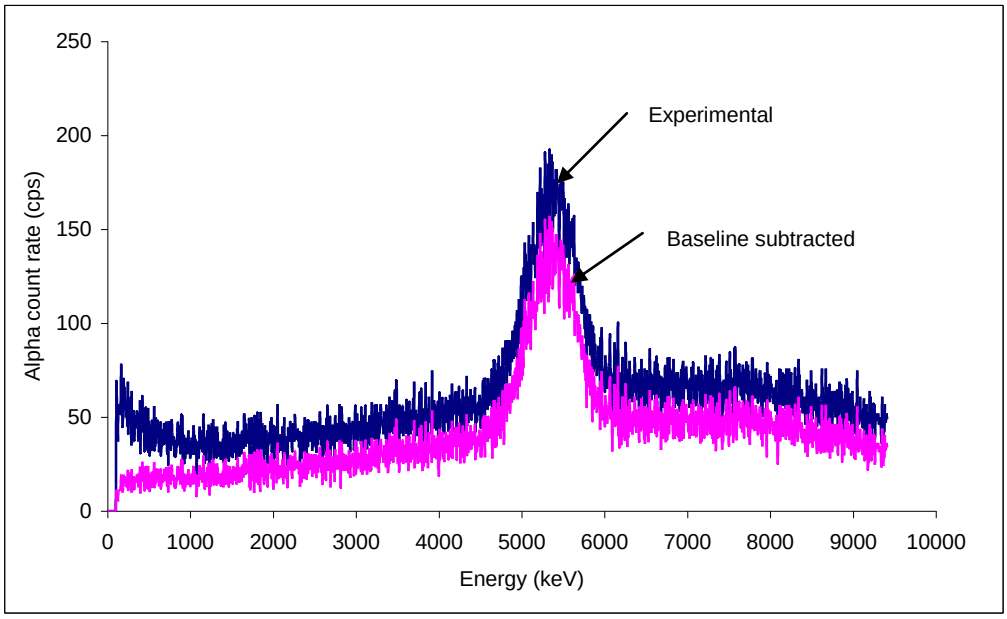


Figure 3.10: Variation of alpha count rate with energy for a Detector Grade CVD diamond (DG2)

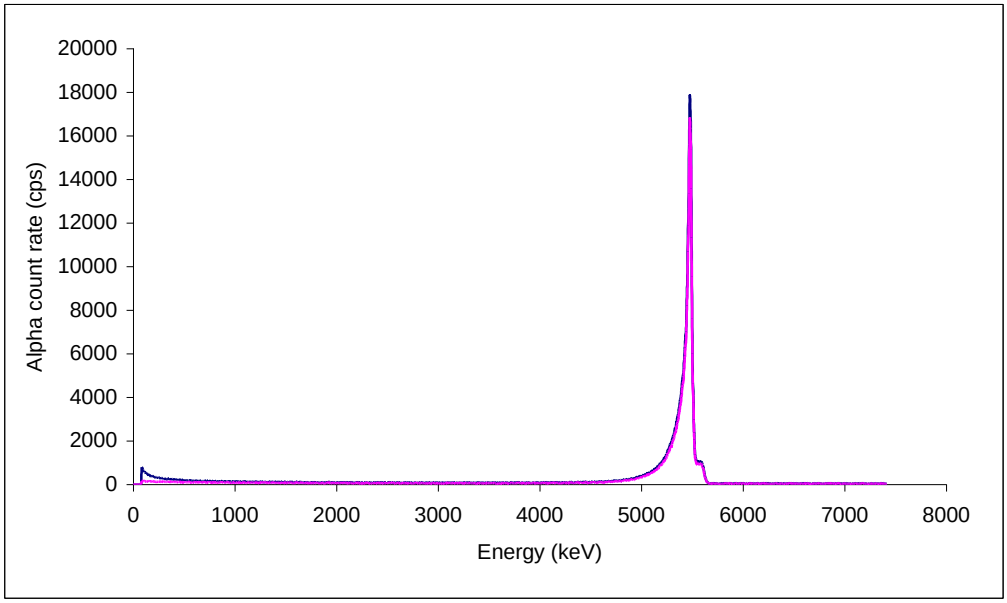


Figure 3.11: Variation of alpha count rate with energy for a Detector Grade CVD diamond (GG3)

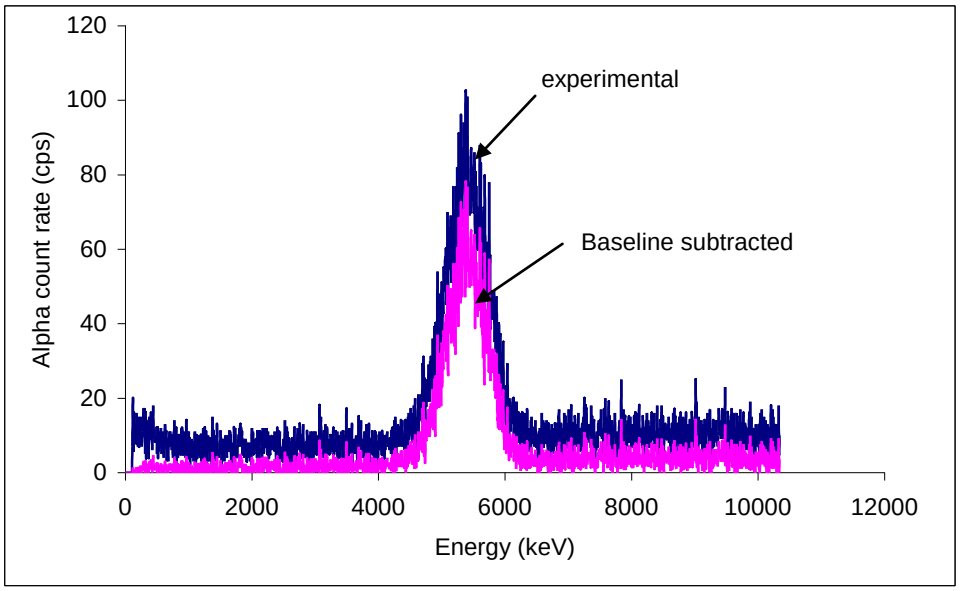


Figure 3.12: Variation of alpha count rate with energy for a Detector Grade CVD diamond (DG4)

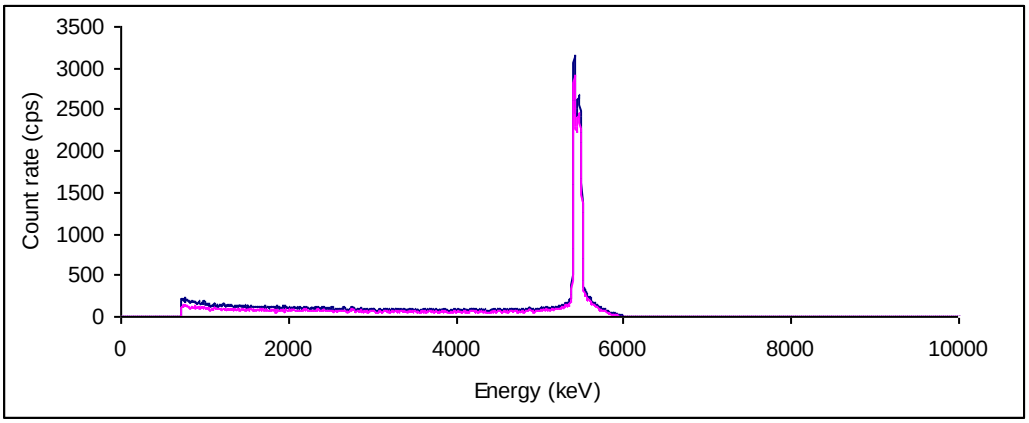


Figure 3.13: Variation of alpha counts with energy for a Single Crystal CVD diamond

Table 3.1 shows both the experimental and the analytical data analyzed using the software package (ORIGIN 6.1) before and after spectrum data correction. In the first two columns the experimental spectrum count rate is observed to be closely related and consistent with the analytical spectrum data but with slight differences. For the Optical Grade wafer the average absolute peak efficiency value is 94 % as compared to the experimental average value of 100 % reported in Chapter 2. The Detector Grade analytical data has an average absolute peak efficiency value of about 79 % and a 71 % value for the Single Crystal; both values being slightly higher than the average experimental values of 66 % and 52 % for the Detector Grade and Single Crystal wafers respectively. A possible explanation could be attributed to the software package Origin having lost track of data points during plotting due to the speed of analysis. Nevertheless it is believed that the method enables a better comparison of the wafers' performances as alpha detectors. The Table, in addition provides the experimentally obtained values for spectrum peak resolutions and peak efficiencies obtained from the analytical data of spectrum height, area and FWHM acquired using the software package Origin. The Detector Grade and Single Crystal wafers indicate peak-efficiency performance values of

about 80 % which in comparison with the Optical Grade wafer value of about 60 %; both results are consistent and same as that observed experimentally. The higher spectrum FWHM/peak resolution values for the Optical Grade CVD diamonds are found to be consistent with the results of the detectors' performances. For the Detector Grade wafers a spectrum resolution 19 % for DG1 (poorest peak) and 1.2 % for DG3 (best peak), with similar performance in the Single Crystal (SC) are observed. In comparison Kozlov et al., (1975) reported peak resolution value 1.1 % to 3 %. The analytical result of the Optical Grade wafers gave peak resolution values of between 109 % (for OG2) to 137 % (for OG1) as the experimental results while the Detector Grade diamond was between 1.2 % (for DG3) to 12.5 % (for DG2). In comparison the peak resolution for the Single Crystal is about 1.6 %.

Table 3.1: Spectral Analysis of accumulated alpha spectra from the three grades of CVD diamonds (The energy of the impinging alpha particles being 5.48MeV)

	Alpha counts (cps)		**%Absolute Efficiency**		**Peak Resolution**	**% peak Efficiency**
Detector Type	**EXPT**	**ANALT**	**EXPT**	**ANALT**	**EXPT**	**EXPT**
DG1	32969	35245	68	73	0.185±0.001	80
DG2	31327	39150	65	81	0.125±0.0023	80
DG3	29834	40623	62	84	0.012±0.0018	82
DG4	32732	37225	68	77	0.124±0.0030	80
OG1	50314	45355	104	94	1.365±0.0089	60
OG2	49010	46531	101	96	1.092±0.004	60
OG3	49397	46288	103	96	1.289±0.0048	60
OG4	39046	43787	81	91	1.325±0.0046	60
SC	25401	34172	52	71	0.016±0.0056	80

Note: (i) ANALT refers to value from the analytical experiment (ii) EXPT refers to experimental value (iii) FWHM refers to the full width at half maximum values

3.7 Conclusions

It can be concluded that the use of the adopted background subtraction methodology on each of the measured alpha spectrum had not affected the peak resolution and peak efficiency values. Noticeable improvements in the absolute efficiency were however obtained. In particular analytical calculations a more pronounced effect on the broader spectra of the Optical Grade detectors as compared to that on narrower and more resolved spectra such as those obtained from the Detector Grades and Single Crystals. Although the improvement is observed (to be greater) for the Optical Grade detectors, the spectrum peak resolution remained higher than the 0.70 value reported elsewhere (Berdermann et al, 2004 and Pomorski et al., 2005), confirming that OG wafers remains a poor choice material for use in spectrometry. The spectrum peak resolutions of the DG wafers (0.012±0.0018 to 0.185±0.001) lie within the 0.01 to 0.03 range which are in line with values reported by Wang et al. (2005); confirming the possible choice of such material for alpha spectrometry. It can be concluded that the comparative analysis adopted has provided a more accurate picture of the actual performance characteristics of the different diamond grades when used for alpha sensing. For the polycrystalline wafer the observed differences in the experimental and analytical methods could be attributed to the high leakage current, giving rise to statistical fluctuation and noise.

Generally the CVD diamond wafers were observed on exposure to alpha particles with 5.48 MeV energy, to have low leakage current (between 5.2 pA and 54.2 pA) and about 80 % full energy peak efficiency for the Detector Grade and 60 % for the Optical Grade wafers.

3.8 References

Adam et al., (RD42 Collaboration) 2003. *Nucl. Instrum. Methods Phys. Res.* **A447** 244

Akulinichev SV, LebedevSG and Vyalov GN 2003. *Moscow Meson Factory, Atomic Energy* **94** 49

Angelone M, Pillon M, Marinelli M, Milani E, Paoletti A, Tucciarone A, Pucella G and Verona-Ranati G 2004. *Radiat. Prot. Dosim*. **110(1-4)** 233

Bacci T, Borchi E and Bruzzi M 1998. *Nucl. Phys. B (Pro. Suppl.)* **61B** 303

Bauer C, Baumann I, Colledani C, e., 1996. *Nocl. Instr. And Methods in phys. Res.* **A383** 64

Berdermann E, Ackermann D, Ciobanu M, Hartmann W, Heßberger F, hildenbrand K, Hofmann S, Kiš M, Martemiyanov A, Mortz P, Pomorski M, Rebisz R, Voss B, Caragheorgheopol AG, Morse J, Salomé M,Sulignano B and Zhilin A 2004. *Supported by the EU Integrated Infrastructure Initiative Hadrons Physics, Project R113-CT-506078*

Berdermann E, Ciobanu1 M, Connell SH, da Costa AMOD, Tromson D, Brambilla A, Foulon F, Mer C, Guizard B, Barrett R, and Bergonzo P 2001. *Diamond and Related Materials* **9** 1850

Fallon PJ 1989. *Masters thesis. University of the Witwatersrand, Johannesburg, South Africa*

Genie ^{TM} 2000 3.1 2006. Customization Manual Canberra. http://www.Canberra.com

Grobbelaar JG 1988. *SA Patent Application, 88/7975*

Knoll GF 2000. *Radiation Detection and Measurement (third ed), Wiley, New York* 116.

Kozlov SF, Konorova EA, Kuznetsov YA, 1977. *IEEE Trans. Nucl. Sci*. **NS24** 235

Kozlov SF, Stuck EA, Hage-Ali M and Siffert P 1975. *IEEE Trans. Nucl. Sci.* **NS22** 160

Manfredotti C 2005. *Diamond and related materials Elsevier* **14** 531

Marinelli M, Milani E, Paoletti A, Tucciarone A, Verona- Rinati G, Angelone M, and Pillon M 2001. *Phys. Rev*. **B64** 19

Pomorski M, Berdermann E, Caragheopol A, Ciobanu M, KišM, Martemiyanov A, Nebel C and Moritz P 2006. *Physica Status Solidi* (**a) 203 (12)** 3152

Pomorski M, Berdermann E, Ciabanu M, Martemyianov A,Maritz P, Rebisz M, and Marczewska B 2005. *Phys. Stat. Sol.* **A202(11)** 2199

Sorenson AJ 1938. *"Physics in nuclear medicine" edition Grune and Stratton Inc. New York 10003*

Steier C, Robin D, Nadolski L, Decking W, Wu Y, and Laskar L 2002. *Physical Review* **E65** 056506

Toshisuke K, Kinya H, Hisashi K, Kunishino M, Shoji O, Takeshi T, Yukio U, Kaori Y and Kenji Y 2006. *IEEE Transactions on Nuclear Science* **53(2)** 630

Wang LJ, Lou YY, Su QF, Shi WM and Xia YB 2005. *Opt. Exp*. **13** 8612

Chapter 4

METHODOLOGY USED FOR THE CORRECTION OF BREMSSTRAHLUNG X-RAY SPECTRA OBTAINED FROM A Ge(Li) DETECTOR AND A COMPARISON WITH SPECTRA GENERATED FROM THE USE OF THE MONTE CARLO CODE PENELOPE.

4.1 Introduction

In the previous Chapters (2 and 3) the surface effects of the diamond detectors were assayed with α-particles and the detectors' performances related to the characteristics of various grades of CVD diamond. The need for a bulk interaction analysis of the CVD diamond wafers when exposed to X-ray radiation in order to provide an exposé of the parameters that affects their overall performances is the ab-initio motivation for the work described in the next few Chapters. An understanding of the types of radiation interactions likely to be encountered requires a thorough and quantitative knowledge of the activities of the sources, the type, and in the case of poly-energetic radiations, the energy range of the spectrum of all the sources likely to be used for the analysis (Seelentag et al., 1979). From the analysis in Chapter 2, it has been established that a spectrum resolution is an indication of the quality of the detector material. The contributions of the fluctuations and pile-up in the signal set important limits on the detector's performance (Chapter 3). Thus the main aim of this Chapter is to analyze the energy spectrum of the photons emitted by the mammography X-ray unit with a view to highlighting and removing all sources of fluctuation and/or noise created by the detection system used (i.e. to provide a spectrum independent of the detection system used). A germanium detector with known properties and characteristics to such radiation interactions was used as a standard to provide actual information pertaining to the total intensity/energy output from the X-ray unit. The detection of photon interactions with germanium results in the loss of some photons, but with the use of the calculated detector efficiency, these losses are corrected for, using the method described by researchers such as Epp and Weiss (1966); Fewell et al. (1977); Israel et al. (1971), Matsumoto et al.

(2000) and Seelentag et al. (1979), to strip photons. The adopted method of stripping used in this work is different from the stripping method used in Chapter 3. A Monte Carlo (PENELOPE) code simulating the experimental model (Blough et al., 1998, Boone et al., 1997, Cranley et al., 1997 and Tucker et al., 1991) was used to both compare and confirm the experimental results that had been corrected for the presence of unwanted artifacts.

4.2 Brief literature review

Hollander discussed the germanium detector's basic operating characteristics and applications in 1966. His focus was on the interaction of radiation with the detector crystal which included the calibration of the detector (Fewell et al., 1977). The detector's response functions such as the efficiency, linearity and spectrum resolution (Fewell et al., 1977) was evaluated for analysis of the detector's performance, to measure the photon spectrum from a mammography X-ray unit.

A recently mammography photon spectrum was measured by Matsumoto et al. (2000) where a cadmium zinc tellurium (CdZnTe) detector's performance was compared with that of germanium detector. In this section, a similar technique was applied to evaluate the photon spectrum acquired from the mammography X-ray Unit to analyze the performance characteristics of a germanium detector. Radiation interaction with the germanium detector releases charge carriers by ionization (Hecht et al., 1932; Gerrish., 1995; Sciortino, 1999). Electrons are excited from the valence band into the conduction band and are free to move, as are the holes produced in the valence band (Knoll, 2001).

The high voltage across the germanium detector creates an electric field, which sweeps the electrons to the positive contact and the holes to the negative contact (Hecht et al., 1932; Gerrish, 1995; Sciortino, 1999). This produces a small electric pulse, which is amplified by the preamplifier and the amplifier; the pulses are recorded and counted (Fewell et al., 1977). The number of charge carriers is proportional to the energy deposited (Evans, 1982). The size of the pulse is therefore proportional to the energy deposited by the incident radiation (Evans, 1982).

When devices such as detectors are used to measure radiation, they must, as a good practice, be calibrated to ensure that the results obtained are the true reflection of the interaction occurring within the detector (Seelentag et al., 1979). Calibration is properly carried out using the known activities of the reference sources. The calculation of the activity for a reference source is performed using the normal decay equation (4.1) formulated by Rutherford and Soddy in 1902 (Evans, 1982), where A_0 is the original radioactivity, A is the activity at the time t and λ is the decay constant ($\frac{\ln 2}{T_{1/2}}$) and $T_{1/2}$ is the radioactive half-life.

$$A = A_o e^{-\lambda t} \qquad (4.1)$$

4.3 Calculation of the activity of the sources

For a thorough analysis of a detector performance a complete knowledge of the activities and strength of the sources used is mandatory. In addition it is necessary to clearly define the environmental conditions and source filters (source encapsulations) under which they

are used. For the present analysis three reference sources were used: 1.73 Bq high-purity carrier-free Co-57 produced at the Obnisky cyclotron accelerator on the metal matrix-rhodium (thickness = 5 μm, active area diameter = 5 mm); a rectangular gamma reference source of Am-241 with activity of 390.3 Bq, and a Ba-133 source with an activity of 436.2 kBq, and an active source dimension 1mm in diameter that is sandwiched between 0.5-mm polystyrene windows. To calibrate the detector for the spectral analysis, the activities at the time of analysis was corrected for using equation 4.1. From the yield of each isotope the activity at the time for the experiment was calculated. Summarized in Table 4.1, is the list of the sources and their activities, that were used for calibrating the Ge(Li) detector.

Table 4.1: The list of radioisotopes used, showing the characteristic energy peaks (keV), Ao, A, yield and the final activity (A_f) at the time of measurement.

Reference source	Half life	Energy (keV)	A_o (Bq)	A (Bq)	Yield	A_f (Bq)
Co-57	271.8d	6.32	1730000000	675369	0.55	371452.95
Am-241	432.7y	13.83	407400	390304	0.133	51910.43
Co-57	271.8d	14.35	1730000000	675369	0.0919	62066.41
Am-241	432.7y	17.78	407400	390304	0.189	73767.46
Am-241	432.7y	20.82	407400	390304	0.049	19124.90
Am-241	432.7y	26.42	407400	390304	0.025	9757.60
Ba-133	10.53y	30.82	436200	72590.91	0.972	70558.36
Ba-133	10.53y	34.93	436200	72590.91	0.2271	16485.40
Am-241	432.7y	59.52	407400	390304	0.357	139338.53
Ba-133	10.53y	81.02	436200	72590.91	0.338	24535.73

4.4 Experimental procedures

4.4.1 Calibration of detector

The liquid nitrogen cooled germanium detector, with a sensitive area of 200 mm^2, a diameter of 16 mm and 10 mm thickness, was exposed to the different source activities to

acquire a spectrum. The reference sources were placed 50 cm from the detector using an optical stand. The spectra of Am-241, Ba-133 and Co-57 were obtained using the setup shown in Fig. 4.1 for a preset time of 3600 seconds.

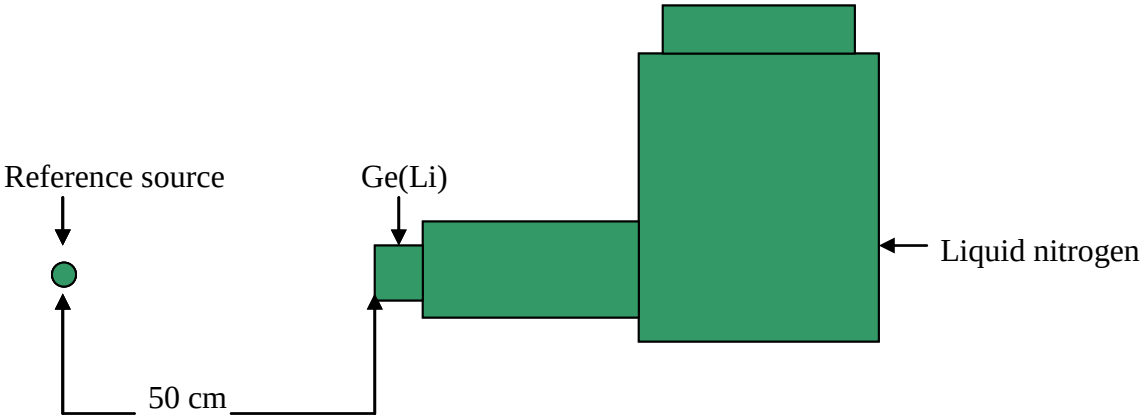


Figure 4.1: Schematic diagram depicting the relative positions of the germanium detector and the reference source

The acquired spectra of the different sources are in channel numbers, hence the need to calibrate the detector in order to convert their channel values to energy values. The spectral measurements were performed on the Ge(Li) detector systems GmbH (DSG) with serial number G-253 type PGP 200-10 at an operating bias of –2500 V. The detector was coupled to software packages SUPERVISOR; Windows 3.0 application, and (SUPER.EXE) which combine with MCARDWIN.EXE provided the automation of an MCA setup for data acquisition, spectral analysis, report generation and archival of spectra. The electronic circuit to which the germanium detector was connected for the pulse counting measurements is similar to the conventional circuits used for obtaining pulse height spectra, and is shown schematically in Fig. 4.2.

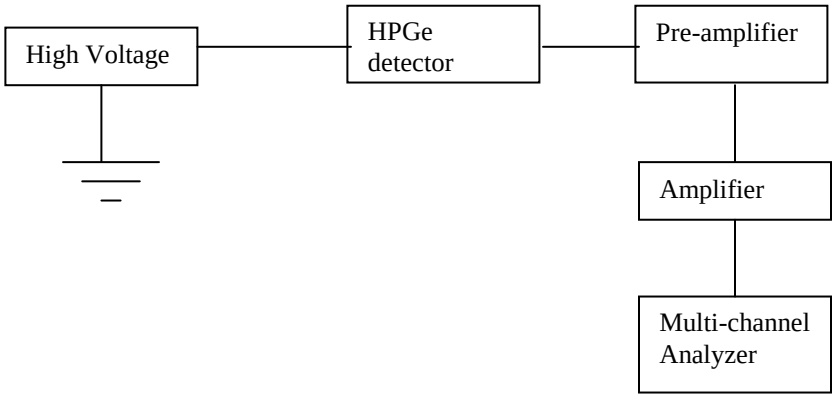


Figure 4.2: Schematic diagram of circuit used for pulse counting measurements

The circuit comprised a preamplifier, an amplifier and a pulse counter with a variable discriminator setting. The germanium detector was mounted directly onto the preamplifier's circuit board in order to reduce the capacitance between the leads from germanium detector to a minimum. The spectrum analysis was conducted using a microprocessor-based analyzer with 4096 channel background memory for buffer storage. For data acquisition the spectrum was set to operate in the multi-scaling mode.

From the spectrum such as the one depicted in Fig 4.3, the channel numbers corresponding to the reference source energies of 6.3 keV, 14.35 keV, 17.78 keV, 20.82 keV, 26.42 keV, 30.82 keV, 34.93 keV, 60 keV and 81 keV peak from the Am-241, Co-57 and Ba-133 were entered into the APTEC software for conversion to Microsoft Excel to calibrate the germanium detector. The plot (Fig. 4.4) of the source energy with the corresponding channel numbers provided the calibration line (fitted linearly) for the germanium detector.

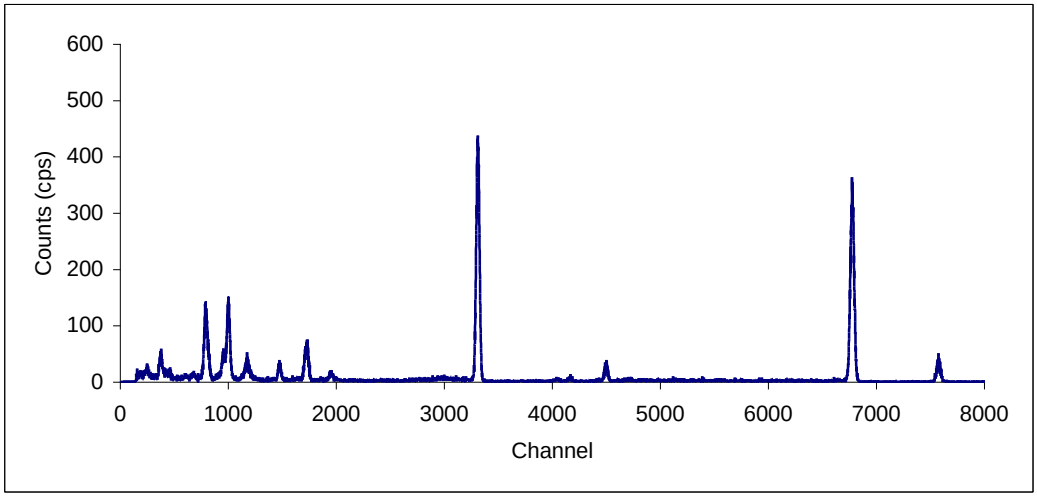


Figure 4.3: Uncalibrated Spectra obtained for the Am-241and Ba-133 sources with X-axis in channel numbers.

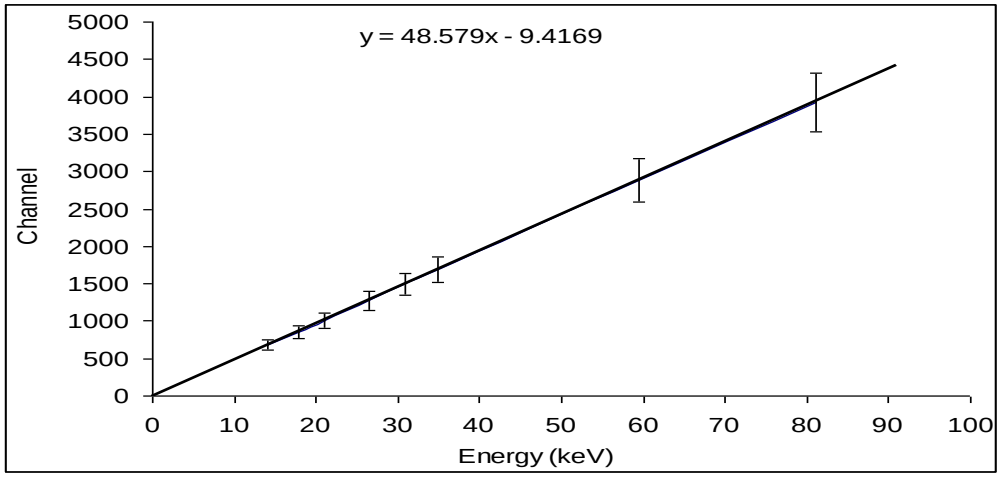


Figure 4.4: Calibrations curve of germanium (Ge(Li)) detector

4.4.2 Determination of efficiency of germanium detector

An APTEC software package was used to obtain the calibrated spectra of the Am-241, Ba-133 and Co-57 radioisotopes using the setup shown in Fig. 4.1. A dead time of less than 15 % was ensured by adjusting the detector to reference source distance. Depicted in Fig.4.5, from left to right, are the Compton scattered peaks as well as the energy peaks of Am-241. The integrated counts are tabulated in Table 4.2. The Table shows the

calculated, but uncorrected absolute efficiency of the germanium detector (column 5). The absolute efficiency (ε_{abs}) of the germanium detector, defined as the number of pulses recorded divided by the number of radiation quanta emitted by the source was applied.

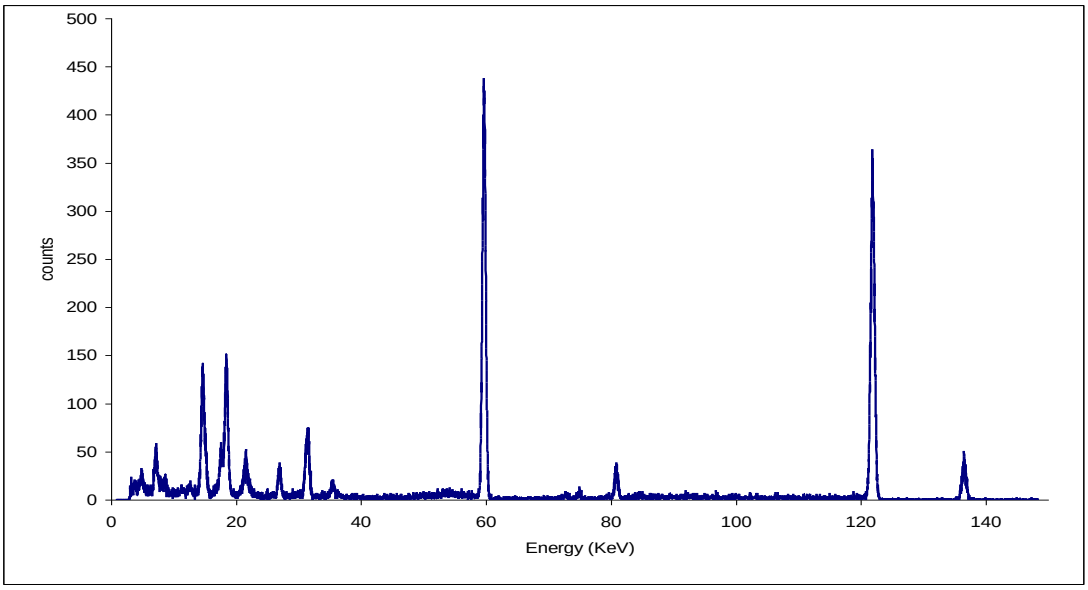


Figure 4.5: Corrected Am-241, Ba-133 and Co-57 spectra from the Ge(Li) detector showing different energy peak positions in keV.

Table 4.2: Table showing the reference source type, their energies (keV), the measured counts for 3600 seconds, counts per second and the uncorrected absolute efficiencies obtained by dividing the counts per second by the calculated activities (A_f) from Table 4.1.

Reference Source	Energy (keV)	Measured Counts in 3600 seconds	Count rate (cps)	Count rate divided by source activity i.e Uncorrected Absolute Efficiency
Co-57	6.32	1179	0.3275	8.81673E-07
Am-241	13.81	6331	1.7586	3.38778E-05
Co-57	14.35	5569	1.5469	2.4924E-05
Am-241	17.78	9719	2.6997	3.65977E-05
Am-241	20.82	2686	0.7461	3.90126E-05
Am-241	26.42	1450	0.4028	4.12784E-05
Ba-133	30.82	10440	2.9000	4.11007E-05
Ba-133	34.93	2533	0.7036	4.26809E-05
Am-241	59.52	21642	6.0117	4.31443E-05
Ba-133	81.02	3564	0.9900	4.03493E-05

A plot of the uncorrected detector efficiency with energy is depicted in Fig. 4.6. In comparison with published data the observed trend and efficiency values were found to be well below the known values, pointing therefore to the need for further correction to the efficiency values. Factors which have an influence on the efficiencies Co-57 at energies of 6.32 keV and 14.35 keV were identified as that of the 5-micron layer of rhodium filter, the intervening air between source and detector as well as that of an aluminium filter of unknown thickness.

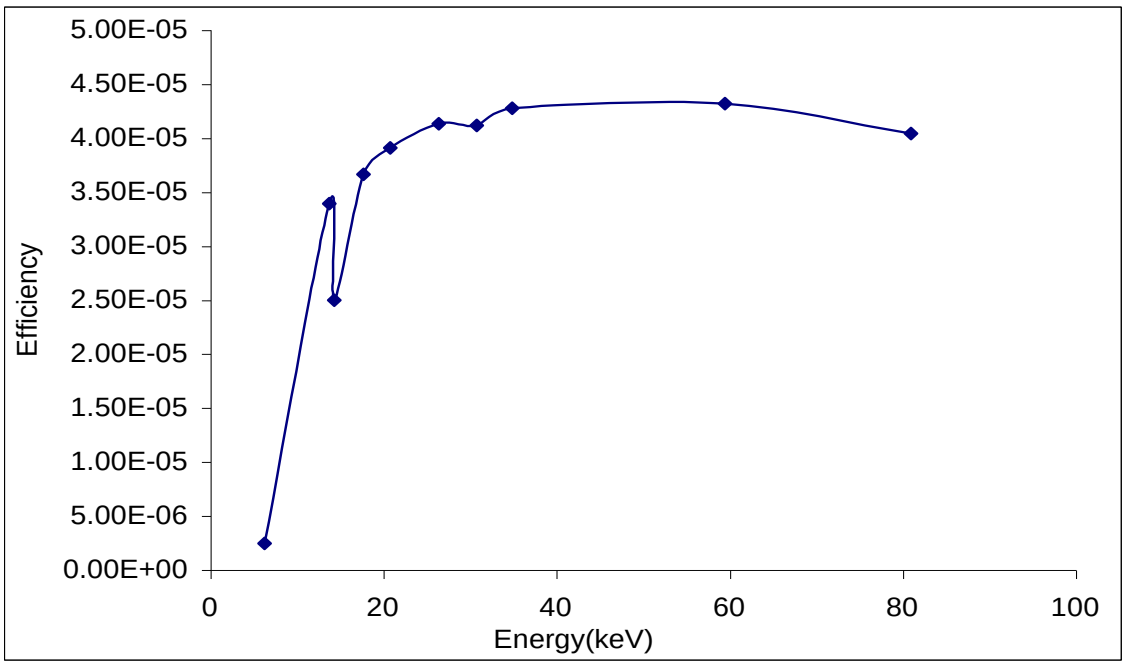


Figure 4.6: Plot of absolute efficiency vs energy for Co-57, with no correction for attenuation by rhodium and aluminum but with corrections for air, Be and Al.

4.5 Estimation of the aluminium filter thickness of the Co-57 reference source

To correct for the attenuations of the aluminium of unknown thickness, the activity of the Co-57 reference source at source to detector distance of 50 cm (Fig. 4.7) was measured over a period 3600 seconds. From the estimated source activity at the time of acquisition

of 57334 Bq, the detected count rate (1.7775 $Bq.s^{-1}$) was determined using the 6399 counts obtained over the 3600 seconds period. The activity after passing through rhodium and aluminium layers in front of the source was achieved by multiplying 57334 Bq by the 86 % value specified in the certificate by the manufacturer. This gave rise to the source activity value at the detector's surface of 49308 Bq. From the thickness for Rh of 10^{-4} cm, the thickness of the Al layer was then calculated. This was done using the emission efficiency value of 86 % for the Co-57 at 14.41 keV peak.

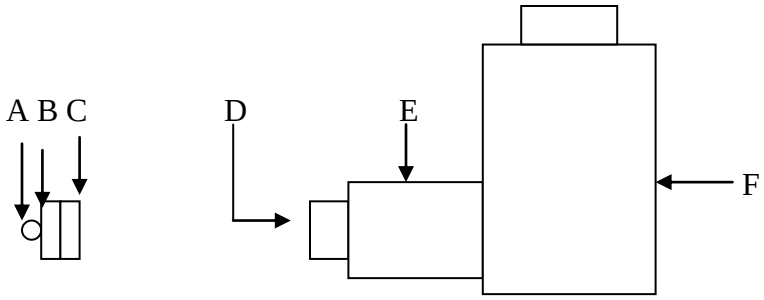


Figure.4.7: .Schematic diagram showing A as the reference source, with B = rhodium, C = aluminium, D = berylium window. E represent Ge-detector and F the liquid nitrogen container Activity of A = 57334Bq, After B and C attenuation, the, nominal activity is 49308 Bq. Using the efficiency value of 86% the counts on the detector per second obtained is 1.7775 cps

The product of mass absorption coefficient (μ), density (ρ) and the thickness (T) of air $(\mu\rho T)_{air}$ through which the radiation must penetrate before interacting with the detector was calculated to be 0.91. The uncorrected efficiency of $3.59x10^{-5}$ was obtained by dividing the detector count rate (1.775 cps) by the nominal activity (49308) in disintegrations per second. Attenuation by air was then corrected for by dividing the uncorrected efficiency by the $(\mu\rho T)_{air}$; from which a figure of 3.945×10^{-5} was obtained.

The count rate expected from the detector with air absorption and no absorption by Rh and Al of 2.26 Bq was obtained by multiplying the initial activity (57334 Bq) by the efficiency value 3.945 x 10^{-5}. Taking into account air absorption, attenuations of the 0.0005 cm Rh and Al (thickness to be calculated), and the attenuation expression

$$I = Io \exp(-(\mu\rho T)_{air} - (\mu\rho T)_{Rh} - (\mu\rho T)_{Al}) \quad (4.2)$$

Where:

I = 1.7775 Bq

I_o = 2.26 Bq

μ = mass absorption coefficient

ρ = density of the material

T = thickness of the material

Rh = Rhodium

$(\mu\rho T)_{Rh}$ =0.2325

$(\mu\rho)_{Al}$ = 23.004

was used to calculate the value of the 0.00146 cm thickness of aluminium (T_{AL}).The fact that the 13.8 keV peak energy of Am-241 superimposes on the peak energy of Co-57 at 14.35 keV, necessitated a correction of the efficiency of Am-241 as well. Using the 13.81 keV, Am-241 energy peak to calculate the efficiency instead of 86 % and the efficiency value of 3.388 x 10^{-5} from Table 4.2 column 5, the corrected efficiency for air absorption at 13.83 keV of 0.898 ($(\mu\rho T)_{air}$), gave rise to the resulting efficiency value of 3.775 x 10^{-5}. As the aluminium source was also encapsulated in 0.05 cm of polystyrene (C_8H_8) with density of 1.05 g/cm^3, the corrected efficiency for air and polystyrene was further calculated by dividing 3.775 x 10^{-5} by 0.959 ($(\mu\rho T)_{air} + (\mu\rho T)_{Rh}$). The final efficiency of

3.936×10^{-5} was obtained using Co-57 activity of 57334 Bq; the count rate of 2.26 $Bq.s^{-1}$ was obtained by multiplying the corrected efficiency for air and rhodium by 57334 Bq. To correct for the attenuation by aluminium, air, beryllium and rhodium for the Co-57 reference source at 6.32 keV and 14.35 keV, the correction factor was obtained as the product of the attenuations in columns 5 of Tables 4.3 and 4.4 and shown in row 6 of the tables.

Table 4.3: The list of absorbing materials with their thickness (T), density (ρ), mass absorption coefficient (μ/ρ), as well as the attenuation fraction (e (-(μ/ρ)ρT)) for 6.32 keV.

6.32 keV	**Thickness(cm)**	**ρ (g/cm^3)**	**(μ/ρ)=cm^2/g**	**Attenuation = exp(-(μ/ρ)ρT))**
Rh	5.00E-04	12.41	357	0.109133323
Al	1.46E-03	2.7	99.4	0.67581575
Air	50	0.00099964	22.3	0.328046931
Be	1.50E-03	1.848	2.01	0.996839256
Correction factor for Co-57 = 0.024060348				

Table 4.4: Tabulation of absorbing materials with their thickness (T), density (ρ), mass absorption coefficient (μ/ρ), as well as the attenuation fraction exp(-(μ/ρ) ρT)) for 14.35 keV.

14.35keV	**Thickness(cm)**	**ρ (g/cm^3)**	**(μ/ρ)=cm^2/g**	**Attenuation = exp(-(μ/ρ)ρT)**
Rh	0.0005	12.41	39.2	0.784086448
Al	0.00146	2.7	8.95	0.965334216
Air	50	0.00099964	1.91946	0.908520196
Be	0.0015	1.848	0.325	0.999488256
Correction factor for Co-57 = 0.687312003				

The efficiencies in Table 4.2 column 5 were then corrected for by dividing those values with the correction factors shown in Tables 4.3 and 4.4. The efficiencies of Am-241 and Ba-133 were also corrected for air attenuation, and all the calculated corrected efficiency

results tabulated in Table 4.5. The variation in the corrected efficiencies with energy is depicted in Fig. 4.8.

The effect of the two attenuation processes on the efficiencies at 6.32 keV and 14.35 keV are demonstrated in Fig. 4.8. The efficiency at the K-edge was determined by interpolation of the polynomial fit of the energy points ranging from 13.85 keV to 81.02 keV in Table 4.6. An equation from the fitted graph namely:

$$Y = -5E\text{-}09X^2 + 5E\text{-}07X + 3E\text{-}05 \quad (4.3)$$

where Y is the efficiency and X is the energy (keV). The graph was extrapolated backward until the efficiency at 11.2 keV was achieved. Using equation 4.3, the efficiency of the fitted curve at energy ranging from 11.2 to 81.02 keV was plotted as Fig. 4.9 and the required calculated efficiency was tabulated in Table 4.6

Table 4.5 Absolute efficiency (ε_{abs}) values obtained after correcting for the presence of rhodium, aluminium, air and beryllium window, between source and detector.

Energy (keV)	**Efficiency(ε_{abs})**
6.32	3.6557E-05
13.83	3.8037E-05
14.35	3.6263E-05
17.78	3.8831E-05
20.82	4.0637E-05
26.42	4.2354E-05
30.82	4.1954E-05
34.93	4.3449E-05
59.52	4.3704E-05
81.02	4.0825E-05

Table 4.6: Extrapolated values from 11.2 keV

Energy (keV)	Efficiency
11.2	3.50E-05
13.83	3.60E-05
14.35	3.61E-05
17.78	3.73E-05
20.82	3.82E-05
26.42	3.99E-05
30.82	4.07E-05
34.92	4.14E-05
59.52	4.20-05
81.02	3.77E-05

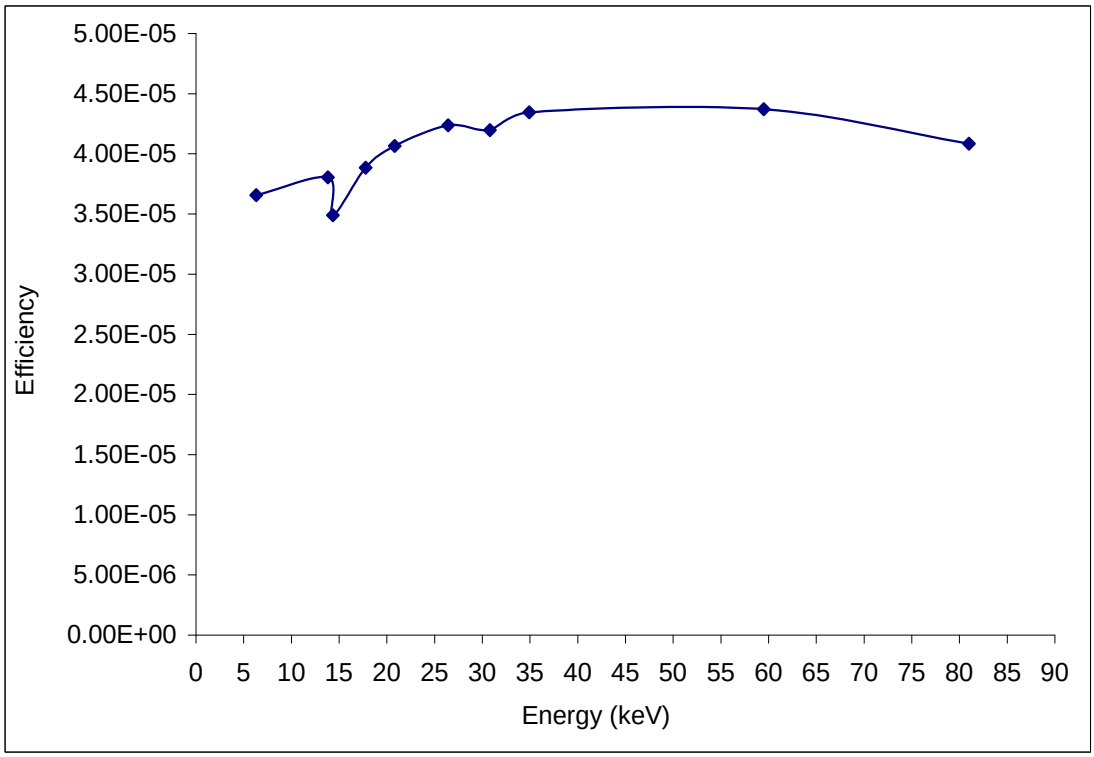


Figure 4.8: Graph of corrected absolute efficiency

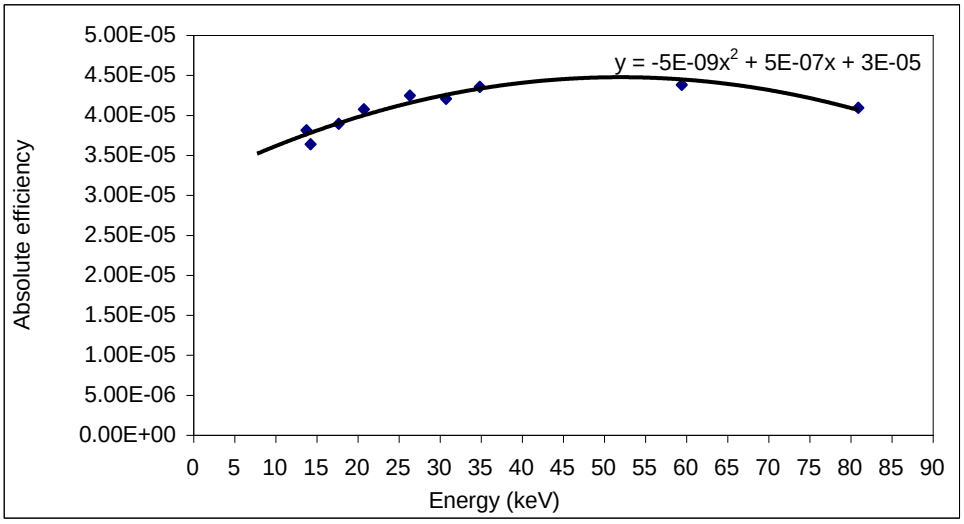


Figure 4.9: Absolute efficiency of germanium detector as a function of energy, with the fitted curve and equation.

The efficiency of the Ge detector is affected by attenuation above and below the K-edge at 11.1 keV. The probability of energy attenuation is shown in Fig. 4.10.

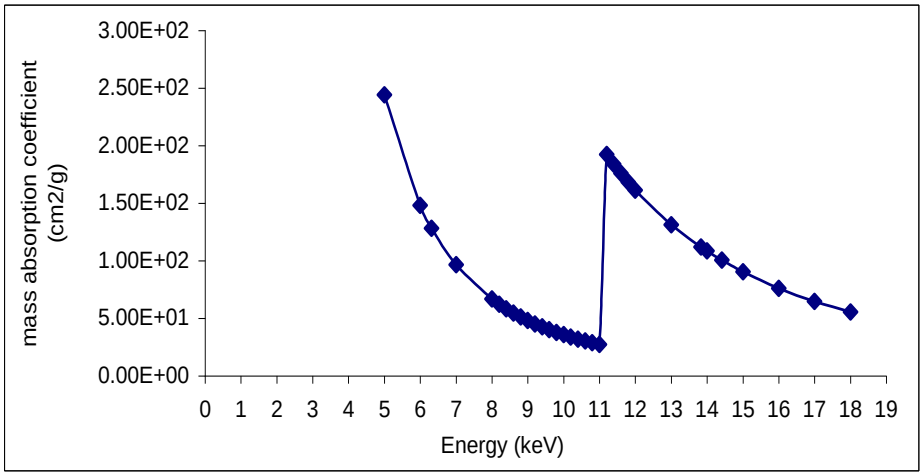


Figure4.10: Mass absorption coefficient (cm^2/g) as a function of energy above and below the K-edge of germanium.

The absolute efficiency at 11.2 keV is 3.50E-05 (Table 4.6). This process was demonstrated by the mass attenuation coefficient (μ/ρ) of germanium and can be expressed as the ratio between the mass attenuation coefficients (μ/ρ) at 11.1 keV (μ/ρ=28.1) and 11.2 keV (μ/ρ=194) calculated from the difference of μ/ρ at 11.2 keV and 11.1 keV divided by μ/ρ at 11.2 kV which resulted to 0.855154639. To correct for the efficiency at 11.1 keV, the absolute efficiency value (3.50E-05) was divided by the ratio (0.855154639) of the mass attenuation coefficients at 11.1 keV and 11.2 keV. This gave rise to an absolute efficiency value of 4.09E-05.

4.7 Determination of the solid angle

Given the radius of the detector (r = 8 mm) and the distance (d = 500 mm) from the reference source to the detector, the solid angle using equation

$$\text{Solid angle } (\Omega) = \frac{(\pi r^2)}{d^2} \tag{4.4}$$

the figure of 0.000804248 (rad), was calculated.

4.8 Intrinsic efficiency

The intrinsic efficiency is defined as the number of pulses recorded divided by the number of quanta incident on the detector and does not include the solid angle (Knoll, 2001). The intrinsic efficiency is related to the absolute efficiency by

$$\varepsilon_{\text{int}} = \varepsilon_{abs}((4\pi)/\Omega) \tag{4.5}$$

where Ω is the solid angle

The values of the intrinsic efficiency are tabulated in Table 4.7 together with the values of the absolute efficiency and relative efficiency. Using the absolute efficiency shown in

Table 4.7, the absolute efficiency curves Fig. 4.11 (comparable with the published Monte Carlo simulated efficiency by Chen et al., 1980) was generated implying the 11.1keV and 11.2 keV energy points that were corrected for by extrapolation.

Table 4.7: Corrected absolute efficiency, intrinsic efficiency and the relative efficiency.

Energy(keV)	**Absolute Efficiency (ε_{pmeas})**	**Intrinsic Efficiency**	**Relative efficiency**
6.32	3.66E-05	0.5712025	0.87
11.1	4.09E-05	0.6390072	0.97
11.2	3.50E-05	0.5464500	0.83
13.83	3.60E-05	0.5618547	0.86
14.35	3.61E-05	0.5647719	0.86
17.78	3.73E-05	0.5829531	0.89
20.82	3.82E-05	0.5975406	0.91
26.42	3.97E-05	0.6206234	0.94
30.82	4.07E-05	0.6353219	0.97
34.93	4.14E-05	0.6463203	0.98
59.52	4.20E-05	0.6569813	1.00
81.02	3.77E-05	0.5888875	0.90

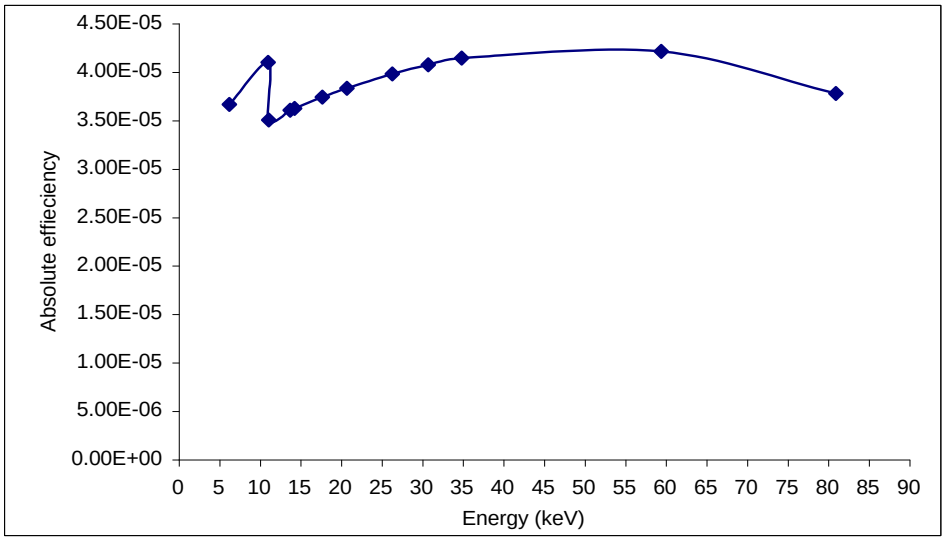


Figure 4.11: Absolute efficiency of germanium detector as a function of energy showing the expected K-edge at 11.1 keV

4.9 Germanium mean free path (λ)

During radiation interaction, radiation energy penetrates the absorbing material in relation to the interaction that takes place. The probability per unit length that a gamma photon is removed from the beam is expressed as

$$\mu = \tau(\text{photoelectric}) + \sigma(\text{Compton}) + \kappa\ (\text{pair}) \qquad (4.6)$$

The gamma ray photons interaction can also be characterized by their mean free path λ, defined as the average distance traveled in the absorber during an interaction (Knoll, 2001). By definitions:

$$\lambda = 1/\mu \qquad (4.7)$$

The mean free path values tabulated in Table 4.8 is a requirement for calculating the probability of K-escape fraction of the X-ray photon in each slice of the Ge(Li) detector during spectra analysis.

Table 4.8: Tabulated mass absorption coefficient (μ/ρ), linear attenuation coefficient (μ) and the path length (1/μ) values at the various energies of interest.

Energy (keV)	**μ/ρ (cm^2/g)**	**μ=(μ/ρ).ρ (cm)**	**λ=1/μ (cm^{-1})**
11.2	194	2407.54	0.0004
13.83	113	1402.33	0.0007
14.35	103	1278.23	0.0008
17.78	58.1	721.02	0.0014
20.82	37.8	469.10	0.0021
26.42	19.7	244.48	0.0041
30.82	12.8	158.85	0.0063
34.93	9.06	112.43	0.0089
59.52	2.07	25.69	0.0389
81.02	0.92	11.42	0.0876

To calculate the probability of the K X-ray escaping from each detector slice, the thickness of each slice (X) was determined taking into consideration the mean free path of the interaction created by each photon energy, where

$$X = 1/N \text{ cm} \quad (4.8)$$

Where N is the number of the slices and the n^{th} slice thickness must be smaller than the mean free path of the Ge K X-ray or the incident photon energy (Fewell et al., 1977). The numerator '1' represents the detector thickness in cm. The escape probability is a function of the distance r the K X-ray must travel before escaping the detector volume. The distance r can be calculated at an aperture θ from the relationship

$$r = Y/\cos\theta \quad (4.9)$$

and

$$Y = nX\text{-}X/2 \quad (4.10)$$

where Y is the distance to be traversed by photon in the material to the nth slice and X the slice thickness (equation 4.7).

Table 4.9: Tabulated values of slice thickness (X) the distance to the nth slice (Y) and the radius 'r'.

X (cm)	Y (cm)	Tan θ = X/Y	θ	Cosθ	r = Y/Cos θ (cm)
0.1	0.9004	0.111062	6.3374	0.9939	0.905926
0.2	0.9004	0.222124	12.5235	0.9762	0.922352
0.3	0.9004	0.333185	18.4273	0.9487	0.949088
0.4	0.9004	0.444247	23.953	0.9139	0.985228
0.5	0.9004	0.555309	29.0438	0.8742	1.02997
0.6	0.9004	0.666371	33.6783	0.8322	1.081951
0.7	0.9004	0.777432	37.8626	0.7895	1.140469
0.8	0.9005	0.8004	38.6738	0.7807	1.280261

The probability of a K X-ray being the photon energy escaping the detector with an angle θ is calculated in Table 4.10 ($P_{\Delta\theta}$) using equations 4.8, 4.9, 4.10 and the value of r in Table 4.9 in equation 4.11

$$P = \exp(-(\mu/\rho)\,\rho r) \text{ where } ([\mu]=cm^{-1}, [\rho]=g.cm^{3}, [r]=cm) \quad (4.11)$$

where P is the probability of K X-ray emitted into a given volume that will escape the detector and the values $(\mu/\rho)\rho$ was calculated in Table 4.8.

Table 4.10: Tabulation of the sum of the incident photons absorbed by the detector (ΣF_n), the change in the photon energy escaping the detector ($P_{\Delta\theta}$), and the escape fraction for each energy peak.

The ratio of k-shell interaction to the total no. of Photoelectric Interaction	The k-fluorescent Yield = the of the no. of k x-ray Emitted to the total no. of k-shell vacancies	$G_{\Delta\theta n}$	Energy (keV)	ΣF_n	$P_{\Delta\theta}$	Escape Fraction (f_{Ei}). $=\Sigma F_n$ x $P_{\Delta\theta}$ x $G_{\Delta\theta n}$ x0.88 x0.499
0.88	0.499	0.1066	11.2	1	0	0
,,	,,	,,	13.83	1	0	0
,,	,,	,,	14.35	1	0	0
,,	,,	,,	17.78	1	2.10E-284	9.84E-286
,,	,,	,,	20.82	1	2.74E-185	1.28E-186
,,	,,	,,	26.42	1	6.49E-97	3.04E-98
,,	,,	,,	30.82	0.9999999	3.18E-63	1.49E-64
,,	,,	,,	34.93	0.9999869	5.83E-45	2.73E-46
,,	,,	,,	59.52	0.9294372	7.81E-11	3.40E-12
,,	,,	,,	81.02	0.8107082	3.17E-05	1.20E-06

For each θ, in Table 4.9 a G_θ value defined as

$$G_\theta = (1-\cos\theta)/2 \quad (4.12)$$

were obtained. A $G_{\theta n}$ value was then calculated for each nth slice to obtain

$G\Delta_{\theta n} = G_{\theta n} - G_{\theta(n-1)}$ shown in Table 4.10 column 3.

From the parameters defined above a factor f_{Ei}, called the escape fraction defined as the probability of each incident photon with energy E_i appearing in the wrong energy interval by Fewell et al. (1977) as:

$$f_{Ei} = 0.439\sum_{n=1}^{N} F_n \sum_{\theta=0}^{\pi/2} (G_{\Delta\theta})(P_{\Delta\theta}) \qquad (4.13)$$

integer i= 1, 2, 3…n, f_{Ei} was calculated and tabulated in Table 4.10.

The total formulation used in stripping the X-ray spectra has to take into account not only the lower energy range below 12 keV known as the Compton continuum region as described by Fewell et al. (1977) and the higher energy range from 50 keV to 300 keV as described by Seelentag et al. (1979), but also the intermediate energies. At the lower energy range the effect of the losses due to Compton scattering could be accounted for using the procedure expounded by Fewell et al. (1977) and at the higher energies the probable loses due to photon escape, aperture and thickness of detector could be corrected for following methodology proposed by Seelentag et al. (1979).

4.10 Bremsstrahlung spectra from diagnostic X-rays.

In this section the X-ray spectra from both Mo and W anode tubes, obtained with voltages up to 95 kV, were analyzed. Corrections for detector window K-escape, Compton scattering and inefficient photon absorption were applied. In addition a combination of the two stripping techniques namely one proposed by Fewell et al. (1977) and the other by Seelentag et al. (1979) was adapted to include the intermediate energy range between 12 keV to 50 keV; the range not normally covered by the cited references.

A comparison of the corrected spectra from molybdenum and tungsten targets with computed spectra obtained using the PENELOPE Monte Carlo simulation code is presented.

4.10.1 Experimental setup

Spectral measurements were obtained using the liquid nitrogen cooled, high purity, intrinsic planar germanium detector, (as described in section 4.4). The detector was connected to a microprocessor-based system with 4096 channel background memory for buffer storage and set to the multi-scaling mode for data acquisition. For the X-ray beam analysis the germanium detector was placed 65 cm from a SENOGRAPHE 500T molybdenum mammography unit and a prototype tungsten target unit.

4.10.2 Detector calibration and data analysis

As described in section 4.4 the detector was calibrated in energy scales, and energy absolute efficiency ε_{pmeas} using the ^{241}Am, ^{57}Co and ^{133}Ba radioactive sources. The measured intensities were corrected for detector absolute efficiency using the two adopted techniques to formulate an integrated method that allow for the correction of entire photon spectra encountered in this work. The technique was also used to correct for Compton scatter, employing the method suggested by Seelentag et al. (1979) as calculated in Tables 4.10 for the spectra. The true photon intensity or the corrected counts, $I_o(E_i)$, with energy, E_i in keV, incident on the detector was calculated from the measured photon intensity (experimental counts), I_{Ei}, at each energy, E_i, where the

integer i= 1, 2, 3…m and m is the last energy point, using the adapted stripping equation, namely Eq. 4.14:

$$I_0(E_i)=\left[I_{E\,i} -\left(f_{E_i+E_K} I_{E_i+E_K} + \sum_{E_i=E_C}^{E_{\max}} C_h(E_i) I_t(E_i) \right) \right] / \left(1- f_{E_i}\right) \tag{4.14}$$

where $E_{\max}$ is the maximum energy of the spectrum and $E_c(E_i)$ is the Compton edge energy for each energy point,

$$E_C(E_i)=\frac{2E_i^{\,2}}{(2E_i+511)} \tag{4.15}$$

where $f_{E\,i}$ is a correcting factor used to formulate the spectrum stripping equation known as the K-escape fraction at the lower energy range (E_i<12 keV). $f_{Ei} I_o$ is the intensity of the lost photon or Compton scattered photons that escaped the detector volume, $f_{E_i+E_K}$ is the escape fraction at each energy E_i+E_K and $f_{E_i+E_K} I_{E_i+E_K}$ is the photon intensity (counts) corrected due to photon escape at each higher energy point E_i+E_K (E_K is the weighted average energy of the Ge fluorescent X-rays, it is 50 keV at higher energy range and is 10 keV at lower energies) (Israel et al., 1971). $I_t(E_i)$ is the true photon numbers (measured) for each energy.

Another factor related to the detector performance and called the calculated absolute efficiency is defined as $\varepsilon_{cal}=\left(1- f_{E_i}\right)$ which forms part of the formulation. When stripping continuous spectra, the effect of multiple scattering photons escaping the detector was considered using the factor $C_h(E_i)$ of each of the Compton continuum height. Each of the factors is generated by considering the difference between the

calculated absolute efficiency from the activity of the sources (ε_{cal}) from eqn. 4.13 and the measured absolute efficiency ε_{pmeas} (Table 4.7). The number of photons (counts) per keV in the Compton continuum per incident photon of each energy, E_i, is defined by Seelentag et al. (1979) as:

$$C_h(E_i) = \frac{\varepsilon_{cal} - \varepsilon_{pmeas}}{E_c(E_i)}(keV)^{-1} \quad (4.16)$$

Data on X-ray properties of germanium however, indicated that the fluorescent yield of K_β X-rays is negligible (Bertin, 1978), implying therefore that all the K-escape fluorescent is due to the K_α component; correction using only existing data for the K-escape fraction was therefore adopted.

4.10.3 Results and discussion

Figure 4.13 represent the normalized detector efficiency for the measured energy range 11.1–81 keV and table 4.7 for a germanium detector. Superimposed is the second-degree polynomial equation fitted to the data. The regression equation is

$$Y=-8\times10^{-5}x^2+8.4\times10^{-3}x+0.7838 \quad (4.17)$$

It correlates well with that published by Fewell and Shuping (1977). Corrected and uncorrected molybdenum and tungsten spectra are shown in Fig. 4.14 and Fig. 4.15 respectively. In both of these figures the characteristic K_α and K_β X-rays are well separated by applying the formulated equation to strip off the effects of the background. The characteristic X-rays spectra correlate well with the published results and with the simulated spectra obtained from the PENELOPE Monte Carlo code. The details of which are described in Chapter 6.

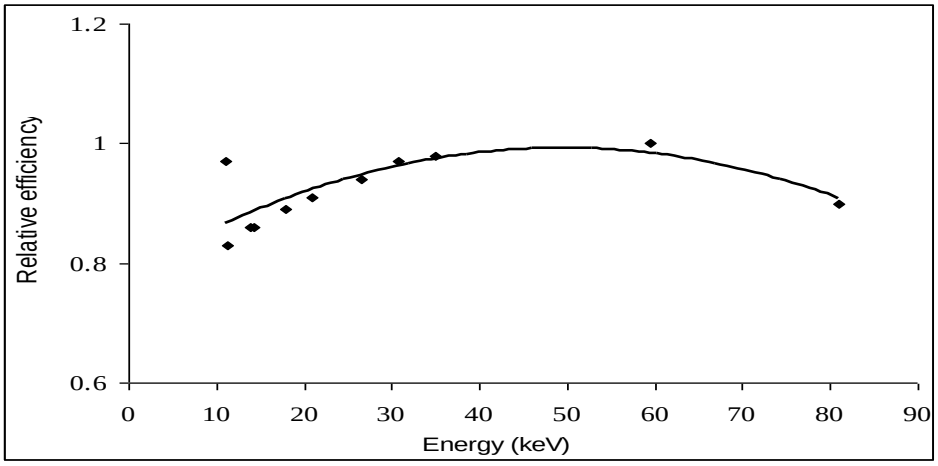


Fig.4.13. Relative efficiency of the Ge(Li) detector after correcting for attenuation by air, aluminium, beryllium window and rhodium matrix of Co-57 reference source (from Table 4.7).

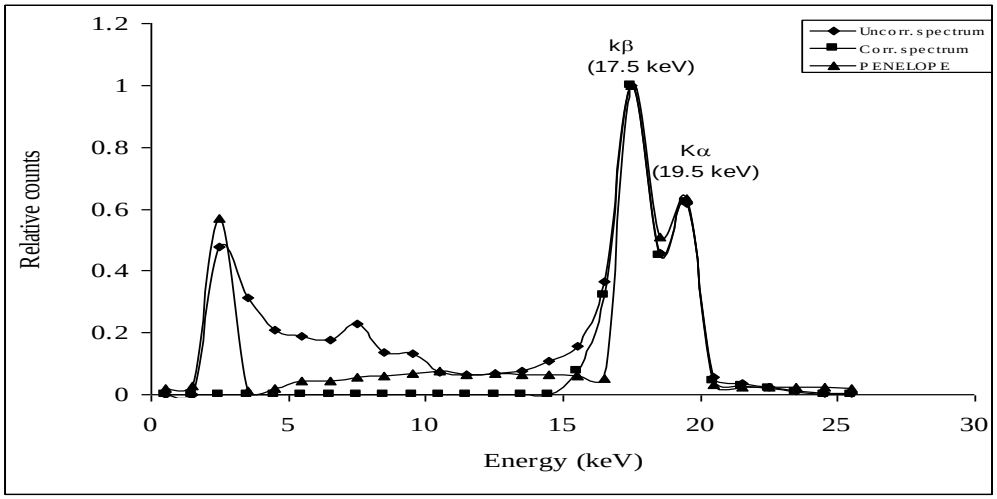


Figure.4.14. Corrected and uncorrected molybdenum spectra obtained from the measured data at 25 kVp setting and a Monte Carlo simulated molybdenum spectrum.

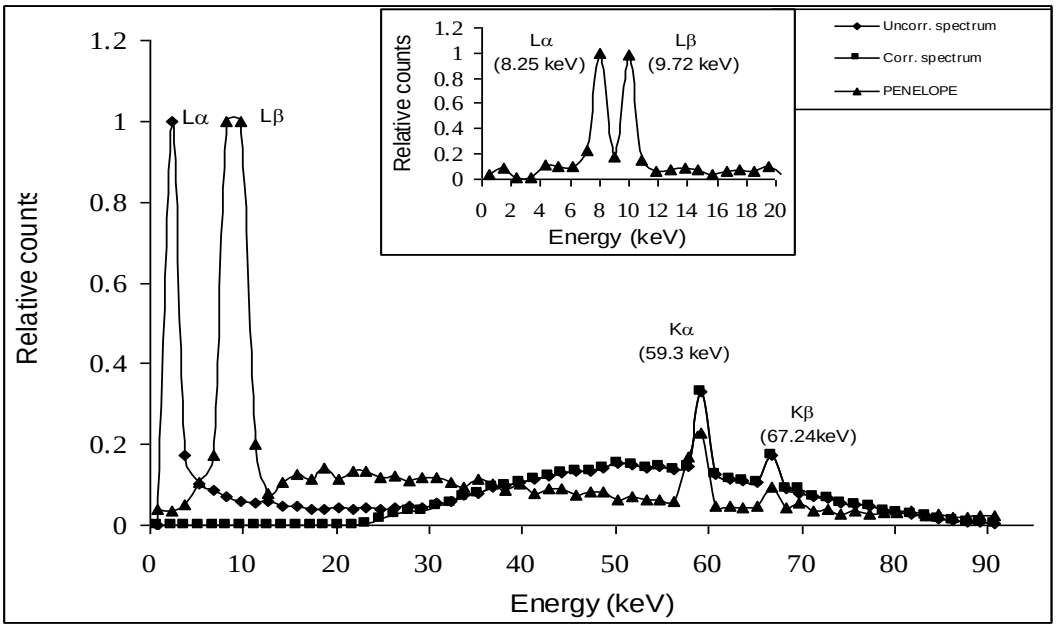


Fig.4.15. The corrected and uncorrected tungsten spectra obtained from measured data and a Monte Carlo simulated tungsten spectrum. Inset is the PENELOPE Monte Carlo computation to 20 keV.

4.11 Conclusion

The mammography spectra obtained using the Ge(Li) was analyzed. The inherent effects due to artifacts present in the Ge(Li) detector were corrected for. This Chapter has identified a method for obtaining an artifact free spectrum. To contrast the response of a pure diamond to that of the actual CVD diamond wafers, it is essential that the spectral range of the photon energy used in the Monte Carlo simulation program be an exact replica to that emitted by the X-ray Unit, but without any of the artifacts that are normally introduced by the measuring system used to obtain the energy output. The use of such a spectrum is described in Chapter 6 to highlight the possible role impurities/defects play in CVD diamond wafers when used in the detection of photons within the mammographic X-ray energy range.

4.12 References

Bertin, E., 1978. *Plenum Press, New York.*

Blough MM, Waggener RG, Payne WH and Terry JA 1998. *Med. Phys*. **25** 1605

Boone JM, Fewell TR and Jennings RJ 1997. *Med. Phys*. **24** 1863

Chen CS, Doi K, Vyborny C, Chan HP, and Holje G 1980. *Med. Phys.* **7(6)** 627

Cranley K, Gilmore B, Fogarty G and Desponds L 1997. *Catalogue of diagnostic X-ray spectra and other data IPEM Report 78 (York: IPEM)*

Epp ER and Weiss H 1966. *Phys. Med. Biol.* **11(2)** 225

Evans RD 1982. *The atomic nucleus. Robert E. Krieger Publishing Company Malabar, Florida*.

Fewell, T.L. and Shuping, R.E., 1977. *Med. Phys*. **4(3)** 187

Gerrish VM 1995. *Simiconductors Semimetals* **43** 493

Hecht K 1932. *Z. Phys.* (Berlin) 235

Hollander 1966. *Nucl. Instrum. and Methods***. 43**: 65

Israel HI, Lier DW and Storm E 1971. *Nucl. Instrum. and Methods* **91**141

Knoll GF 2001. *Radiation detection and measurement. Second edition. John wiley & Sons*

Matsumoto M, Yamamoto A, Honda I, Taniguchi A and Kanamori H 2000. *Med. Phys*. **27** 1490

Sciortino S 1999. *Riv. Nuovo Cimento* **22** 1

Seelentag, W.W. and Panzer, W. 1979. *Phys. Med. Biol*. **24(4)** 767

Tucker DM, Barnes GT and Wu X 1991. *Med. Phys*. **18** 402

Chapter 5

EVALUATION OF OBSERVED VARIATION IN CVD DIAMOND DETECTOR RESPONSE WITH CRYSTAL DEFECTS AT LOW ENERGY MAMMOGRAPHIC X-RAYS.

5.0 Abstract

The tissue equivalence of diamond allows for accurate radiation dose determination without large corrections for different attenuation values in biological tissue. The low Z value limits this advantage however, to the lower energy photons. Nine Chemical Vapour Deposition (CVD) diamonds have been analyzed for use as mammography X-ray dosimeters using the linearity, sensitivity and characteristics of the detectors to the photon interaction. The resistivity of each of the diamond grades is calculated from the I-V characteristics of the samples. The diamonds, categorized into four each of, so called, Detector and Optical grade, and a Single Crystal CVD were exposed at low X-ray peak voltage range (22 to 27 kVp) with trans-crystal polarizing fields of 0.4 $kV.cm^{-1}$, 0.6 $kV.cm^{-1}$ and 0.8 $kV.cm^{-1}$. The crystals were then assayed for further physical characteristics additional to earlier cataloging of their defects reported elsewhere in Chapter 2. The response of the CVD diamond wafer as an X-ray dosimeter within the selected energy range was evaluated with the aim of classifying the appropriate CVD type for use in the mammography X-ray energy region.

5.1 Introduction

The interest in bulk interaction analysis of the CVD diamond requires the use of the X-rays source for this work. In this Chapter, the interaction of the low energy X-rays spectra with defects in CVD diamond wafers (mentioned in Chapter 2) is discussed. The performance characteristics of the CVD diamond exposed to mammography X-rays within the spectral range analyzed in Chapter 5 was monitored at different potentials. The search for radiation detectors of robust material possessing also high thermal

conductivity, high breakdown voltage, high radiation hardness, large saturated carrier mobility and high band gap, makes diamond an excellent choice of material. The increase in the use of radiation as a clinical diagnostic tool in recent years coupled with the demands for improved measurements of the radiation beams to allow for greater control over treatment motivated this work. Presently, ionization chambers and silicon diodes are the most widespread dosimeters in this field. While the ionization chamber has low spatial resolution and sensitivity, the silicon diode suffers from radiation damage and hence decreases in performance with time and has a limited life, therefore. The advent of chemical vapour deposition (CVD) technique has overcome the known drawbacks of natural diamonds as a radiation probe, and has allowed for its application in X-ray and nuclear dosimetry to be exploited by many researchers (Marinelli et al., 1989; and Assiamah, 2004). Diamond has been used as a thermo-luminescence dosimeter (Nam et al. 1991; 1989), and as a radiosensitive resistor (Burgemeister, 1981; Keddy et al., 1987).

Diamond has a unique advantage of being a tissue equivalent material and non toxic, thus making it suitable for in-vivo usage. Diamond has also been used as a probe in electron radiation therapy (Van der Merwe, 1994); as a sensor for measuring low X-radiation (Grobbelaar et al., 1991) and for X-ray mammography dosimetry (Assiamah et al., 2004).

The production of the CVD synthetic diamonds with controlled amount of impurities, reproducible, and with improved carrier life-time, provides the impetus to characterize the properties needed to fabricate detectors with good performance characteristics.

The polycrystalline nature of a CVD diamond wafer contributes to many grain boundaries where concentrations of impurities and/or defects are found (Manfredotti et al., 1996). These impurities and/or defects determine the quality of the CVD diamond and particularly the electrical performance. The characteristics of each of the diamond types described determined in Chapter 2 are both highlighted and contrasted in this Chapter, in relation to their interaction with the photons when used as detectors.

5.2 Experimental Method

5.2.1 Experimental setting of sample holder

The different grades of CVD diamond of dimensions 5x5x0.5 mm biased at voltages of between 200 V to 400 V, were each placed in the sample holder (Fig.5.1) previously designed by Assiamah, (2004) for evaluation. Each CVD diamond wafer was exposed to X-rays from a Senographe 500t mammography unit at a distance of 50cm from the tube.



Figure 5.1: The sample holder with BNC connector. The slit opening provides for both positioning and 'edge-on' exposure.

5.2.2. The Wellhofer system setting

The Sample holder was attached to the Wellhofer system (Fig. 5.2) that provided the bias voltage to the diamond wafer. The responses of the CVD diamond wafers, were

monitored and recorded using a Wellhofer dosimetrie CU500E control computer 232C-A. For data acquisition a software package WP600 version 4.26C was used.



Figure 5.2: The Wellhofer CU 500E Control Unit

5.2.3 Senographe 500t mammography X-ray Unit setting

The senographe 500t mammography X-ray unit serves as a source of X-rays used to probe the diamond wafers (Fig. 5.3). Nominal tube voltage settings of 22 kVp, 23 kVp, 24 kVp, 25 kVp, 26 kVp and 27 kVp were used to expose both the CVD diamond wafers together with the reference Diados detector. Integrated responses (at 2s integration time) with applied electric field of 0.4 $kVcm^{-1}$, 0.6 $kVcm^{-1}$ and 0.8 $kVcm^{-1}$ were measured for each of the specimens.

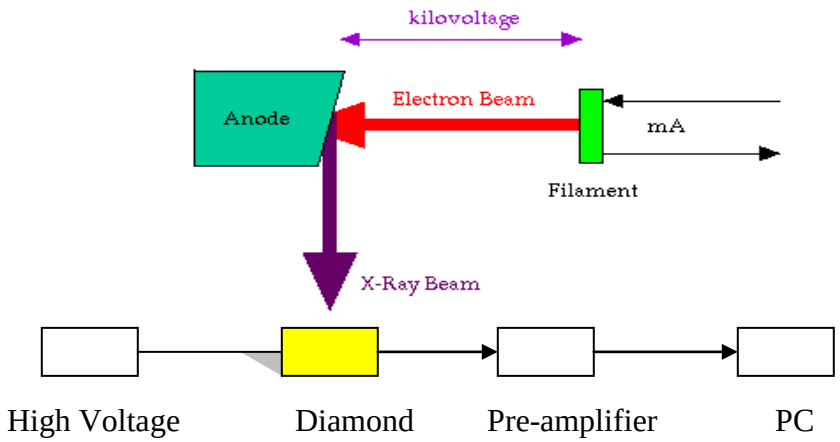


Figure 5.3: Schematic diagram of X-ray production and CVD diamond detector

5.2.4 The DIDOS E setting as a reference detector

To ensure consistency and repeatability a PTW diados 11003-1121 reference detector attached to the PTW UNIDOS E (Fig. 5.4) was placed next to the CVD diamond detector for all X-ray exposure measurements.



Figure 5.4: The PTW UNIDOS E for biasing the diados and displaying the results of the dose measured

The measurement of the I-V characteristics of the detector-probe assembly were made using a Keithley 237 unit for biasing and for measuring the output signal over the range 0-500 V for the polycrystalline diamonds and a range of 0-1000 V for the single crystal. The resistivity of each wafer was calculated from the measured values.

5.3 Results and Discussion

Table 5.1 is a presentation of the data for the current-voltage (I-V) characteristics for all the three diamond grade types as shown in Figure 5.5. The reciprocal of the gradients of the curves was used to calculate the resistivity values for each of the crystal types. Averaged resistivity values of 1.25×10^{14} Ωm for the Single Crystal, 2.5×10^{13} Ωm for the Detector Grade and 1.25×10^{13} Ωm for the Optical Grade were obtained.

The observed high resistivity of the crystals was part of the reason for the low X-ray response as reported in Tables 5.2a, 5.2b and 5.2c for the bias voltages at 200 V, 300 V and 400 V respectively. For each of the applied electrical fields the X-ray energy was also varied from 22 kVp to 27 kVp. The Detector Grade (DG) diamonds, on average, gave the higher response rates. In particular DG3 displayed, consistently, the highest response rate for all variations of peak voltage (kVp) settings at each of the applied electric fields when compared to both the Optical Grade CVD and Single Crystal CVD diamonds.

The Single Crystal was also observed to perform consistently better than all of the Optical Grade detectors and a particular Detector Grade (DG1) in terms of sensitivity.

Table 5.1: Current-Voltage characteristics for Single, DG and OG CVD diamond diagram

Voltage Setting (volts)	Current (amps)		
	SC	OG	DG
30	2.10E-13	6.50E-12	1.50E-12
50	8.00E-13	9.30E-12	9.00E-12
80	1.60E-12	1.65E-11	2.00E-12
120	3.00E-12	2.50E-11	1.80E-12
200	5.80E-12	4.80E-11	1.17E-11
300	9.10E-12	8.80E-11	3.68E-11
500	1.64E-11	1.86E-10	8.80E-11
800	2.50E-11		
1000	3.50E-11		

Table 5.2a: X-ray response rate at 200V bias for DG, OG and SC

Detector Type	Raman FWHM (cm^{-1})	TL (arbt. Unit)	ESR (ppm)	UV (cm^{-1})	X-ray response (cps) at 200V bias					
					22 kVp	23 kVp	24 kVp	25 kVp	26 kVp	27 kVp
DG1	2.64	1146.8	3.5	0.51	1.52	1.64	1.72	1.95	2.18	2.35
DG2	2.57	881.2	4	1.93	1.62	1.96	2.41	2.56	2.78	3.01
DG3	2.63	2023.7	5	1.03	1.72	2.46	3.07	3.46	4.08	4.56
DG4	2.55	813.8	5.3	1.9	1.65	2.28	2.53	2.64	2.76	3.03
OG1	2.59	154.5	42.9	3.86	1.29	1.57	1.76	1.95	2.1	2.2
OG2	2.78	83.2	71	3.52	1.22	1.54	1.88	2.15	2.24	2.4
OG3	2.76	140.5	53.6	3.48	1.2	1.55	1.96	2.12	2.4	2.21
OG4	2.81	93.2	62.5	3.59	1.25	1.54	1.64	1.91	2.05	2.19
SC	2.32	25	1	0.88	1.35	1.74	1.86	2.1	2.21	2.42

Table 5.2b: X-ray response rate at 300V bias for DG, OG and SC

Detector Type	Raman FWHM (cm^{-1})	TL (arbt. Unit)	ESR (ppm)	UV (cm^{-1})	X-ray response (cps) at 300V bias					
					22 kVp	23 kVp	24 kVp	25 kVp	26 kVp	27 kVp
DG1	2.64	1146.8	3.5	0.51	1.92	2.38	3.15	3.87	4.5	4.98
DG2	2.57	881.2	4	1.93	2.18	2.73	3.67	4.14	4.6	5.25
DG3	2.63	2023.7	5	1.03	2.45	2.92	3.71	5.26	5.62	6.15
DG4	2.55	813.8	5.3	1.9	2.26	2.76	3.41	3.76	4.55	4.86
OG1	2.59	154.5	42.9	3.86	1.78	2.22	3.05	3.14	3.22	3.34
OG2	2.78	83.2	71	3.52	1.89	2.26	2.8	3.54	3.72	3.81
OG3	2.76	140.5	53.6	3.48	1.91	2.38	2.9	3.1	3.4	3.5
OG4	2.81	93.2	62.5	3.59	1.82	2.31	2.84	3.15	3.37	3.52
SC	2.32	25	1	0.88	2.13	2.59	2.75	2.95	3.34	3.56

Table 5.2c: X-ray response rate at 400V bias for DG, OG and SC

Detector Type	Raman FWHM (cm^{-1})	TL (arbt. Unit)	ESR (ppm)	UV (cm^{-1})	X-ray response (cps) at 400V bias					
					22 kVp	23 kVp	24 kVp	25 kVp	26 kVp	27 kVp
DG1	2.64	1146.8	3.5	0.51	2.31	2.87	3.26	3.94	4.64	5.07
DG2	2.57	881.2	4	1.93	2.42	2.98	3.72	4.08	4.78	5.41
DG3	2.63	2023.7	5	1.03	3.31	3.74	4.48	5.38	5.71	6.29
DG4	2.55	813.8	5.3	1.9	2.59	2.92	3.54	3.88	5.61	5.46
OG1	2.59	154.5	42.9	3.86	2.19	2.27	3.09	3.32	3.5	3.72
OG2	2.78	83.2	71	3.52	2.26	2.42	3.17	3.58	3.84	3.92
OG3	2.76	140.5	53.6	3.48	2.14	2.34	3.2	3.29	3.57	3.66
OG4	2.81	93.2	62.5	3.59	2.16	2.61	2.88	3.23	3.41	3.62
SC	2.32	25	1	0.88	3.68	4.29	4.79	5.07	5.34	5.9

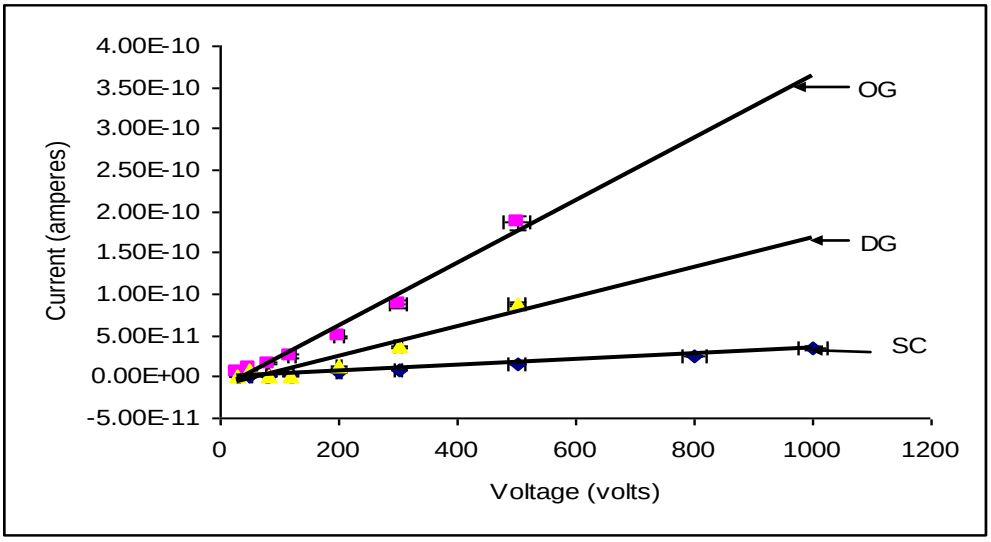


Figure 5.5: Variation of current with bias voltage for detector grade, optical grace SC CVD diamonds

Figure 5.6 shows the response at electrical field of 0.4 $kV.cm^{-1}$ of all the wafers falling under the DG classification, to be linear with changing peak voltage setting. Figure 5.7 is a plot of the response rate with change in kVp settings for the Optical Grade CVD diamond at an applied electric field of 0.6 $kV.cm^{-1}$. Here the response is observed to saturate at higher kVp settings of between 25 kVp to 27 kVp.

Figure 5.8 is the graph of the response rate of the Single Crystal specimen with 27 kVp change for an applied electrical field of 0.8 $kV.cm^{-1}$. Unlike the Optical Grade CVD diamond the gradient is positive and linear. Figure 5.9a is a plot of the change in response rates with applied voltage for a Detector Grade (DG3). The gradients are linear and positive and are observed to vary from 0.47 at 200 V bias, 0.74 at 300 V bias and 0.60 at 400 V bias. The observed crossing of the plots at 27 k Vp for 300 V and 400 V bias settings, as depicted in Fig. 5.9a, can be attributed to the inherent safety features of mammography X-ray unit itself. It is designed to prevent over exposure by limiting the extent X-ray photons can be emitted. To substantiate this, the response of a less sensitive detector DG2, to kVp change was repeated for the same bias voltage range. The result of which is shown in Fig. 5.9b. Unlike Fig. 5.9a parallel plots with no crossing over is highlighted.

Depicted in figure 5.10 and figure 5.11 are the variations in responses from an Optical Grade and a Single Crystal CVD diamond respectively with kVp settings for 3 different bias voltage settings. The gradient for the Single Crystal was 0.19 at 200 V, 0.49 at 300 V and 0.44 at 400 V unlike the response of the Single Crystal, the gradient of the Optical Grade is again observed to be non linear and saturates at higher kVp values of 25 kVp to 27 kVp.

Although the linear gradient values for the Detector Grade and Single crystal is observed to show a decrease above 300 V bias this could be ascribed to recombination of the charges when highly sensitized or biased (Hecht et al., 1932; Gerrish 1995; Sciortino

1999) else it could be due to a reduction in the internal field due to polarization and the consequent capture release mechanism (Souw et al., 1997)

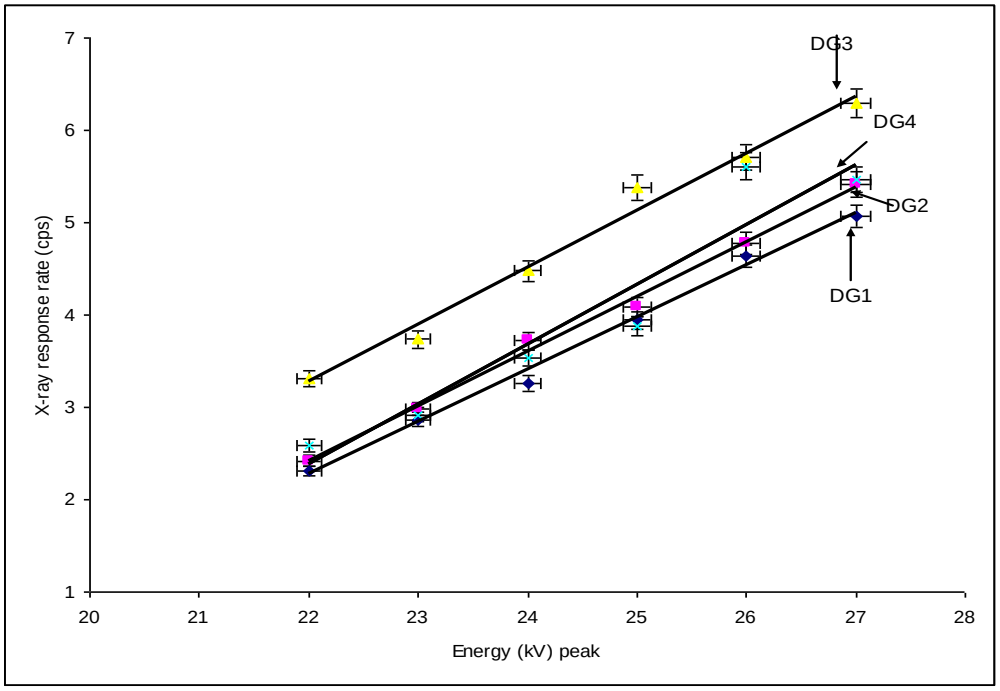


Figure 5.6: Variation of X-ray response rate with energy for Detector Grade CVD diamonds at 400 volts bias

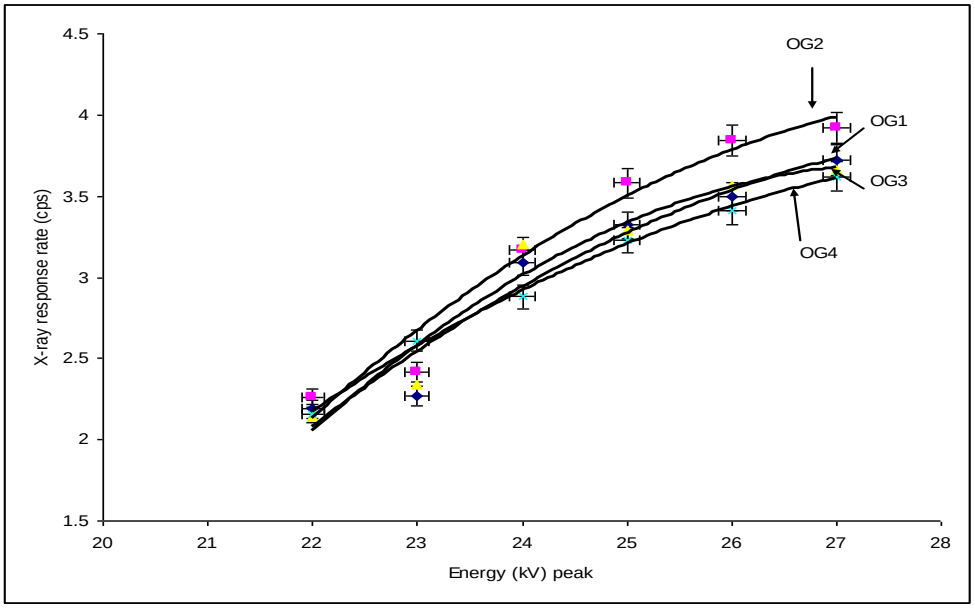


Figure 5.7: Variation of X-ray response rate with energy for Optical Grade CVD diamonds at 400 volts bias

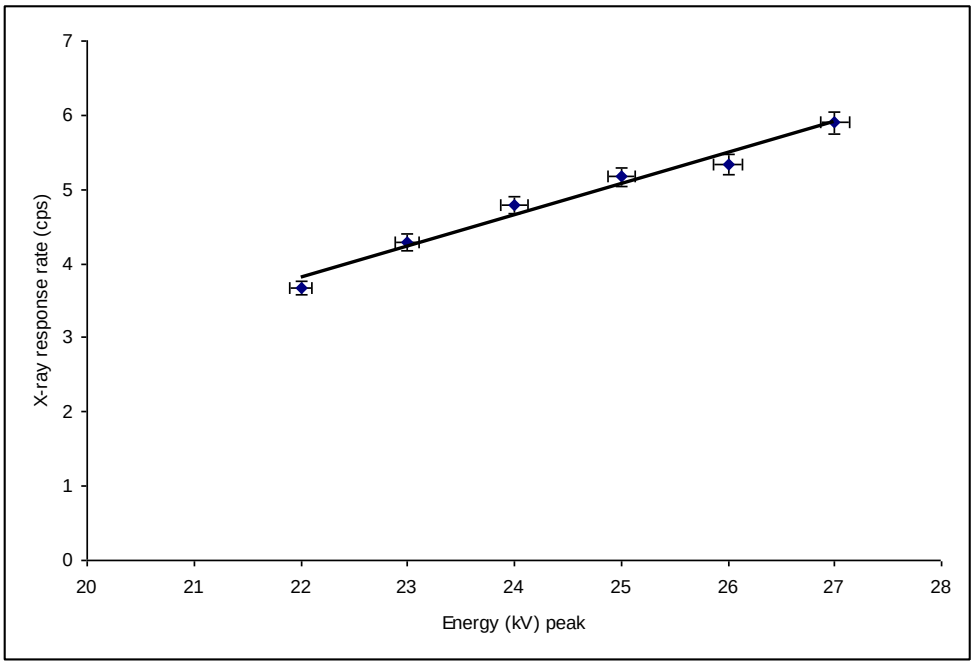


Figure 5.8: Variation of X-ray response rate with energy for Single Crystal CVD diamond at 400 bias voltages

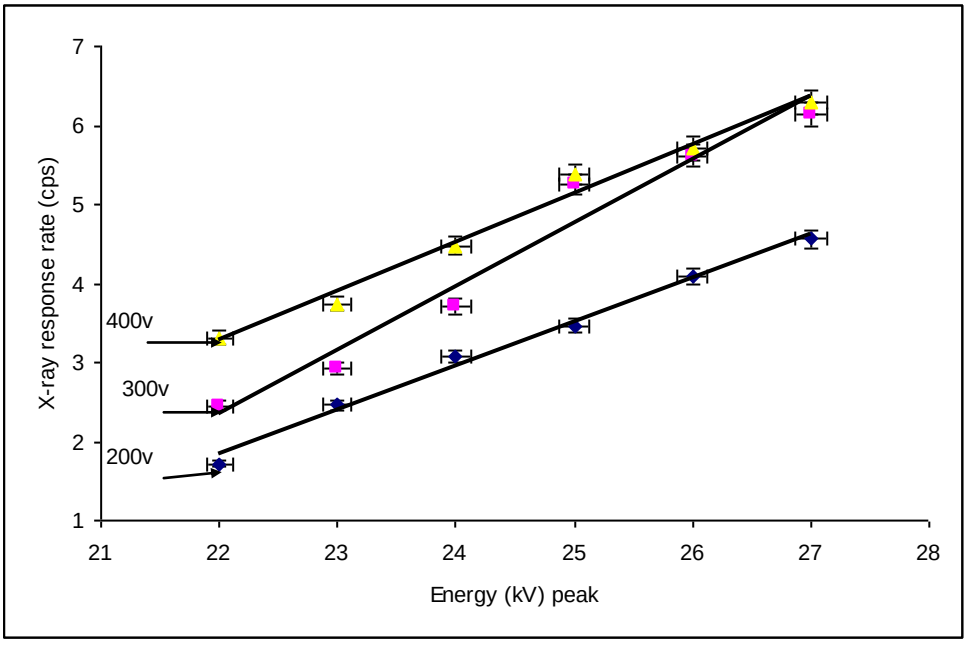


Figure 5.9a: Variation of X-ray response rate with energy for Detector Grade (DG3) CVD diamond at different bias voltages

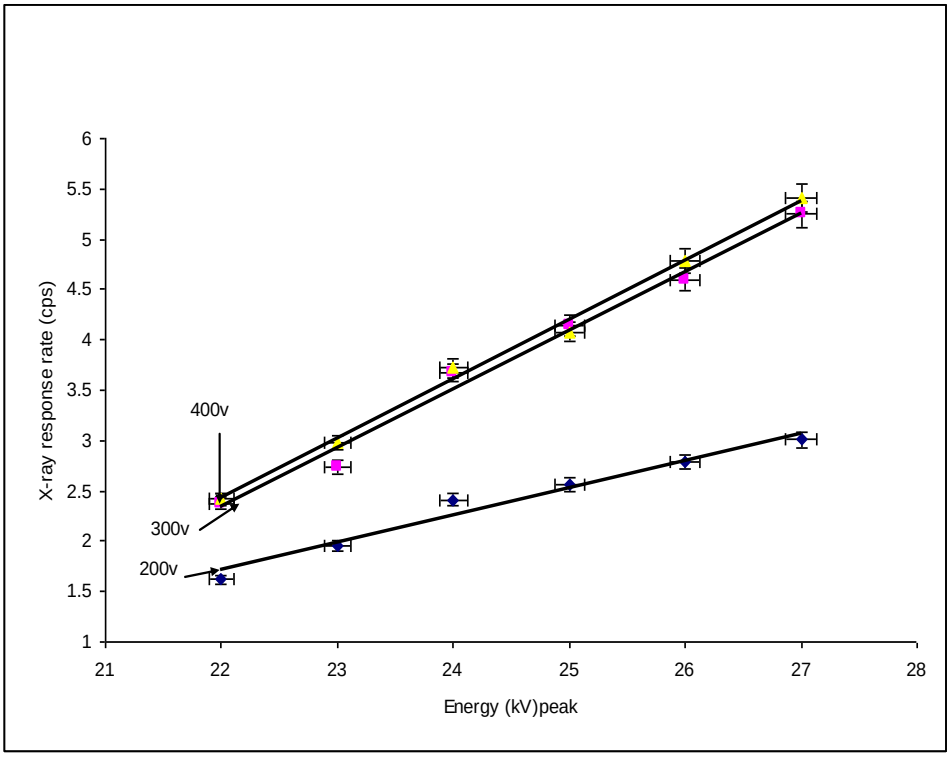


Figure 5.9b: Variation of X-ray response rate with energy for Detector Grade (DG2) CVD diamond at different bias voltages

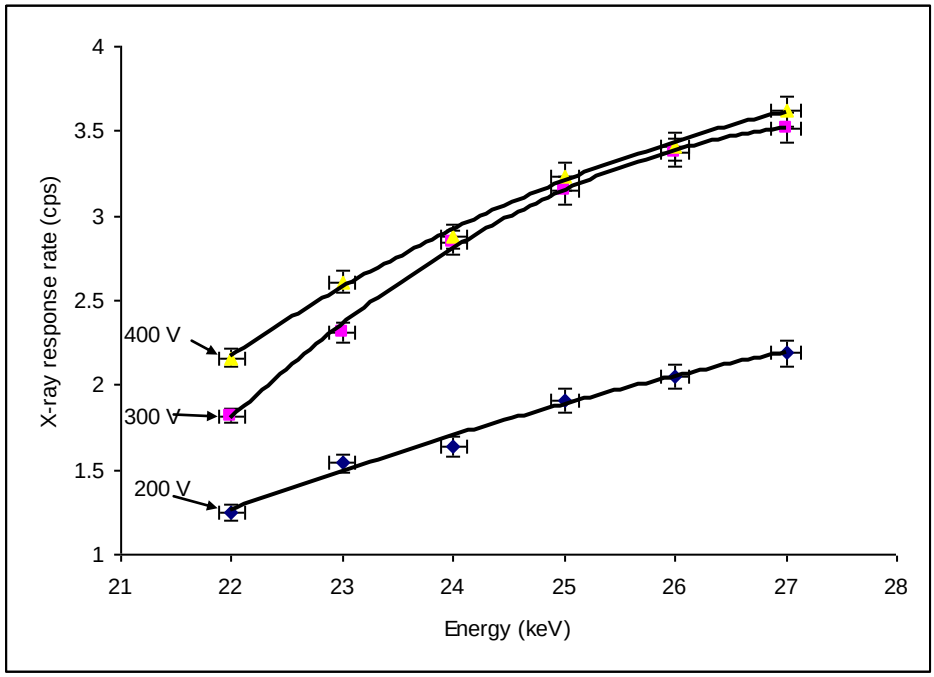


Figure 5.10: Variation of x-ray response rate with energy at different bias voltages

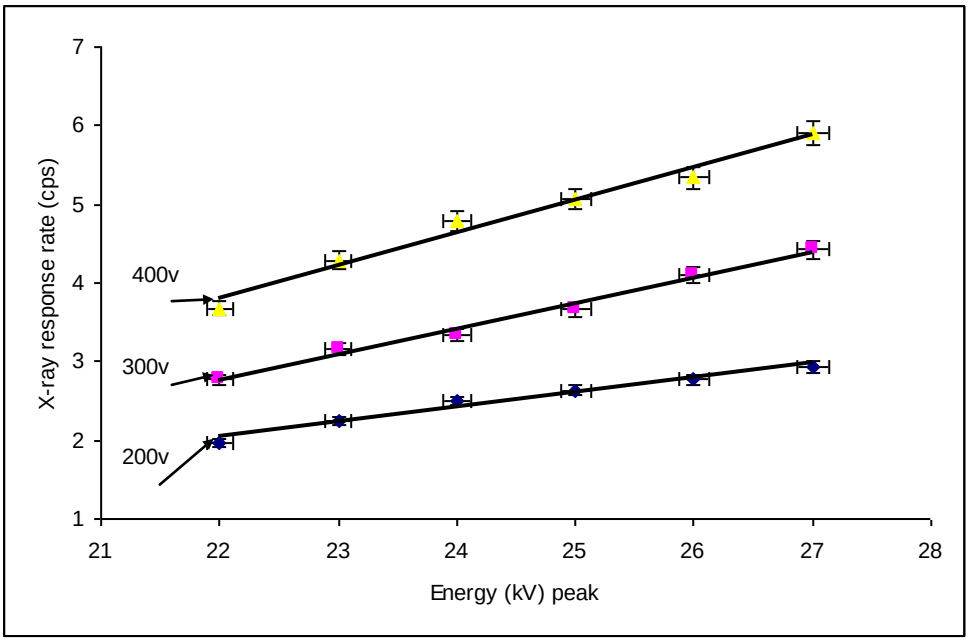


Figure 5.11: Variation of X-ray response rate with energy for Single Crystal (SC) CVD diamond detector at different bias voltages

Figure 5.12 are plots showing the variation of the response rates with applied electrical field for a Detector Grade (DG1) at energy of 22 kVp, an Optical Grade (OG2) at energy of 24 kVp and the Single Crystal at 27 kVp respectively. All the detectors were observed to respond with a positive linear gradient to changes in electrical field i.e. with increase in applied electric field.

Figure 5.13 are plots of the variation of the averaged response rate of all Detector Grade and Optical Grade with bias voltage at 25 kVp setting. The gradients are positive and saturate fitting polynomially. This indicates that on the average the polycrystalline CVD diamonds response to changes in applied electric field is not linear and hence not similar to that of a Single Crystal (Fig. 5.12). The consistency of the performance of the Single Crystal CVD diamond in terms of sensitivity and linearity is observed.

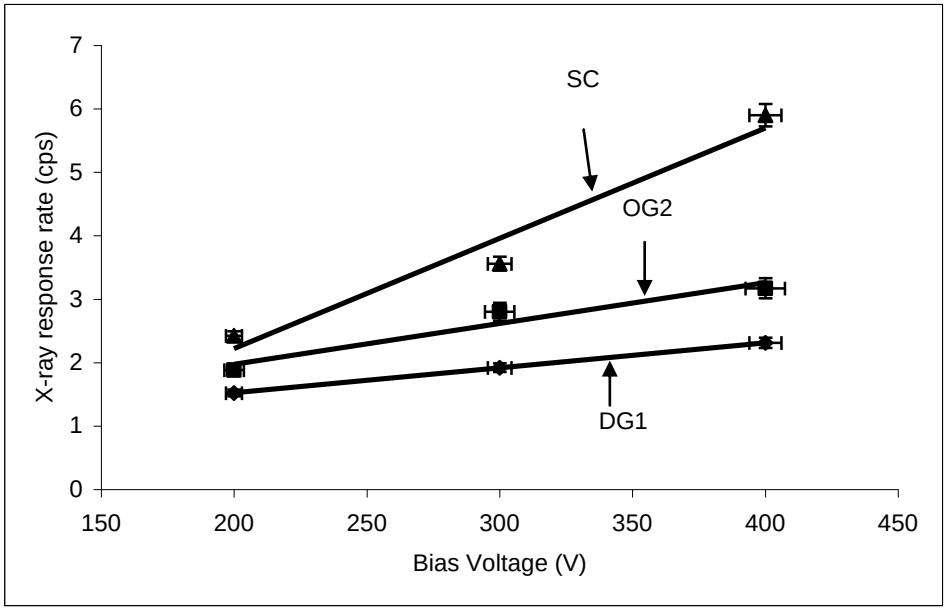


Figure 5.12: Variation of X-ray response rate with bias voltage for DG1 at peak voltage 22kVp, OG2 at peak voltage 24kVp and Single Crystal at peak voltage 27kVp

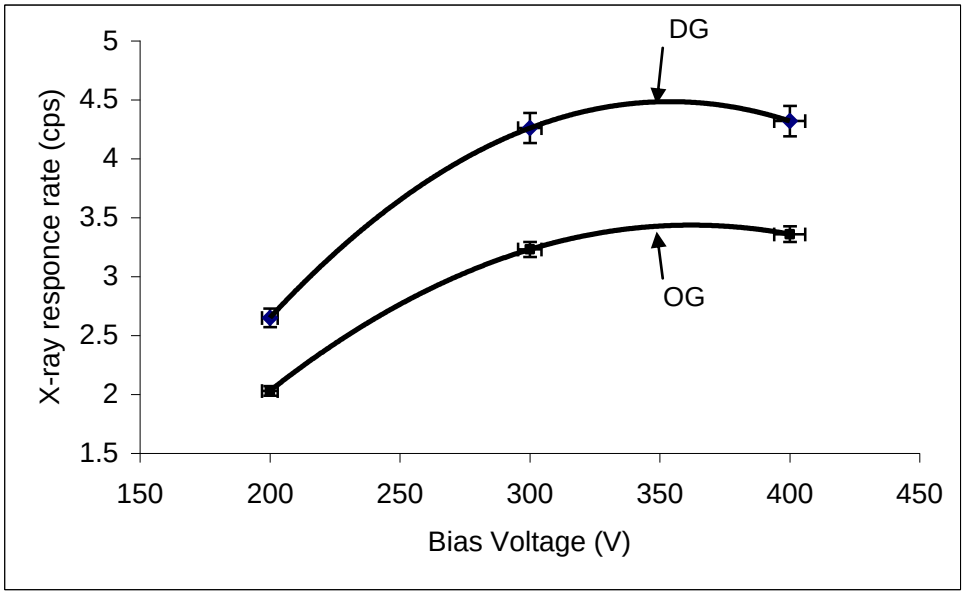


Figure 5.13: Variation of X-ray response rate (averaged) with bias voltage for Detector and Optical Grade CVD diamonds at peak voltage 25 kVp

Figures 5.14 to 5.16 illustrates the variation in X-ray response with the parameters relating their defects and impurity levels. Depicted are the changes of the X-ray response rate with Raman broadening, thermo-luminescence response and single substitutional

nitrogen for both Optical and Detector Grade specimens with both Fig. 5.14 and Fig. 5.16 having negative gradients. This implies therefore, the adverse influences the presence of single substitutional nitrogen and Raman related defects have on all the polycrystalline detectors at all the kVp setting and applied electric field considered.

In contrast Fig. 5.15 illustrates, for the Detector and Optical Grades the increase in X-ray response with increase in TL emission at all energies and applied electric fields. The effects of such parameters were further analyzed for the individual diamond grades; these are depicted in Figs. 5.17 to 5.21.

Figures 5.20 and 5.21 are plots of the variation of X-ray response with the single substitutional nitrogen concentration for Optical Grade detector and that of the Raman broadening respectively for Detector and Optical grade CVD diamonds. The two observations are consistent with the general observations of Figs. 16 and 14 respectively.

Figures 5.11 to 5.19 are different from the above observations. Figure 5.19 depicts the variation of X-ray response rate with TL emission for a Detector Grade CVD diamond whilst Fig. 5.17 and Fig. 5.18 illustrates a variation of X-ray response rate with UV absorption for both Optical and Detector Grade CVD diamond respectively. The observation of Fig. 5.19 is consistent with the general observation of Fig. 5.15. The increase in response with UV absorption for both Optical Grade and Detector Grade CVD, as depicted in Figs. 5.17 and 5.18, we believe, suggests a possible positive influence the presence of UV related defects have on their response.

Unlike Fig. 5.16 which shows the general adverse effect the presence of single substitutional nitrogen has on the response of detectors to photons, Fig. 5.22 shows that within a certain limited range of single substitutional nitrogen concentration values (3.5 ppm to 5 ppm), a slight improvement in response is observed. At concentrations above the 5 ppm level a drop in response is implied. Polynomial fits suggests the presence of interplaying effects the presence of single substitution nitrogen and UV absorption nitrogen vacancy complex have on the detectors. It could be that within the (3.5-5 ppm) single substitution nitrogen concentration the UV effect dominates the detector response and as the single substitutional nitrogen concentration increases beyond 5ppm recombination comes into play resulting in the effect observed in the detectors response. This could be a reason for the relatively better performance of the Single Crystal.

The sensitivity of all the grades of detectors with the different applied electric fields and with the single substitutional nitrogen as well as UV absorption was also analyzed. The sensitivity values were calculated from the gradients of X-ray response rate versus peak voltage.

Figure 5.23 shows that, as the applied electric field is increased, the sensitivity of the detectors increases until the field attains a maximum field value of about 0.6 $kVcm^{-1}$ (300 V bias) before saturation in sensitivity sets in. The observation is consistent with all the three CVD diamond grades. Of note is the observation of the response rates of all the three CVD diamond grades as depicted in Figs.5.12 and 5.13 which increase linearly with

increase in bias voltages, here the sensitivity does not increase linearly with the applied electric field.

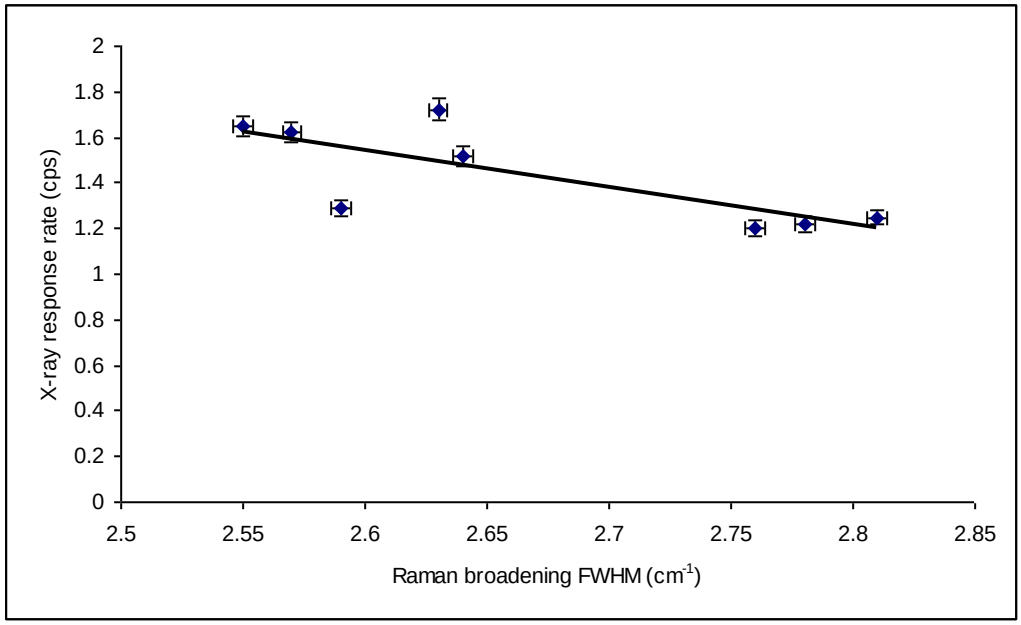


Figure 5.14: Variation of X-ray response rate with Raman broadening for Detector and Optical Grade CVD diamond detectors

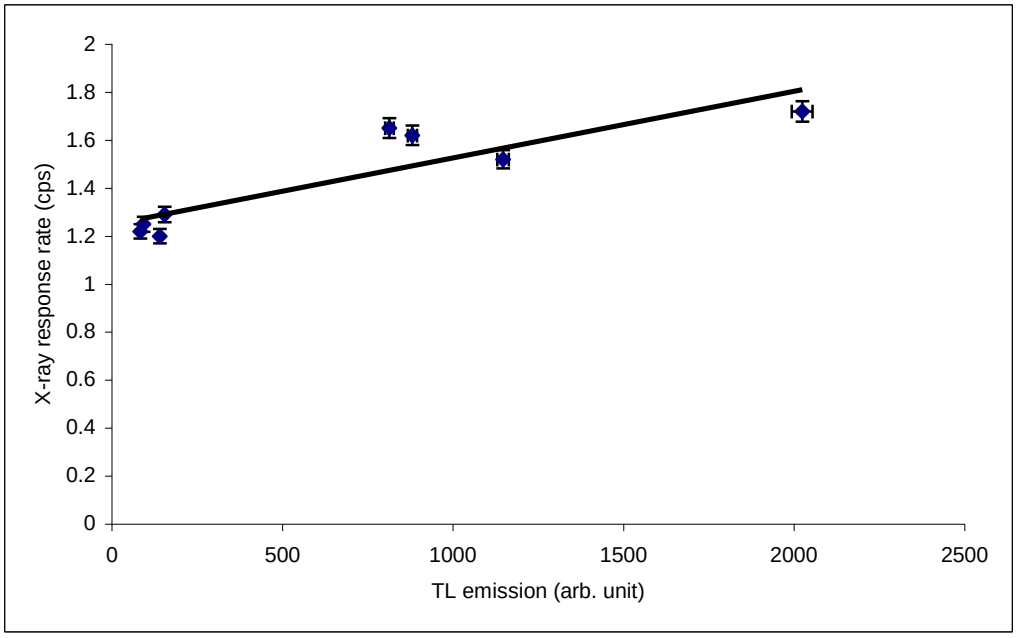


Figure 5.15: Variation of X-ray response rate with TL emission for Detector and Optical Grade CVD diamond detectors

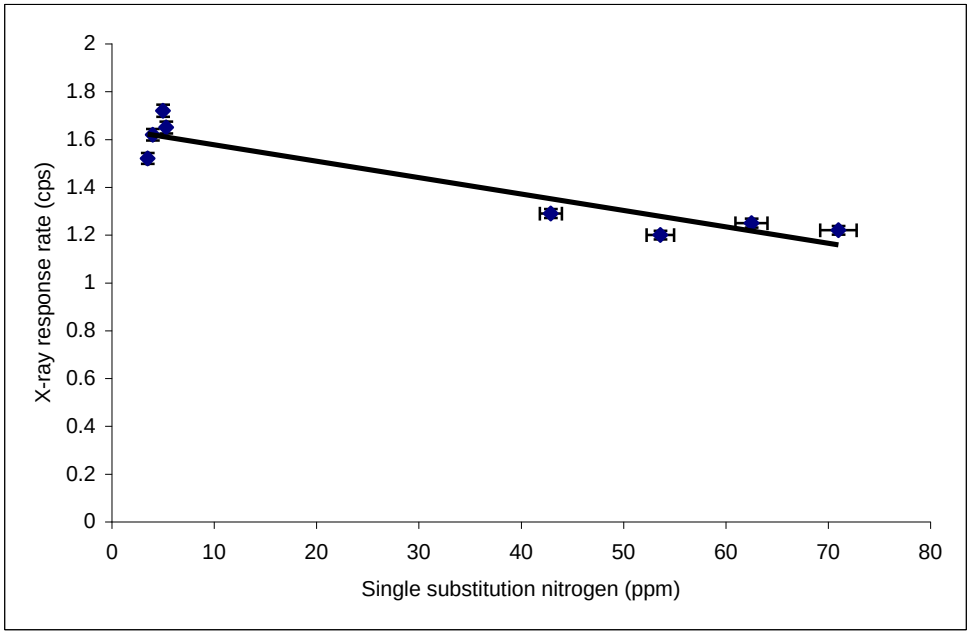


Figure 5.16: Variation of X-ray response rate with single substitutional nitrogen concentration for Detector and Optical Grade CVD diamond detectors

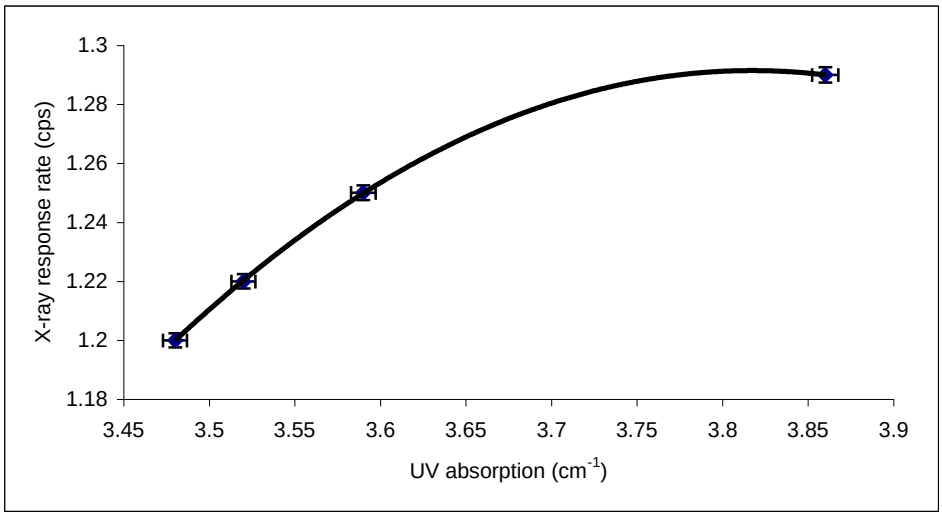


Figure 5.17: Variation of X-ray response rate with UV absorption for Optical Grade CVD diamond detectors at a peak voltage of 22 kVp and 200 V bias

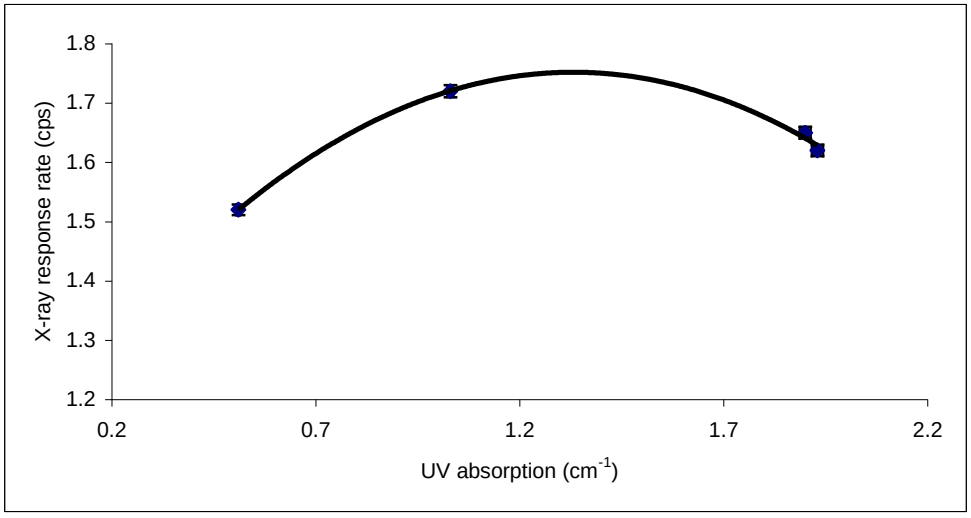


Figure 5.18: Variation of X-ray response rate with UV for Detector Grade CVD diamond detectors at a peak voltage of 22 kVp and 200 V bias

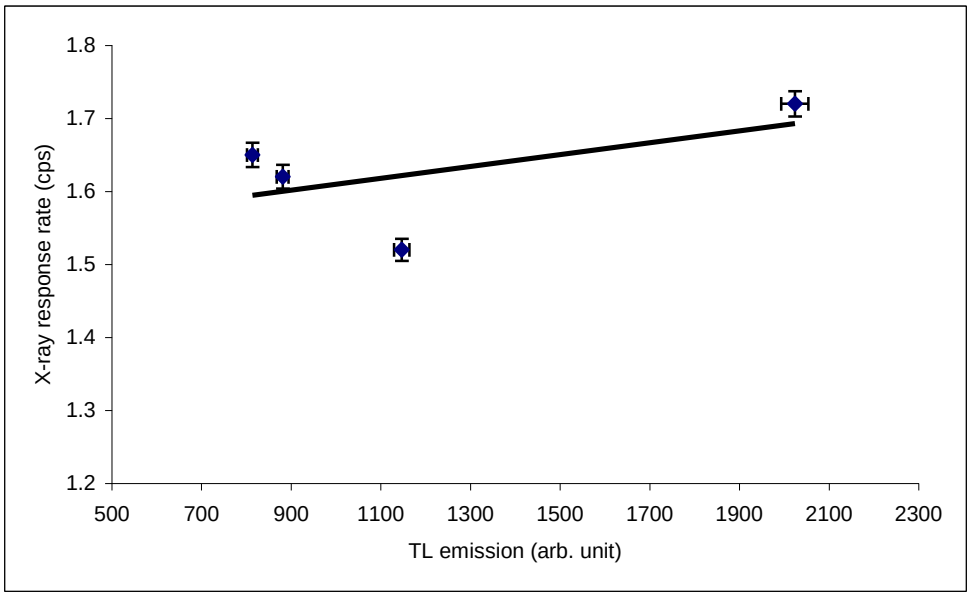


Figure 5.19: : Variation of X-ray response rate with TL emission for Detector Grade CVD diamond detectors at a peak voltage 22 kVp and 200 V bias

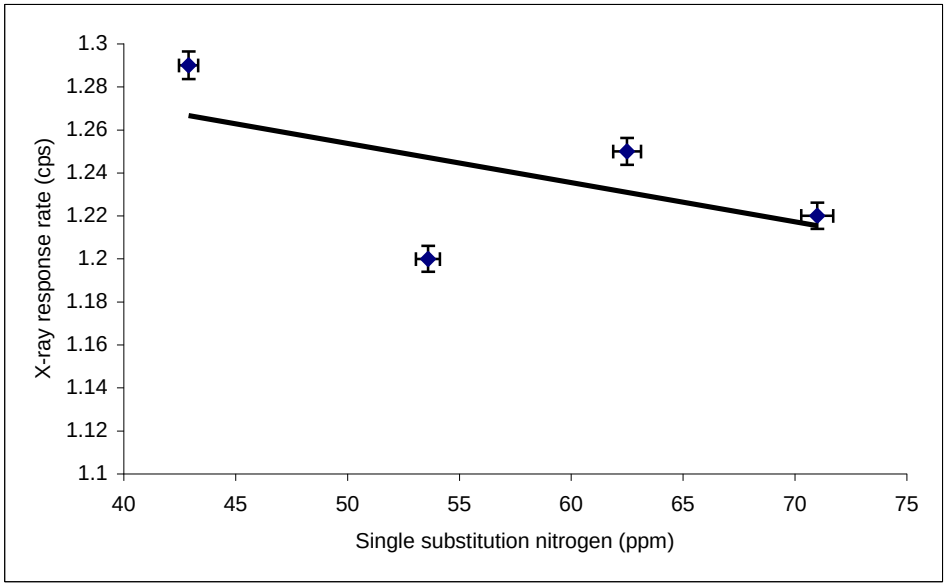


Figure 5.20: Variation of X-ray response rate with single substitutional nitrogen for Optical Grade CVD diamond detectors at peak voltage of 22 kVp and 200 V bias

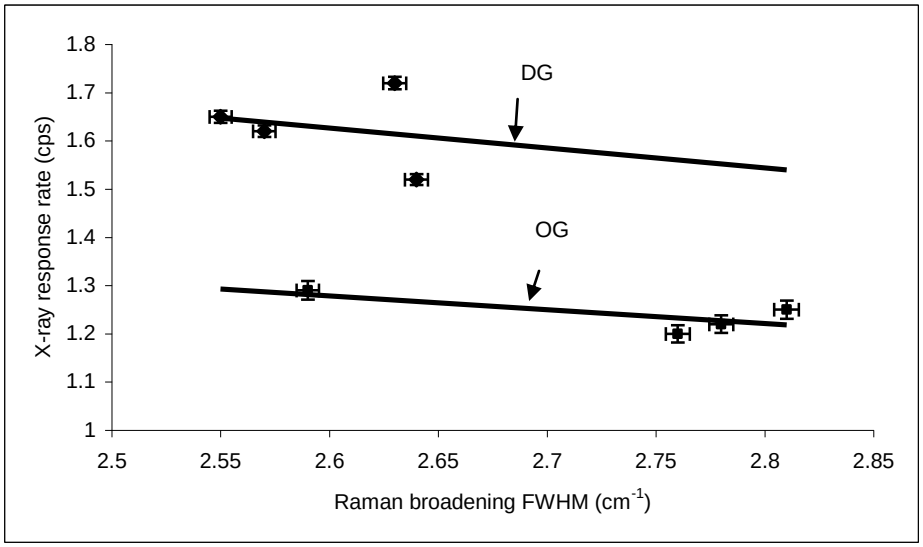


Figure 5.21: Variation of X-ray response rate with Raman broadening for Detector and Optical Grade CVD diamonds wafers at peak voltage of 22 kVp and 200 V bias

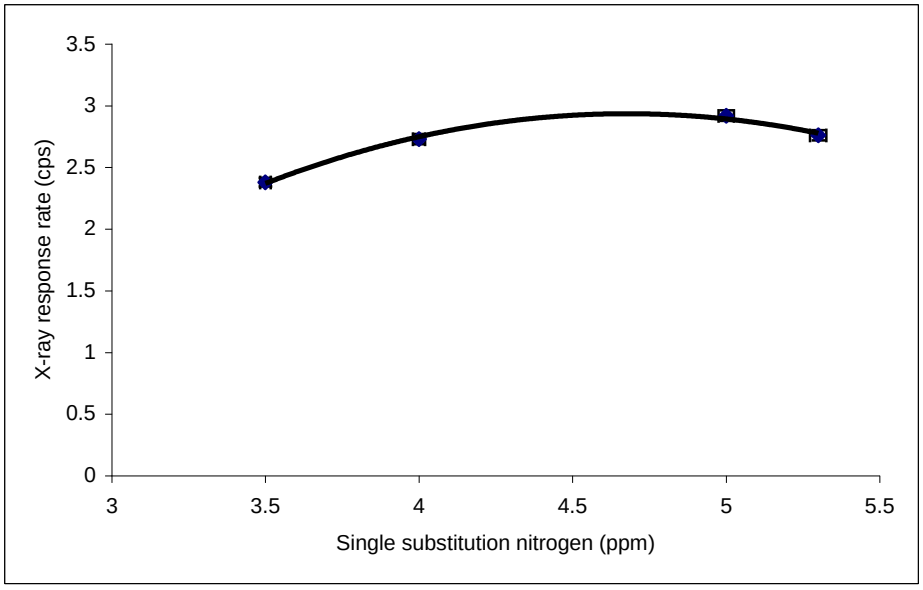


Figure 5.22: Variation of X-ray response rate with single substitutional nitrogen for Detector Grade CVD diamond detectors at a peak voltage of 23 kV and 300 V bias

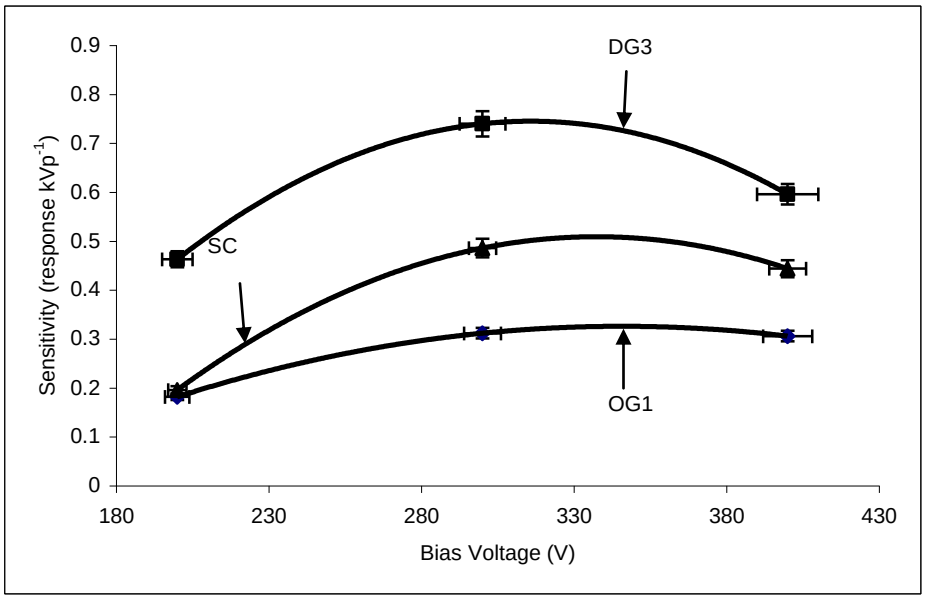


Figure 5.23: Variation of sensitivity with bias voltage for Detector Grade (DG3), Optical Grade (OG1) and Single Crystal CVD diamonds

Figures 5.24 and 5.25 again highlight the interplay between the single substitution nitrogen and UV absorption nitrogen complex at the low nitrogen concentration values on the detector sensitivity. These are consistent with the observations of Fig. 5.22. The same

observation of the decrease in sensitivity with the presence of UV absorption nitrogen (the UV absorption value of above 1.5 cm^{-1}) could be due to more dominated role of ESR nitrogen coming into play above the 5 ppm level giving rise to the observed decrease in the detectors sensitivity as depicted in Fig. 5.25.

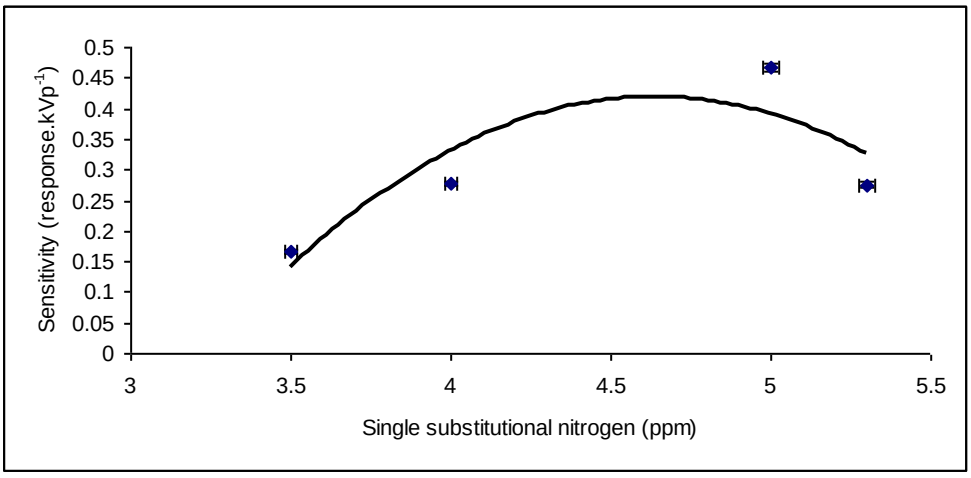


Figure 5.24: Variation of sensitivity with single substitutional nitrogen concentration for Detector Grade CVD diamonds at 200 V bias

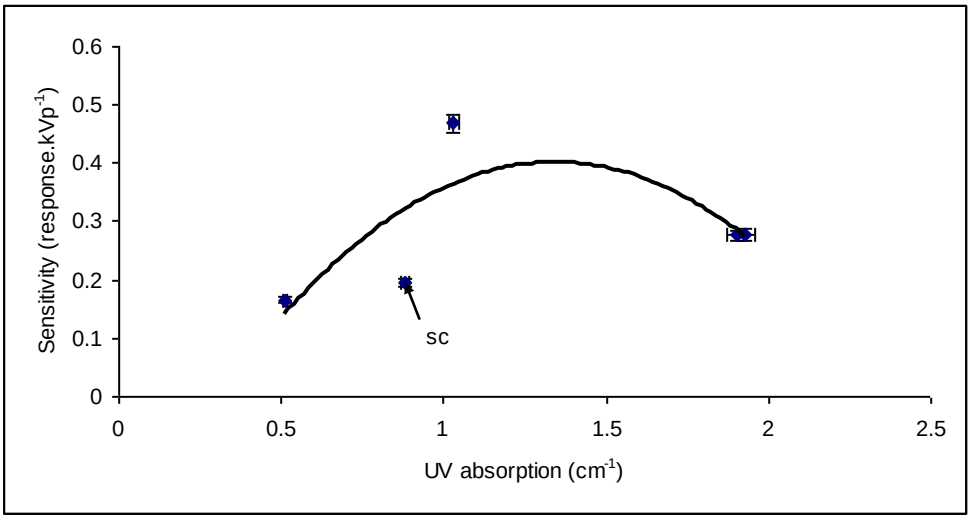


Figure 5.25: Variation of sensitivity with UV absorption for Detector Grade and SC CVD diamond at 200 V bias

5.6 Conclusion

The analyses of the low energy X-ray response with the three grades of wafers (DG, OG and SC) were based on the sensitivity and the linearity of their response rate at different kVp settings and at different applied electric fields. The presence of defect related parameters and impurities of the wafers were also used to further explain the observations made on the sensitivity and linearity when used as detectors. The observed differences in resistivity of the specimens are part of the reason for the observed differences in the X-ray response rate. It also explains the reason for the observed lower X-ray responses of the Single Crystal, despite its relative purity in terms of defects and impurities.

The single Crystal and Detector Grade CVD diamond specimens are observed to perform linearly with the variation in X-ray response rate with the X-ray peak voltage setting (kVp) while the Optical Grade saturates at peak voltage setting above 25 kVp.

All the CVD types (DG, OG and SC) are observed to behave consistently, displaying increase in sensitivity with increase in applied electric field (between 0.4 kV^{-1} cm and 0.8 $kV.cm^{-1}$) up to an optimum value of about 0.6 $kV.cm^{-1}$. The sensitivity values then saturate with further increase in applied electric field.

The study has shown that both the response (linear or non-linear) and the sensitivity of the wafers to X-ray photons are susceptible to the presence of defects in the crystal. These defects contribute either positively (as in the case of Detector Grade) or negatively (as in the case of the Optical Grade) to the performance of the detector. The Detector

Grade and Single Crystal CVD diamonds are observed to be consistently better in performance as X-ray probe in terms of linearity and sensitivity than the Optical Grade diamond.

One of the reasons for the relatively low performance of the Optical Grade specimens as X-ray sensors could be ascribed to the observed characteristics of the diamond wafers namely the much higher presence of single substitutional nitrogen concentration.

The other reason for the consistently poor performance of the Optical Grade could be attributed to the presence of the relatively larger concentration of grain boundary related type of defects that are associated with observed Raman broadening; giving rise to trapping and de-trapping of charge carriers. The presence of single substitutional nitrogen and the overall lower availability of created charged carrier at higher kVp setting are presented as the possible reason for the indicated saturation at the higher X-ray peak energies.

The relatively better performance of the Detector Grade in general and DG3 in particular could on the other hand be related to the impurity concentrations analyzed by UV absorption values. This could also be the reason for the observed improved performance of a Single Crystal CVD diamond. The relation between the plots of Fig. 5.24, showing the presence of an optimum single substitutional nitrogen concentration (4.64 ppm) and that of an optimum concentration of UV related nitrogen complex (1.28 cm^{-1}) in Fig.

5.25, hints at the existence of a proportionally related factor relating to the two types of impurities.

For a choice of X-ray dosimeter, the specimen must have a high TL emission and UV absorption but a low Raman broadening and single substitutional nitrogen concentration. The preferred choice, based on our analysis, is the Detector Grade (DG3 in particular) CVD diamond however the most consistent wafer tested was the Single Crystal.

5.7 References

Assiamah M 2004. *PhD thesis. University of the Witwatersrand, Johannesburg, South Africa*

Burgemeister EA 1981. *Phys. Med. Biol*. **26(2)** 269

Dean PJ 1965. *Phys. Rev*. **139 A**588

Gerrish VM 1995. *Simiconductors Semimetals* **43** 493

Grobbelaar J.H, Burns RC, Nam TL, and Keddy RJ 1991. *Nucl. Instrum. Methods. Phys. Res*.**B61** 553

Hecht K 1932. *Z. Phys. (Berlin)* 235

Herzberg IG 1945. *Infrared and Raman Spectra of Polyatomic Molecules, Van Nostrand Reinhold, New York*

Iakoubovskii K, Stesmans A, Suzuki K, Sawabe A and Yamada T 2002. *Phys. Rev*. **B66** 113203

Keddy RJ, Nam TL, and Burns 1987. *Phys.Med.Biol*. **32(6)** 751

Manfredotti C, Fizzotti F, Vittone E, Polesello P, Jaksic M, Fazinic S and Bogdanovic I 1996. *Italian Physical Society* **52** 59

Marinelli M, Milani E, Paoletti A, Tucciarone A, Verona- Rinati G, Angelone M, and Pillon M 1989. *J. Appl. Phys*. **89** 1430.

Mavunda R.D, Zakari YI, Nam TL, Keddy RJ 2008. *Appl. Radiation and Isotopes* **66** 1128

Nam TL 1989. *PhD thesis, University of the Witwatersrand, Johannesburg, South Africa*

Nam TL, Karfunkel U, Keddy RJ and Every AG 1991. *Radiation effect and defects in solids* **116** 233

Nebel CE 2003. *Semicond.Sci. Technol*. **18** S1

Sciortino S 1999. *Riv. Nuovo Cimento* **22** 1

Souw EK and Meilunas 1997. *Nucl. Instrum. and Methods in Phys. Research* **A400** 69

Van der Merwe DG 1994. *PhD thesis, Faculty of Science. University of the Witwatersrand, Johannesburg, South Africa*

Chapter 6

ANALYSIS OF A SIMULATED LOW ENERGY X-RAY MAMMOGRAPHIC MODEL WITH MONTE-CARLO CODE (PENELOPE) FOR A VALIDATION OF THE EXPERIMENTAL PERFORMANCE OF THE CVD DIAMOND DETECTORS

6.0 Abstract

The impurity/defects concentration of different grades of CVD diamond polycrystalline and single crystal was assayed for use to analyze their effect on the X-ray dosimetric performance of diamond crystals. A model of the experimental set-up was simulated and the detectors absorbed dose calculated using a Monte Carlo code (PENELOPE). The observed trend of the simulated plot for a pure diamond with a slight negative effect to change in peak voltage was used to validate the experimental observations of the (impurity/defect prone) detectors performance as an X-ray dosimeter.

6.1 Introduction

In Chapter 4, the analysis of the molybdenum spectrum from mammography X-ray unit was corrected for comparison with the simulated spectrum. The corrected spectrum was observed to correlate well with the simulated spectrum in terms of energy and intensity. This motivated the use of the simulated mammography X-ray to analyze diamond wafers in this Chapter.

High energy photons, electrons and positrons penetrating matter suffer multiple interactions, by which energy is transferred to the atoms and molecules of the material and secondary particles are produced.

During simulation of radiation transport, the history (tracks) of a particle viewed as a random sequence of free flights that ends with an interaction event where the particles change direction, loose energy and produces secondary particles, or passes through without interacting with the medium it traverses (Salvat et al., 2001).

It has been established that all Monte Carlo calculations are equivalent to integrations at least in a formal sense (James, 1980), thus permitting formal theoretical foundation for MC technique. Algorithms for MC calculations are well established and available in literature (Nelson et al., 1985; Bielajew et al., 1994; Bielajew et al., 1994 Bielajew et al., 1994 and Baró et al., 1995). The CVD diamond response to X-ray was simulated using Monte Carlo code (PENELOPE). The algorithm used in PENELOPE simulation code system is based on equation 6.1, where N is number of random points, x_i, from the probability distribution functions (PDF) $p(x)$ and $f(x_i)$ is the sum of values accumulated in a counter.

$$\bar{f} \equiv \frac{1}{N}\sum_{i=1}^{N} f(x_i) \qquad 6.1$$

Applying series of statistical theories to equation 6.1, the PDF of $\bar{f}$ is estimated as:

$$p\left(\bar{f}\right) = \frac{1}{\sigma_f \sqrt{2\pi}} \exp\left(- \frac{\left(f - \left\langle \bar{f} \right\rangle \right)^2}{2\sigma_f{}^2} \right) \qquad 6.2$$

If the limit $N \rightarrow \infty$, the PDF of $\left\langle \bar{f} \right\rangle$ is a normal (Gaussian) distribution with mean $\left\langle \bar{f} \right\rangle$ and standard deviation σ_f, the interval $\left\langle \bar{f} \right\rangle \pm n\sigma_f$ contain the exact value $\left\langle \bar{f} \right\rangle$ with a probability of 68.3 % if N =1, 95.4 % if N =2 and 99.7 % if N =3 (3σ rule) (Salvat et al., 2006). The simulation algorithm of PENELOPE is based on a scattering model that combines numerical databases with analytical cross section models for different interaction mechanisms and is applicable to wide energy range, from a few hundred eV to 1 GeV. Photon transport is simulated by means of the standard, detailed simulation scheme. The code performs "analogue" simulations i.e. simulated showers are intended to be replicas of actual showers of electron-photon simulations in infinite media of various compositions. The principles and basic theory of the MC algorithms employed in the simulation code, PENELOPE, used for this study has been well presented in the user's manual for the code (Salvat et al., 2006).

Salvat et al. has shown, in their work that the outcome of MC code is affected by statistical uncertainties, similar to those found in laboratory experiments. Thus the proper evaluation of statistical uncertainties is important in order to determine the accuracy of the MC result.

Monte Carlo (MC) methods are used to solve such complex physical and mathematical problems (James, 1980; Rubinstein, 1981; Kalos and Whitlock, 1986). The degree of

accuracy to which the physical parameters are measured with exact and sufficient statistics makes Monte Carlo method superior to other deterministic and analytical methods. The EGS4- electron shower version 4 (Nelson et al., 1985; Bielajew et al., 1994); EGSnrc extended and improved version of EGS4 for calculating the response of ion chambers used in Medical Physics; ETRAN-electron Transport code and ITS-intergrated Tiger Series (Nelson et al., 1985; Bielajew et al., 1994); GEAT MC simulation tool originally developed at CERN for high energy physics experiments; MCNP- neutron particle transport code (Briesmeister, 1993) and PENELOPE (Baró et al., 1995; Salvat et al., 1996; Sempau et al., 1997) PENetration and Energy Loss of Positrons and Electrons; are some of the MC codes available but new improved versions are continuously developed to solve practical problems that unfold. PENELOPE enhance transport algorithms (Salvat et al., 2001) and is based on scattering models for different interaction mechanism, and is used to assess the attenuation coefficient (μ) (Basyigit et al., 2005) and to measure the probability of all possible interactions between photons and atoms. The simulation is intended to be similar to the actual showers of electron-photon in infinite media of various compositions. It is assumed that, in the region where the particles move, there is an electric field and a magnetic field, which are set up by external sources and do not vary with time (Salvat et al., 2001) and both fields are continuous functions of the position vector.

Mammography X-ray beam deposited energy has been assessed with Monte Carlo simulation by Doi and Heang-Ping 1980, Dance, 1980; Monte Carlo simulation has also been used to calculate integral radiation dose in xeromammography. Some investigations

on mammography techniques using the MC code include calculation of conversion factors for the estimation of mean glandular dose (Dance, 1980); backscattered factors for mammography calculated by Kramer et al. (2001).

Monte Carlo simulation of X-ray spectra generated by kilo-electron volt electrons was described by Salvat, (2003) and recently calculated low energy X-ray beams simulated with PENELOPE by Assiamah, 2004.

The present work aims at validating the experimental results of low energy X-ray mammography when probed with CVD diamond wafers and modeled for MC simulation to calculate the deposited energy. The same molybdenum spectrum corrected for in Chapter 4 for fluctuations and energy range dependent of the detector (Fig. 4.13) was used to simulate the diamond in this presentation.

6.2 PENELOPE code

PENELOPE is implemented in a FORTRAN 77 computer code and runs on a platform with a FORTAN 77 compiler. The code was installed and run on a 3 GHz Pentium 4 Intel processor and 1023 MB RAM personal computer. The source files of the PENELOPE code include: the transport and physical routines (Penelope.f). This is a simulation subroutine package that provides the steering programs, which controls the geometry and evolution of tracks, keeps score of the relevant quantities and performs the required

averages at the end of the simulation; variance-reduction sub-routines (Penvared.f) calculates the errors and; the quadratic geometry routines (Pengeom.f) involves space displacements, interface crossings, identify bodies and materials present at interfaces. The main program creates cross-section data files (material.f). The information about each material i.e. tables of physical properties, interaction cross sections, relaxation data and densities are stored and read; the main program used to generate the bremsstruhlung (Penslab.f); sample input data file (Penslab.in); the interaction of photons with the material to give photoelectric absorption routines (Pencyl.f). The (Pencyl.in) file describes the geometry of the file. Other routine files such as material.exe for creating material cross section data; GNUPLOT for plotting simulated results; timer.f a subroutine used in setting time during simulation process and GVIEW software for geometry visualization. Compilation and linking the code were performed by following the instruction such as: g77-0 Penslab.f, timer.f and penslab.exe.

6.3 MAIN programs and the Input Files

The new version (2006) of the distributed package of the PENELOPE code includes various examples of MAIN programs which include the Penslab.f (which simulates electron-photon in slabs); Pencyl.f (for transport in cylindrical geometry); and Penmain.f (generic quadric geometries). PENELOPE must be complimented with a steering main program which controls the geometry and the evolution of tracks, keeps track of the relevant quantities and performs the required averages at the end of the simulation.

The main program is connected with the PENELOPE via:

KPAR: –kind of particle to be used for the simulation (1-electron; 2-photon; 3-proton)

IBODY:-which identifies different bodies in a complex material structure.

MAT:-identifies the material through which the particles move.

ILB (5):- the auxiliary array of 5 labels that describes the origin of the secondary particles.

The position coordinates r = (X, Y, Z) and the direction cosines d = (U, V, W) of the direction of movement are referred to a fixed "laboratory" system which can be arbitrarily defined. During simulation, all energies are expressed in eV and lengths in cm.

A detailed simulation report includes a relevant input data as well as a main program filename.dat. These files are in a format suited for direct visualization with GNUPLOT. The generic program Penmain performs simulations of electron-photon transport in complex material structure. Penmain is devised to allow occasional users to employ PENELOPE without having to write their own main program.

The geometry of the material system is described by the package PENGEOM which is able to handle complicated geometries very efficiently. The operation of the main program is completely controlled from the input data file. Penmain is flexible enough to solve a broad class of practical problems.

The input files are written according to specific order and format with explicit 6-character (filled with blank if less) keywords followed by numerical data or character string. The 6-character keywords identify the simulation parameters such as the kind of particles being simulated in the energy and position from target, its angular aperture described by the polar and azimuthal angles with respect to z-axis, the default axis vector direction for any beam, number of materials in the geometry being simulated, the material and geometry filenames. The input file also includes the cut-off absorption energies (for each material), the desired number of the simulated showers and the simulation time. All the main programs were used to simulate the molybdenum target to acquire the photon backscattered spectra with Penslab; simulate and filter the spectra to obtain the filtered spectra using Pencyl and the Penmain used to calculate the absorbed dose in the modeled diamond probe together with the contacts. The programs thus generated, filtered the spectra and used the spectra energy distribution to simulate the exact experimental set-up.

6.4 Generation of Low energy X-ray spectra

Electron interaction mechanism in the code involves artificial soft event (random hinge), hard elastic collision, hard inelastic collision and hard bremsstrahlung emission as a result of the acceleration caused by the electrostatic field of atoms swift electrons (Salvat et al., 2001). An electron with kinetic energy generates a photon of energy W, which takes values in the interval from 0 to E. Using the Penslab geometry as the main program to model for a molybdenum target, the electrons were accelerated to the molybdenum

target where the interaction resulted in the bremsstrahlung of molybdenum target similar to that produced by the mammography X-ray unit with peak energy values of between

22 keV and 27 keV. These were measured as the backscattered photons from the molybdenum. Simulation of photoelectric absorption of electrons resulted in K-shell X-rays at 17.5 keV and 19.5 keV and Auger electron emissions. The unfiltered simulated spectrum of molybdenum is presented in Fig. 6.1.

Using the Pencyl geometry to model for the cylindrical layers of the beryllium (0.084 cm); aluminium (0.0003 cm) and 50 cm layer of air for filter the spectra of undesirable energies. The resulting filtered spectra were acquired as the transmitted photons at the lower X-ray energy range 22 keV to 27 keV. Attenuation of soft energy bremsstrahlung by beryllium window, tungsten mirror and air was simulated and the resulting spectrum Fig. 6.2 was obtained.

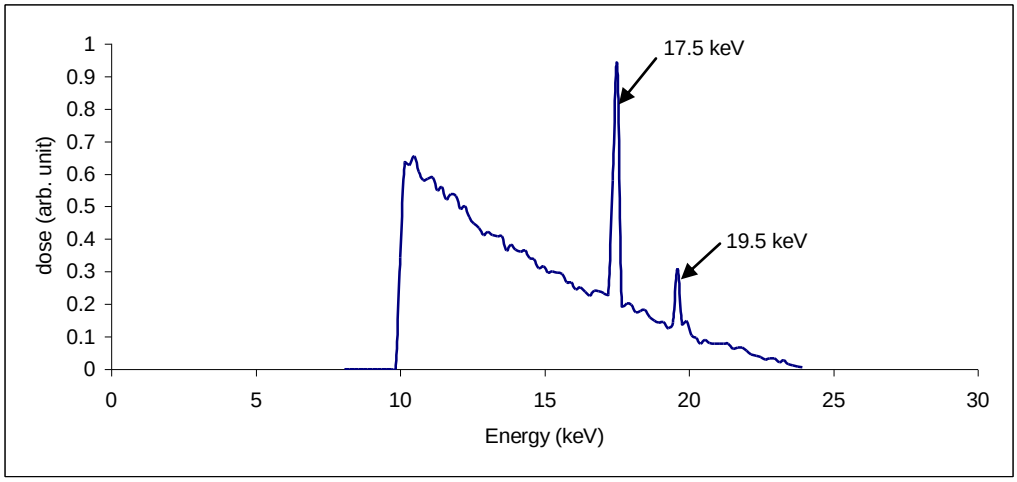


Figure 6.1: Molybdenum spectrum for 24 keV energy before attenuation by berylium window; molybdenum mirror and air.

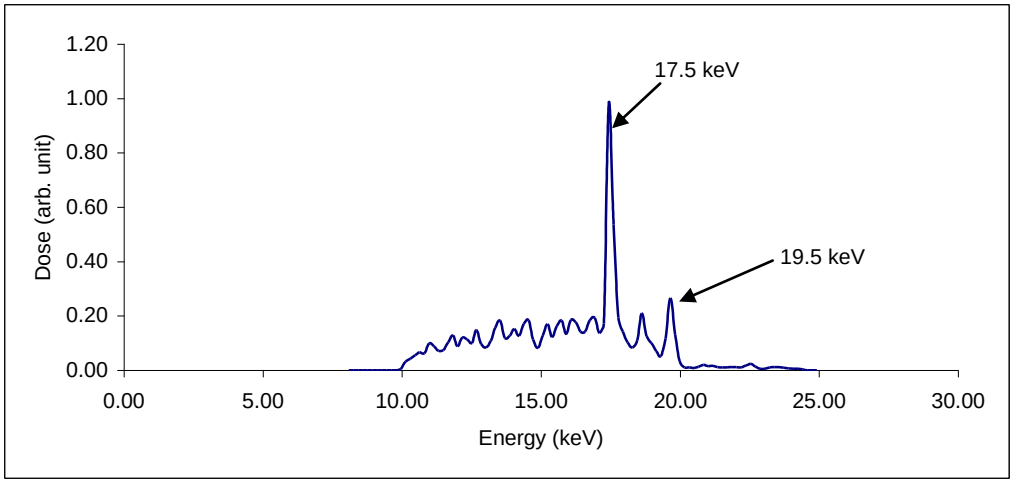


Figure 6.2: Molybdenum spectrum for 24 keV energy, after attenuation by berylium window, molybdenum mirror and air (after filtering)

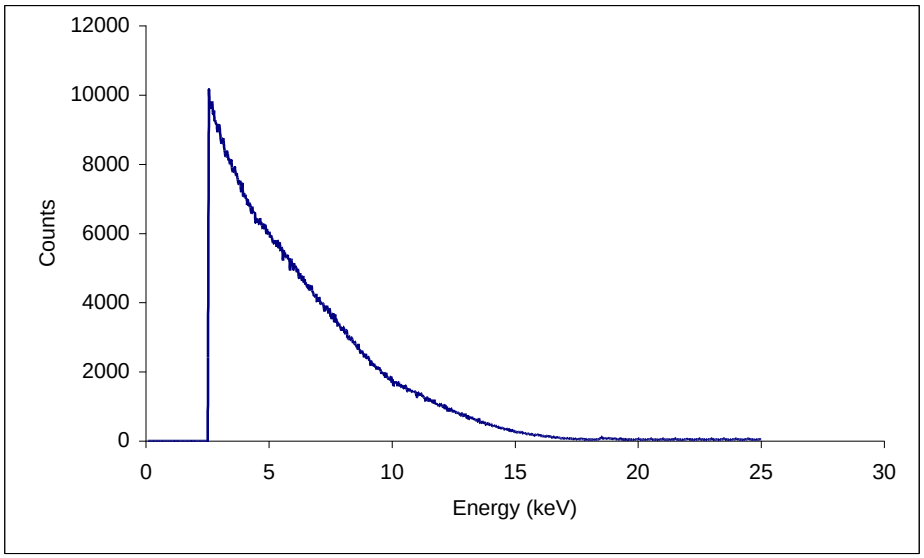


Figure 6.3: A typical mammography X-ray spectrum obtained from CVD diamond

Figure 6.3 show an experimental molybdenum spectrum obtained using a CVD diamond detector. The energy peaks could not be resolved due to pile-up of low energy signals and the shaping time of the signal.

6.5 Simulation for the absorbed dose in diamond with the generated X-ray spectra

The spectrum simulated from the molybdenum target Fig. 6.2 at energy 22 keV was used to interact with pure diamond detector modeled with the platinum, titanium and gold contacts. Interaction in the code involves coherent (Rayleigh) scattering, incoherent (Compton) scattering, photoelectric absorption and electron-positron pair production in CVD diamond detector. Photon interaction cross section occurring in the material is presented in Fig.6.3.

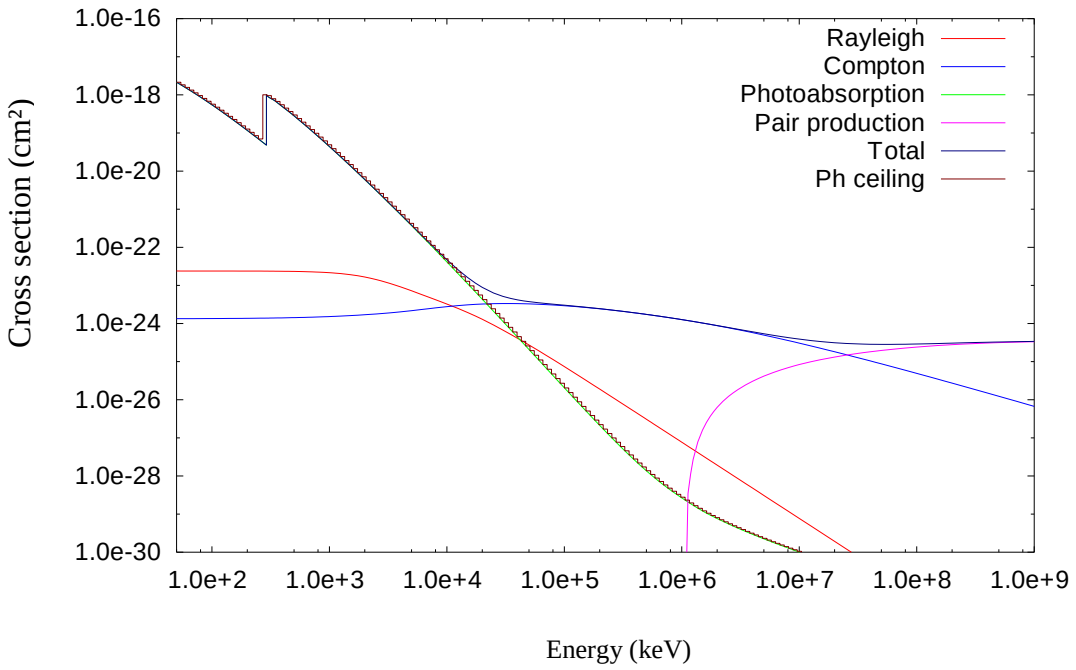


Figure 6.3: Variation of photon interaction cross section of pure diamond with energy

The photon mass attenuation coefficient for pure diamond detector is presented in Fig. 6.4. The energy deposited is also related to the photon mean free path Fig. 6.5

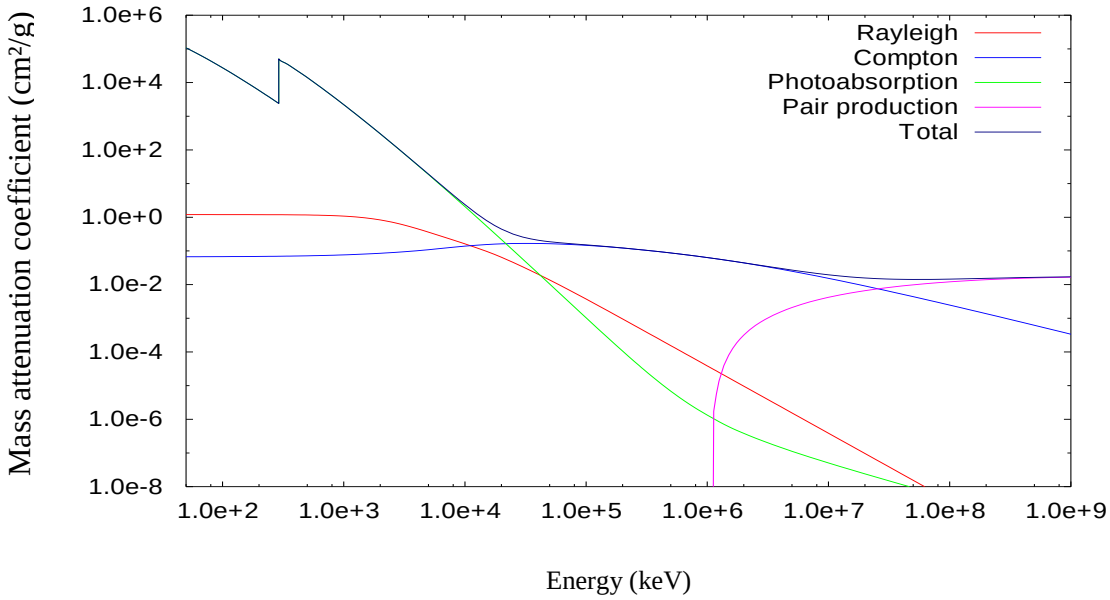


Figure 6.4: Variation of photon mass attenuation coefficient of pure diamond with energy

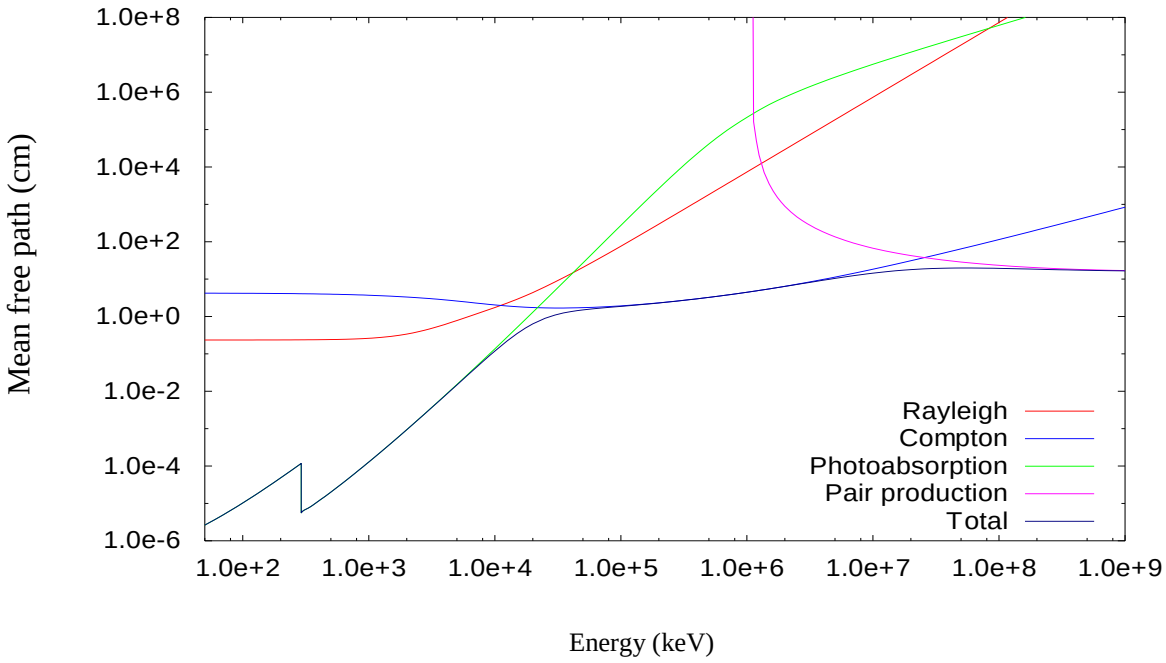


Figure 6.5: Variation of photon mean free paths of pure diamond detector with energy

6.6 The input file

In this work, the MAIN program PENMAIN was used to simulate the deposited energy (eV) when 22 keV to 27 keV photon spectra interact with the pure diamond detector

applied in the experimental set-up. The geometric file defines the thickness of the material where interaction takes place. The material file defines the type and number of materials in the model, as well as the order of arrangement. The input file defines the source position and direction. An aperture of 5.7 degrees of photon source placed in vacuum at a distance of 2.0 cm from the detector was incident on the pure diamond. The energy bins obtained from data energy Fig. 6.2 were employed for the simulation of each energy applied i.e., 22 keV to 27 keV.

6.7 Results and Discussion

The simulated results, for the bare diamond, metalized diamond together with the experimental results of the mammography X-ray photon interaction with the diamond wafers are tabulated in Table 6.1. Also tabulated is the simulated energy deposited in the platinum, titanium and gold contacts showing the contribution of each on the performance of the diamond wafers. Figure 6.6 is a plot of the variation of absorbed dose with X-ray peak voltage (22 kVp to 27 kVp) for the platinum, titanium and gold contacts. All plots showing a positive gradient of 0.00012 for platinum, 0.00006 for titanium and 0.002 for gold. The plot shows the interaction of the metals to X-ray to be consistently increasing with increasing peak voltage.

Figure 6.7 is a plot of the variation of absorbed dose with X-ray peak voltage used with the mammography X-ray tube (22 kVp to 27 kVp). For the simulated pure diamond and

the metalized diamond the plots depicts a parallel linear graphs with negative gradients of 0.0145 for plane diamond and 0.013 for the metalized diamond,

The two plots Fig. 6.6 and Fig. 6.7 show that the plane diamond performance was not altered by the metallization but alter the sensitivity of the diamond by 6 %. The effect of metalized metals with diamond as positive in gradient could be the reason for the slight decrease gradient of 0.0015 for the metalized diamond.

The plot of Fig. 6.8 depicts the observed trend of the simulated X-ray response for a metalized CVD diamond using the PENELOP. The graph is observed to be negatively related to peak voltage. It suggests that the difference in gradients of the plots of experimental absorption and the simulated plots could be due to the effect of the impurities discussed in Chapter 2 on the performance of the diamond wafer. The observation in Chapter 5 that the impurities sensitive and linearise the detectors performance is further confirmed. While the simulated metalized diamond is observed with a negative gradient of 0.0013 the experimental plots are on the average having a positive gradient value of 0.28 except the Optical Grade CVD wafers that depicts saturation at above 25 kVp**.**

Table 6.1: Variation of X-ray response rate with energy for DG1, OG1 and SC CVD diamond detectors and the absorbed dose of a simulated plane and metalized diamond, with platinum, titanium and gold contacts.

Energy KeV	DG1	OG1	SC	Simulated and metalized diamond	Plane Diamond	Platinum	Titanium	Gold
22	1.52	1.29	1.35	1.114	1.0521	0.0160	0.0044	0.0618
23	1.64	1.57	1.74	1.100	1.0357	0.0162	0.0044	0.0641
24	1.72	1.76	1.86	1.084	1.0186	0.0164	0.0045	0.0662
25	1.95	1.95	2.1	1.074	1.0067	0.0164	0.0046	0.0676
26	2.18	2.1	2.21	1.058	0.9894	0.0165	0.0047	0.0697
27	2.35	2.2	2.42	1.049	0.9797	0.0166	0.0047	0.0707

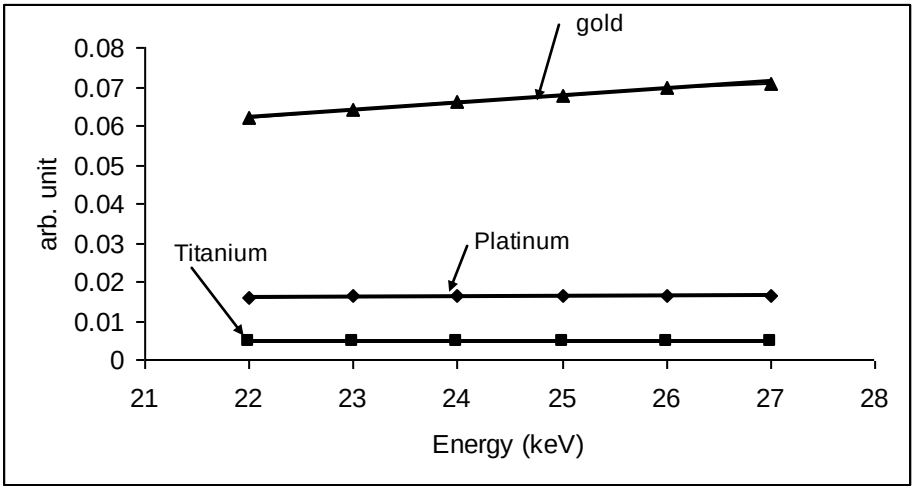


Figure 6.6: Variation of absorbed dose with X-ray peak energy for a Monte Carlo simulation on platinum, titanium and gold

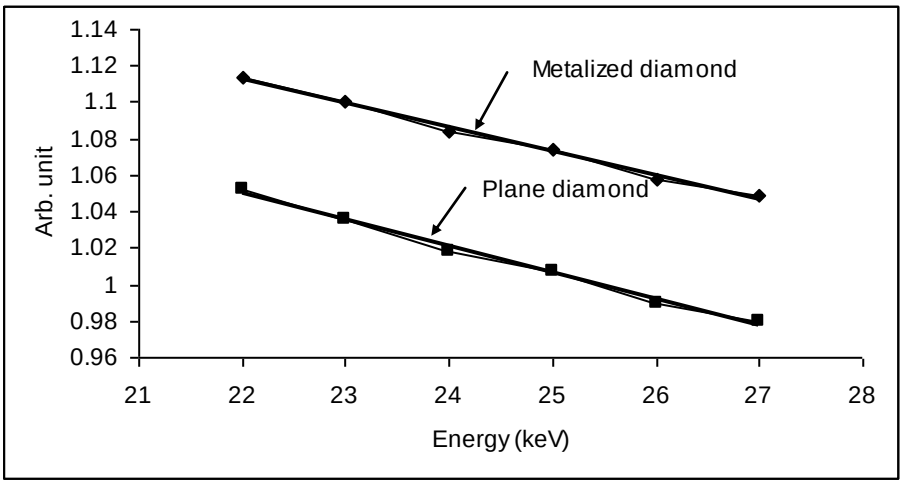


Figure 6.7: Variation of absorbed dose with X-ray peak energy for a Monte Carlo simulation on plane and metalized diamond

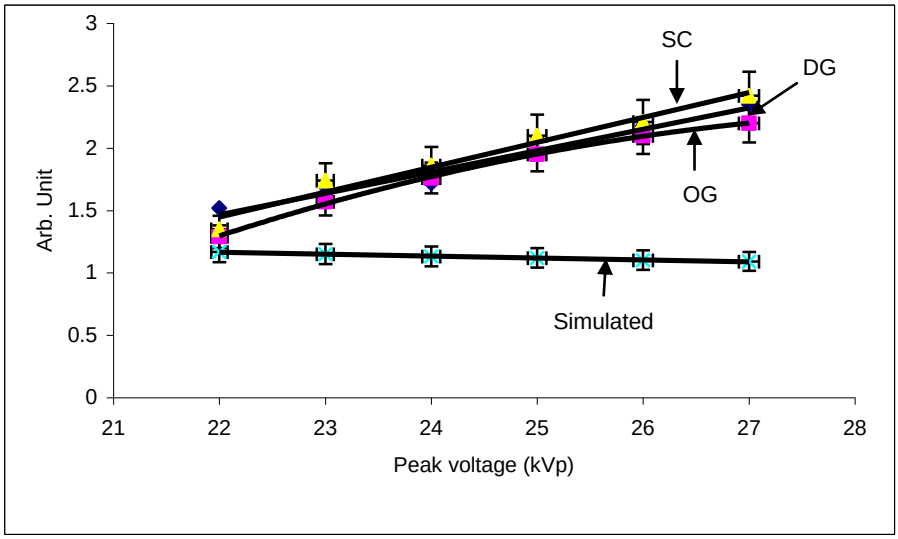


Figure 6.8: Comparison of actual responses with peak voltage for SC, DG, and OG at 200v bias with that of a simulated response for a pure diamond using Monte Carlo Code PENELOPE

6.8 Conclusions

The general observation of the results is that the CVD diamond response saturates with increase peak voltage. The behavioral trend of CVD diamond detectors to X-ray is related to the defects and impurities as discussed in Chapter 5. Comparison of the results of measured deposited energy in CVD diamond detector with the energy deposited on simulated pure diamond using PENELOPE, showed different trends with increase peak voltage that could be related to concentration of impurity/defect in the detectors. The difference in Detector Grade can also be related to their different performance, not only in sensitivity but also the linearity as observed with the detector grades and single crystal CVD diamond wafers, and in comparison with the simulated pure diamond performing negatively to mammography X-rays.

6.9 References

Assiamah M 2004**.** *PhD thesis. University of the Witwatersrand, Johannesburg, South Africa, 87*

Baró J, Sempau J, Fernández-Varea JM and Salvat F 1995. *Methods Phys. Res.* **B 100** 31

Basyigit C, Akkurt I, Kilincarslan S and Akkurt A 2005. *J. Radiol. Prot.* **25** 189

Berger MJ 1963. *Methods in Computational Physics,* **vol.1**, Academic Press, New York 135

Bielajew AF, Hirayama H, Nelson WR and Rogers DWO 1994. *National Research Council of Canada, Report* ***PIRS****-0436*

Briesmeister JF 1993. *Alamos National Laboratory Report* ***LA-12625-M*** *(los Alamos, NM)*

Dance DR 1980. *Phys.Med. Biol.* **25** 25

Doi K and Heang-Ping C 1980. *Radiology* **135** 199

Halbeib JA, Kensek RP, Mehlhorn TA, Valdez GD, Seltzer SM and Berger MJ 1992. *Sandia Report* **SAND9** 1-1634

Halbleib JA 1989. *ITS code system in T. Jenkins, Nelson W; Rindi A; Nahum A and Rogers D. New York: Plenum Press,* 249

James F 1980. *Rep. Prog. Phys*. **43** 1145

Kalos MH and Whitlock PA 1986. *Monte Calo Methods* ***vol. 1*** (Wiley, New York)

Kramer R, Drexler G, Petoussi-Henss N, Zankl M, Regulla D and Panzer W (2001). Phys.Med. Biol. **46** 771

Nelson WR, Hirayama H and Rogers DWO 1985. *The EGS4 Code System Report SLAC-265, Stanford Linear Accelerator Centor, Stanford, California.*

Rubinstein RY 1981. *Simulation and the Monte Carlo Method (*Wiley, New York)

Salvat F 2003**.** *Phys.Rev.***A68** 012708

Salvat F, Fernadez-Verea JM, Baro J and Sempau J 1996. *Ciemat Technical Report No. 799*

Salvat F, Fernández-Varea JM, Acosta E and Sempau J 2001. *PENELOPE-A CODE SYSTEM FOR Monte Carlo Simulation of electron and photon transport. Workshop Proceedings Issy-les-Moulineaux, France 5-7 November.*

Sempau J, Acosta E, Baró J, Fernández-Varea JM and Savat F 1997. *Nucl. Instrum. Methods Phys. Res.* **B 132** 377

Chapter 7

GENERAL CONCLUSIONS

7.0 General conclusions

In this study the effectiveness of electron spin resonance (ESR), ultra-violet (UV) absorption, Raman broadening and thermo-luminescence (TL) emission as tools for performance evaluation of polycrystalline and single crystal CVD diamonds in radiation detection were analyzed.

A review of the CVD diamond detectors is presented in Chapter 1; starting from the historic development of detectors, their use in different fields of science, to highlighting the advantages of diamond detectors in such fields as mammography. As the performance of diamond varies with the synthesis process there is need for having a set of effective characterization tools. Such tools must be capable of distinguishing materials best suited for each application e.g. those that are suitable for dosimetry versus those that are suitable for spectroscopy when exposed to such different sources of radiation as alpha particles or low energy mammography X-rays.

The study showed that both single substitutional nitrogen concentration and the interstitial nitrogen concentration played a significant role in the performance of CVD diamond materials when used as radiation detectors. The presence of single substitutional nitrogen concentration as determined by ESR technique and the presence of grain boundaries as measured by Raman broadening were analyzed and correlated with the absorption of UV and TL respectively in different CVD diamond materials. The study has shown aside from the lower TL values that the values for single substitutional nitrogen concentrations, UV absorption and Raman broadening were higher in the

Optical Grade CVD diamond. The study has further shown that relatively higher single substitutional nitrogen concentration, the higher UV absorption values and higher Raman broadening in Optical Grade CVD diamond wafers could be related to their better performance as alpha detectors whilst lower ESR, lower UV absorption, and higher TL emission values as well as lower Raman broadening could be related to the better performances of both Detector Grade and Single Crystal CVD diamonds when used for alpha spectroscopy i.e. better energy peak efficiencies and energy peak resolutions in the Detector Grade and Single Crystal CVD diamond detectors, were observed.

Chapter 3 presents the background subtraction methods and techniques that were used for α-spectra analyses.

In Chapter 4, the background subtraction methods developed by Fewell et al. (1977) and Seelentag et al. (1979) were extended to cover the range (12keV to 81keV) not included in the earlier publications. The adopted methodology provided corrected spectra that were independent of the detector type when exposed to the mammographic X-ray beam. As the simulated spectrum obtained using the Monte Carlo code PENELOPE corresponded with the measured and corrected spectra it was used to evaluate the performance of a pure diamond material when exposed to X-rays.

In Chapter 5, the performances of the polycrystalline and Single Crystal CVD diamonds when exposed to mammography X-rays were evaluated. The effect of changes to bias voltages on the current leakage was performed. Of note is the higher impendence of

Single Crystal and Detector Grade CVD diamonds when compared to that of the Optical Grade CVD diamond.

In general the detector response to X-rays was observed to increase with the increase in bias voltage for the diamond types evaluated. Saturation in X-ray responses to peak voltage variations were observed for the Optical Grade CVD diamonds. Both Single Crystal and the Detector Grade CVD wafers have X-ray responses that were higher than that of the Optical Grade CVD wafers. It was further found that lower single substitutional nitrogen concentration, lower UV absorption and higher TL emission values as well as lower Raman broadening correlated with higher X-ray response. The sensitivities of the detectors saturated with increase in single substitutional nitrogen concentration, bias voltage and UV absorption for both CVD diamond types.

In Chapter 6, based on the good correlation obtained for both experimental and simulated results in Chapter 4, the Monte Carlo (PENELOPE) code was subsequently used to substantiate the observed implied role impurities have on the response of CVD diamond wafers to X-ray energies.

It can be concluded the research has provided a set of evaluation techniques for use in selecting and narrowing the choice of CVD detector material that can be used for radiation detection. In particular for alpha detection the preferred material ought to be from the Optical Grade CVD diamond; suitably selected Detector Grade CVD diamond can be used as an effective alpha spectrometer as would be from the Single Crystal CVD

diamond. The detection of X-ray photons is best obtained using a Detector Grade CVD diamond wafers, but generally the most consistent radiation detector is seen in the use of Single Crystal wafers.

7.1 Suggestion for future work

An investigation into a possible use of CVD diamond as X-ray spectrometer for low energy X-rays in the mammographic energy range is suggested as an area for further research. The observed linearity and sensitivity of the Detector Grade and Single Crystal CVD diamond to low energy mammography X-rays hint at their possible use in X-ray spectroscopy.

The limitations of the MC code (PENELOPE) with regard to the study of a detector under the application of electric field across opposite surfaces coupled with the presence of added impurities to detector matrix, prevented an exact modeling of the research under taken. An improvement in the Code could make it an invaluable validatory and design tool if all such parameters (electric field, voltage and impurity concentrations) could be taken into account as this study has shown their presence affect the simulation of actual experiment.

Appendices

Appendix 1

1.1 PUBLICATIONS

RD Mavunda, YI Zakari, TL Nam and RJ Keddy 2008. Evaluation of observed variation in CVD diamond detector response with crystal defects at low energy mammographic X-rays. Submitted to the journal: *Applied Radiation and Isotopes*.

RD Mavunda, YI Zakari, TL Nam and RJ Keddy 2008. The presence of defects and their influence on the performance of CVD diamond as an α-particle radiation sensing element. *Applied Radiation and Isotopes*. In press

RD Mavunda, M Assiamah, TL Nam and RJ Keddy 2004. Bremsstrahlung spectra from diagnostic X-rays. *Radiation Physics and Chemistry* **71** 991.

M Assiamah**, RD Mavunda,** TL Nam and RJ Keddy 2003. Effect of pressure, temperature and humidity in air on photon fluence and air kerma values at photon energies. *Radiation Physics and Chemistry* **68** 707-720.

M Assiamah**, RD Mavunda,** TL Nam and RJ Keddy. 2003. Segmented multifit of polynomial function for mass attenuation and energy-absorption coefficient values. *Radiation Physics and Chemistry* **67** 1.

1.2 CONFERENCES

RD Mavunda, YI Zakari, TL. Nam and R.J Keddy. The presence of defects and their influence on the performance of CVD diamond when used as radiation sensing element. 4th SAIP conference 2007. Jahannesburg.

RD Mavunda, TL Nam and RJ Keddy 2004. Stripping of low energy brehmsstralung spectrum. 44th Annual Congress of the South African Association of Physicists in Medicine and Biology. Johannesburg.

RD Mavunda, M Assiamah, TL. Nam and RJ. Keddy 2003. Bremsstrahlung Spectra from Diagnostic X-rays. International symposium on radiation physics-9. Cape Town.

RD Mavunda, M Assiamah, TL Nam and RJ Keddy 2002. X-ray spectral measurement within mammography energy range for dose calculation. 42nd Annual Congress of the South African Association of Physicists in Medicine and Biology.

Appendix 2

LIST AND DESCRIPTION OF DIAMOND SAMPLES

The list of diamond samples used for the study

Name	DG1
Type[1]:	Synthetic, polycrystalline
Dimension:	5 x 5 mm^2
Mass:	9.31±0.02mg
Thickness[2]:	1±0.01 mm
Nitrogen[3]:	3.5 ±0.01 ppm
Contact:	Platinum, titanium and gold on opposing surfaces
Quality[4]:	good
Comments:	no space charge effect needs no pre-irradiation

[1] Type indicates diamond type of the product
[2] Thickness refers to the distance between the polished surfaces of the diamond sample
[3] Nitrogen concentration present in samples
[4] Quality refers to % non-diamond

Name	DG2
Type:	Synthetic, polycrystalline
Dimension:	5 x 5 mm^2
Mass:	9.06±0.02 mg
Thickness:	1±0.01 mm
Nitrogen:	4.0 ±0.01 ppm
Contact:	Platinum, titanium and gold on opposing surfaces
Quality	good
Comments:	no space charge effect needs no pre-irradiation

Name	DG3
Type:	Synthetic, polycrystalline
Dimension:	5 x 5 mm^2
Mass:	8.59±0.02 mg
Thickness:	1±0.01 mm
Nitrogen:	5.0 ±0.01 ppm
Contact:	Platinum, titanium and gold on opposing surfaces
Quality	good
Comments:	no space charge effect needs no pre-irradiation

Name	DG4
Type:	Synthetic, polycrystalline
Dimension:	5 x 5 mm^2
Mass:	8.46±0.02 mg
Thickness:	1±0.01 mm
Nitrogen:	5.3 ±0.01 ppm
Contact:	Platinum, titanium and gold on opposing surfaces
Quality	good
Comments:	no space charge effect needs no pre-irradiation

Name	OG1
Type:	Synthetic, polycrystalline
Dimension:	5 x 5 mm^2
Mass:	9.25±0.02 mg
Thickness:	1±0.01 mm
Nitrogen:	42.9 ±0.01 ppm
Contact:	Platinum, titanium and gold on opposing surfaces
Quality	good
Comments:	no space charge effect needs no pre-irradiation

Name	OG2
Type:	Synthetic, polycrystalline
Dimension:	5 x 5 mm^2
Mass:	8.31±0.02 mg
Thickness:	1±0.01 mm
Nitrogen:	71.0 ±0.01 ppm
Contact:	Platinum, titanium and gold on opposing surfaces
Quality	good
Comments:	no space charge effect needs no pre-irradiation

Name	OG3
Type:	Synthetic, polycrystalline
Dimension:	5 x 5 mm^2
Mass:	9.22±0.02 mg
Thickness:	1±0.01 mm
Nitrogen:	53.6 ±0.01 ppm
Contact:	Platinum, titanium and gold on opposing surfaces
Quality	good
Comments:	no space charge effect needs no pre-irradiation

Name	OG4
Type:	Synthetic, polycrystalline
Dimension:	5 x 5 mm^2
Mass:	8.67±0.02 mg
Thickness:	1±0.01 mm
Nitrogen:	62.5 ±0.01 ppm
Contact:	Platinum, titanium and gold on opposing surfaces
Quality	good
Comments:	no space charge effect needs no pre-irradiation

Name	SC
Type:	Synthetic, polycrystalline
Dimension:	5 x 5 mm^2
Mass:	35.4±0.01 mg
Thickness:	0.5±0.001 mm
Nitrogen:	<1 ±0.001 ppm
Contact:	Platinum, titanium and gold on opposing surfaces
Quality	good
Comments:	no space charge effect needs no pre-irradiation

Appendix 3

PUBLISHED ARTICLES

Available online at www.sciencedirect.com
SCIENCE DIRECT®
Radiation Physics and Chemistry 71 (2004) 991–992
Radiation Physics and Chemistry
www.elsevier.com/locate/radphyschem

Bremsstrahlung spectra from diagnostic X-rays

R.D. Mavunda*, M. Assiamah, T.L. Nam, R.J. Keddy

Health Physics Service, Schonland Research Institute for Nuclear Sciences, University of the Witwatersrand, Private Bag 3, PO Wits 2050, Johannesburg, South Africa

1. Introduction

In this paper X-ray spectra from Mo and W anode tubes, obtained with voltages up to 95 kV, were analysed. Corrections for detector window K-escape, Compton scattering and inefficient photon absorption were applied. A combination of stripping techniques was used. A comparison of the corrected spectra from molybdenum and tungsten targets with computed spectra obtained using the PENELOPE Monte Carlo simulation code is made.

2. Experimental setup

The spectral measurements were obtained using a liquid nitrogen cooled, high purity, intrinsic planar germanium detector with an operating bias of −2500 V. A microprocessor-based system with 4096 channel background memory for buffer storage was used for the spectrum analysis. For data acquisition the spectrum was set to operate in the multi-scaling mode. Calibration reference sources were placed 50 cm from the detector and a preset time of 3600 s was used for the calibration of the detector system. For the X-ray beam analysis the germanium detector was placed 65 cm from a SENOGRAPHE 500 T molybdenum mammography unit and a prototype tungsten target unit.

3. Detector calibration and data analysis

The detector was calibrated for energy scales, linearity, resolution and full energy peak efficiency using ^{241}Am, ^{57}Co and ^{133}Ba radioactive sources and the measured intensities were corrected for detector efficiency. The spectra were also corrected for Compton scatter, employing the method suggested by Seelentag and Panzer (1979). The true photon intensity, I_0, with energy, E, incident on the detector was calculated from the measured photon intensity, I_E, at energy, E, after the two corrections (Fewell and Shuping, 1977; Seelentag and Panzer, 1979) using Eq. (1):

$$I_0 = \left[I_E - \left(f_{E+E_K} I_{E+E_K} + \sum_{E=E_c}^{E_{max}} C_h(E) I_t(E) \right) \right] / (1 - f_E), \quad (1)$$

where E_c is the Compton edge energy

$$(E_c = 2 \times E_0^2 / (2 \times E_0 + 511)). \quad (2)$$

In Eq. (2) E_0 is the incident photon energy in keV, f_E is the K-escape peak ratio at energy E, $f_E I_0$ is the intensity lost due to escape, f_{E+E_K} is the escape peak ratio at energy $E + E_K$ and $f_{E+E_K} I_{E+E_K}$ is the intensity gained by escape from a higher energy $E + E_K$. (E_K is the weighted average energy of the Ge fluorescent X-rays, 10 keV (Israel et al., 1971)). $C_h(E)$ is the Compton background correction factor, $I_t(E)$ is the sum of the counts in the true photon contribution. The denominator of Eq. (1) is the full energy peak efficiency of the detector. Data on X-ray properties of germanium however, indicated that the fluorescent yield of K_β X-rays is negligible (Bertin, 1978), implying therefore that all the K-escape fluorescent is due to the K_α component; correction using only existing data for the K-escape fraction was therefore adopted.

4. Results and discussion

Fig. 1 presents the normalized detector efficiency for the measured energy range 11.1–81 keV. The efficiency

*Corresponding author. Tel.: +27-11-717-6930; fax: +27-11-717-6932.
E-mail address: Mavunda@src.wits.ac.za (R.D. Mavunda).

0969-806X/$ - see front matter © 2004 Elsevier Ltd. All rights reserved.
doi:10.1016/j.radphyschem.2004.05.015

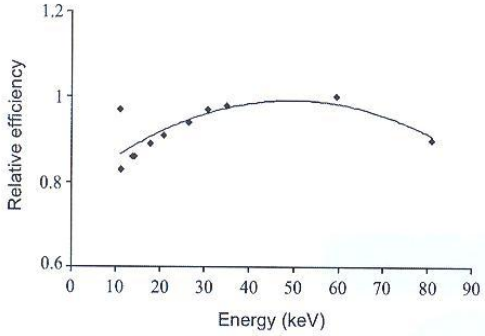


Fig. 1. Germanium detector efficiency is demonstrated after correction for attenuation by air, aluminium, beryllium window and rhodium matrix of $^{57}Co_7$ reference source. Superimposed is the second-degree polynomial equation fitted to the data. The regression equation is $Y = -8 \times 10^{-5}x^2 + 8.4 \times 10^{-3}x + 0.7838$.

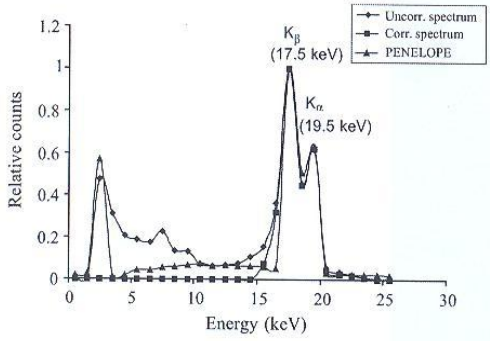


Fig. 2. Corrected and uncorrected molybdenum spectra obtained from the measured data and a Monte Carlo simulated molybdenum spectrum.

was determined after correction for attenuation by air, aluminium, beryllium window and rhodium matrix of the ^{57}Co reference source. The detector efficiency curve for the detector used as depicted in Fig. 1 correlates well with that published by Fewell and Shuping (1977). Corrected and uncorrected molybdenum and tungsten spectra are shown in Figs. 2 and 3, respectively. In both

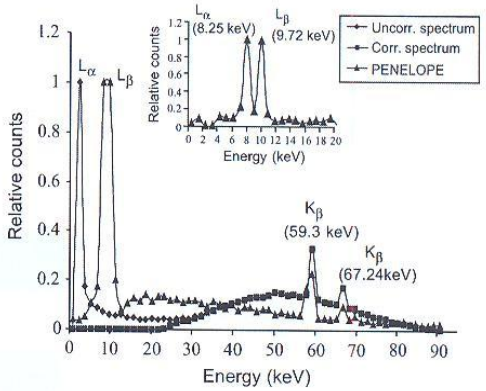


Fig. 3. The corrected and uncorrected tungsten spectra obtained from measured data and a Monte Carlo simulated tungsten spectrum. Inset is the PENELOPE Monte Carlo computation to 20 keV.

these figures the characteristic K_α and K_β X-rays are well separated. The characteristic X-rays spectra correlate well with the published results (Figs. 2 and 3) and with the simulated spectra obtained from the PENELOPE Monte Carlo code (Sempau et al., 1997).

References

Bertin, E., 1978. Principles and Practice of X-ray Spectral Analysis. Plenum Press, New York.

Fewell, T.L., Shuping, R.E., 1977. Photon energy distribution of some typical diagnostic X-ray beam. Med. Phys. 4 (3), 187–197.

Israel, H.I., Lier, D.W., Storm, E., 1971. Comparison of detectors used in measurement of 10–300 keV X-ray spectra. Nucl. Instrum. Methods 91, 141–157.

Seelentag, W.W., Panzer, W., 1979. Stripping of X-ray Bremsstrahlung Spectra up to 300 kVp on a desk type computer. Phys. Med. Biol. 24 (4), 767–780.

Sempau, J., Acosta, E., Baro, J., Fernandez-Varea, J.M., Salvat, F., 1997. An algorithm for Monte Carlo simulation of coupled electron-photon transport. Nucl. Instrum. Methods B132, 377–390.

ARTICLE IN PRESS

Available online at www.sciencedirect.com

ScienceDirect

Applied Radiation and Isotopes ▮ (▮▮▮▮) ▮▮▮–▮▮▮

Applied Radiation and Isotopes

www.elsevier.com/locate/apradiso

The presence of defects and their influence on the performance of CVD diamond as an α-particle radiation sensing element

R.D. Mavunda[a], Y.I. Zakari[b], T.L. Nam[a,*], R.J. Keddy[a]

[a]*Radiation and Health Physics Unit, DST/NRF Centre of Excellence in Strong Materials and the School of Physics, University of the Witwatersrand, Private Bag 3, PO Wits 2050, Johannesburg, Republic of South Africa*

[b]*Ahmadu Bello University, Zaria, Nigeria*

Received 2 November 2007; received in revised form 19 December 2007; accepted 1 January 2008

Abstract

Three types of diamonds produced by chemical vapor deposition (CVD) and broadly classified as detector grade, optical grade and single crystal were evaluated in terms of their response to α-particle radiation when used as detection elements. It is well known that the presence of defects in diamond, including CVD specimens, not only dictates but also affects the response of diamond to radiation in different ways. In this investigation, tools such as electron spin resonance (ESR), thermo-luminescence (TL), Raman spectroscopy and ultraviolet (UV) spectroscopy were used to probe each of the samples, which were then graded on their performance as α-particle radiation detectors. The presentation discusses the presence of defects identifiable by the techniques used and correlates the radiation performances of the three types of crystals to their presence.

© 2008 Elsevier Ltd. All rights reserved.

Keywords: A-spectroscopy; CVD diamond characterization; Particle radiation detectors

1. Introduction

Recent advances in homoepitaxial synthesis of a single crystal-diamond have invigorated the already growing interest in chemical vapor deposition (CVD) diamond crystal for use as a radiation probe. In general, epitaxy, on foreign substrates, leads to a polycrystalline diamond with detector and optical properties of grain boundaries that precludes its use in some of the desired applications. Some progress has been made in recent years in growing CVD diamond on iridium (Schreck et al., 2001).

Single-crystal CVD diamond with the reported carrier transport properties (Isberg et al., 2002) could surpass other wide band gap materials for power and high-frequency electronics application. The electronics and optical properties of CVD diamonds are determined by intrinsic defects and extrinsic contaminants or dopants, most prominently nitrogen, silicon, boron and phosphorus, as well as different structural morphologies (Davies, 1999).

The nominally un-doped polycrystalline CVD diamond has characteristics of both electrons and holes, contributing to transient photocurrents. The combined charge mobility (electrical behavior) depends on the film quality, carrier density, grain size, higher growth temperature and purity of the diamond film (Nebel, 2003). The life-time of photo-generated carriers in the conduction and valence bands is short, with a time constant in the range 340–550 ps. Based on these parameters, a trap density of $10^{17}\,cm^{-3}$ was realized as the density of trapping centers most likely present in grain boundaries (Nebel, 2003). Grain boundaries are believed to act as charge trapping and recombination centers in polycrystalline CVD diamond (Manfredotti et al., 1996), but absent in single-crystal CVD diamond (Hammersberg et al., 2001; Sellin et al., 2007). The interaction of photon-generated carriers with traps and defects in the band gap of diamond has been investigated. When an electric field is applied to a semiconductor exposed to radiation, the electron–hole pair generated separates and drifts towards opposite electrodes. Charge trapping and recombination may however prevent some carriers from being collected by the electrodes (Hecht,

*Corresponding author. Tel.: +27 1171 76931; fax: +27 1171 76937.
E-mail address: tom.nam@wits.ac.za (T.L. Nam).

0969-8043/$ - see front matter © 2008 Elsevier Ltd. All rights reserved.
doi:10.1016/j.apradiso.2008.01.006

Please cite this article as: Mavunda, R.D., et al., The presence of defects and their influence on the performance of CVD diamond as an α-particle radiation sensing element. Appl. Radiat. Isotopes (2008), doi:10.1016/j.apradiso.2008.01.006

1932; Gerrish, 1995; Sciortino, 1999). The interstitial nitrogen, which is non-bonded to CVD diamond crystal, exhibits a very low activation barrier and may diffuse out of the bulk at low temperatures (Kuo et al., 2001).

High-pressure/high-temperature (HPHT) diamond with single substitutional nitrogen (N_s) has a recombination efficiency which compromises the response (Nam, 1989). However, high N_s concentration was also observed to lower the electron trap levels when compared with specimens synthesized with lower N_s concentrations (Nam et al., 1991). Whilst the concentration of N_s can be accurately determined by electron spin resonance (ESR), nitrogen complexes are normally determined by ultraviolet (UV) absorption (Davies, 1999; Nam et al., 1991). Kuo et al. (2000) have shown that incorporation of nitrogen leads to a chemical shift and a reduction in Raman peak intensity. UV visible absorption results show that, compared to undoped film, nitrogen-doped films have a higher relative intensity of UV absorption (Kuo et al., 2001). Thermoluminescence (TL) occurs in crystal due to the radiative recombination of previously trapped charge carriers, at luminescence centers. The larger the concentration of these centers, the higher the TL yield. A large number of solids exhibit the presence of centers with which carriers can only recombine non-radiatively (Araikum, 1993), in this case N_s centre. The TL is mainly dominated at the broad (~0.5 eV width) signal referred to as band-A emission (Iakoubovskii and Stesmans, 2002), which is generated via strain-induced broadening from a vibronic side band. Band-A type luminescence originates either from the dislocation or from boron-related impurities (Ruan et al., 1992). The TL is explained by the donor–acceptor (DA) pair recombination model (Dean, 1965).

In this work the characteristics of nine CVD diamond samples classified as electrical grade, optical grade and single crystal were analyzed for use as a radiation probe. These CVD diamond samples were characterized to obtain information about their levels of impurities including nitrogen and consequently to establish the material quality.

The tool commonly used in diamond characterization is ESR, which enables the identification of the concentrations of N_s, hydrogen and other impurities (Nebel, 2003). Ns–V–Ns complexes could be from the aggregation of single nitrogen atoms or N_2 incorporation, followed by the capture of a vacancy. The aggregation is temperature activated and depends on the crystal orientation (Doverspike et al., 1993; Lin et al., 1996; Snail et al., 1992; and Taylor et al., 1996). UV spectroscopy can be used to identify the diamonds with such nitrogen complexes and the nearest neighbor nitrogen substitutional forms $(N_s–N_s)^o$ (Davies, 1999; Iakoubovskii et al., 2000). The UV absorption is associated mainly with the planar $\langle 1\,0\,0 \rangle$ defects of unknown structure, which are determined by a high-resolution microscope as observed by Wight et al. (1971). In UV measurements the dipole moments of the molecules change due to absorption of light of certain energies, and the transition occurs due to the absorption of UV radiation, which happens if the transition integral is nonzero (Herzberg, 1945). Raman spectroscopy was used to identify the purity of diamond material, to establish how much stress/strain the CVD diamond material was under, and the orientation of the crystal of the material, i.e., polarization of the scattered light in the material (e.g. crystallinity of the CVD diamond) (Herzberg, 1945).

It is a well-known fact that defects in diamond, including CVD specimens, affect the response of the diamond to radiation in different ways. The research undertaken was aimed at correlating the α-particle radiation detection performance characteristics of CVD diamonds to the defects identified by the above-mentioned tools.

2. Experimental

Information about the level and types of impurities, especially nitrogen, was sourced for different grades of CVD diamonds identified by the supplier as optical grade samples OG1, OG2, OG3, OG4, detector grade samples DG1, DG2, DG3, DG4, all polycrystalline, and a single crystal (SC) type. Characterization experiments were carried out on all of these samples. The samples were acid cleaned before metallization was carried out with, in order, titanium (strong carbide former), platinum (weak carbide former), and gold (non-carbide former), i.e. Ti/Pt/Au layers, 200 Å:200 Å:2000 Å in thickness, respectively, to form ohmic contacts (Tachibana and Glass, 1993) on the two polished and opposite surfaces of the diamond. The diamonds were all in wafer form and of dimensions $5 \times 5 \times 0.5$ and $5 \times 5 \times 0.1\,mm^3$, for the polycrystalline and single-crystal structures respectively.

Each of the samples from the three classified types was assayed, first, by placing each sample in the magnetic field of a Bruker microwave bridge ESP 380-1010 coupled to a ESP 380-1020 controller and an ESP 300E ESR unit. The N_s concentrations of the diamond samples were measured.

UV measurements were undertaken using a Varian Cary UV–vis–NIR Spectrometer. Each of the samples was beam scanned covering the UV range between 200 and 350 nm and compared with a reference beam for each of the UV values. The relative absorbance values were recorded at an absorption edge of 230 nm.

Raman spectroscopy was conducted using a Jobin-Yvon T64000 Raman spectrometer operated in the single spectrograph mode with an Olympus microscope as micro-Raman attachment. Excitation laser wavelength was 514.5 nm from an argon ion laser. Backscattered light was dispersed via 1800 grooves/mm grating onto a liquid nitrogen-cooled charge collection device (CCD) detector. Laser spot size under the microscope was approximately 1.5 μm in diameter. The vibration in the Raman peaks at $1332\,cm^{-1}$ due to the absorption, transmission and scattering of the light illuminating the samples was measured.

TL measurements were carried out by placing each of the irradiated samples (using Sr-90 with controlled exposure

Please cite this article as: Mavunda, R.D., et al., The presence of defects and their influence on the performance of CVD diamond as an α-particle radiation sensing element. Appl. Radiat. Isotopes (2008), doi:10.1016/j.apradiso.2008.01.006

time) into a TLD reader, model Toledo 654 TLD. The temperature was ramped up to 300 °C for the luminescence emission to be measured. The integrated response from each sample was recorded as arbitrary counts.

Finally, the CVD diamond was placed 2.2 cm from a 3.7×10^6 Bq cm^{-2} Am-241 alpha source for the acquisition of the alpha spectrum using a PC-based commercial software APTEC. The number of α-particles impinging on the surface of the wafer per second was estimated to be 4.84×10^4. The CVD diamond probe with a bias voltage of 100 V, applied across the opposing metallized surfaces, was then connected to a locally designed and manufactured preamplifier, and the whole system, including the alpha source, was placed in a vacuum chamber. The preamplifier was coupled to an oscilloscope for pre-assessment of the signal, and a personal computer with the APTEC software for data acquisition, processing and analysis. The peak value of each spectrum was equated to the alpha energy peak (5.48 MeV) to evaluate the energy per channel for a plot of the calibrated graphs.

3. Results and discussion

General observations of the results summarized in Table 1 indicate a consistent pattern from the different diamond types for most of the methods used. The UV values, N_s concentration, TL values, to some degree the extent of Raman broadening, and values reflecting absolute efficiency results can be separated into three groups, which themselves can be associated with the different grades of detectors investigated as OG, DG and SC. The N_s concentration in the polycrystalline specimens (3.5–71 ppm) is observed to be higher than that observed in the single-crystal specimen (below 1 ppm). The same variation in trend is observed in the UV absorption and Raman spectral broadening of the samples. The different grades of polycrystalline specimens also indicate a difference in their N_s contents, UV absorption and Raman spectral broadening. The optical grade CVD diamond was observed to have higher UV response (3.48–3.86 cm^{-1}) than the detector grade samples (0.51–1.93 cm^{-1}).

The TL response was an exception to the above trend, where the luminescence response of the detector grade was observed to be higher (814–2024 arb. units) than the luminescence response of the optical grade (83–155 arb. units). Higher TL values generally indicate a larger number of charge carriers created by the impinging alpha particles. These charge carriers are available for capture at trapping/luminescence centers and for collection should a field be applied across the detector. The observed improvement in energy resolution of the detector grade, in general, and DG3, in particular, with its relatively better alpha response, can be attributed to their fewer defects and lower N_s concentrations. The overall performance of the single-crystal CVD diamond and the conclusions of Pomorski et al. (2006) support the importance of low defect levels. The single-crystal CVD diamond maintained its comparatively lower response with the TL (25 arb. units) despite a relatively low concentration of N_s centers. This may be attributed to the concomitant low levels of luminescence-related defects in its matrix. It is suggested that the much higher TL values of DG3 reflect not only the availability of charge carriers but also the effectiveness of the capture/release mechanism.

A typical alpha spectrum from the CVD optical grade diamond detector is shown in Fig. 1. Depicted in the figure are the spectra before and after background subtraction. A software package ORIGIN (6.1) was used for both baseline insertion and background subtraction. The spectrum of each of the nine CVD diamond detectors was analyzed for peak resolution, peak efficiency and absolute efficiency.

The alpha spectrum analysis observed with the full-width half-maximum (FWHM) value $\Delta E/E$, where ΔE is the spectrum width at half the maximum ordinate of the peak value and E is the value of the alpha spectral peak (5.484 MeV), was calculated. The energy resolution ΔE of the detector's spectrum is an indicator of the quality of the detector material, as it reflects the impurity and homogeneity of the crystal structure and is strongly related to the carrier life-time and thus the charge collection efficiency (Pomorski et al., 2006). The single crystal was observed to have FWHM of 85.3 ± 0.9 keV when compared with the

Table 1

Sample	Raman spectral broadening FWHM (cm^{-1})	TL response (arbt.unit)	ESR: single substitution nitrogen (ppm)	UV absorption (cm^{-1})	Total alpha counts (cps)	Absolute efficiency %	Energy peak efficiency %	Alpha FWHM (keV)
DG1	2.64 ± 0.17	1147	3.5	0.51 ± 0.06	32969	68	80	1010.59 ± 27.03
DG2	2.57 ± 0.17	881	4	1.93 ± 0.13	31327	65	80	693.41 ± 11.16
DG3	2.63 ± 0.15	2024	5	1.03 ± 0.08	29834	62	81	64.14 ± 0.8
DG4	2.55 ± 0.16	814	5.3	1.9 ± 0.05	32732	68	80	672.55 ± 5.46
OG1	2.59 ± 0.15	155	42.9	3.86 ± 0.05	50314	104	60	7465.39 ± 90.4
OG2	2.78 ± 0.24	83	71	3.52 ± 0.09-	49010	101	60	5975.00 ± 34.99
OG3	2.76 ± 0.24	141	53.6	3.48 ± 0.11	49397	103	60	7050.34 ± 124.8
OG4	2.81 ± 0.22	93	62.5	3.59 ± 0.11	39046	81	60	7245.66 ± 60.48
SC	2.32 ± 0.03	25	<1	0.88 ± 0.02	25401	52	80	85.28 ± 0.9

Please cite this article as: Mavunda, R.D., et al., The presence of defects and their influence on the performance of CVD diamond as an α-particle radiation sensing element. Appl. Radiat. Isotopes (2008), doi:10.1016/j.apradiso.2008.01.006

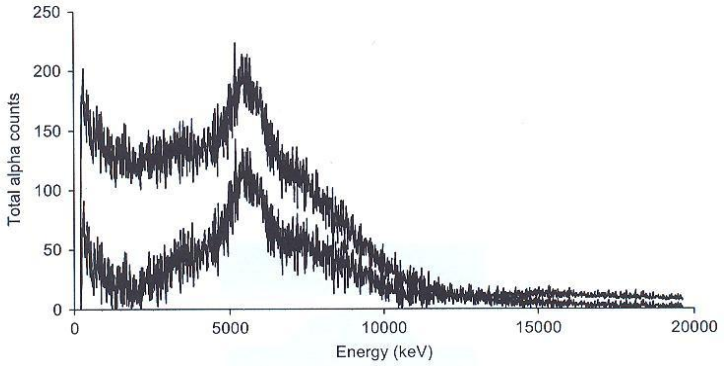


Fig. 1. A typical optical grade CVD diamond spectrum before (upper curve) and after (lower curve) background subtraction.

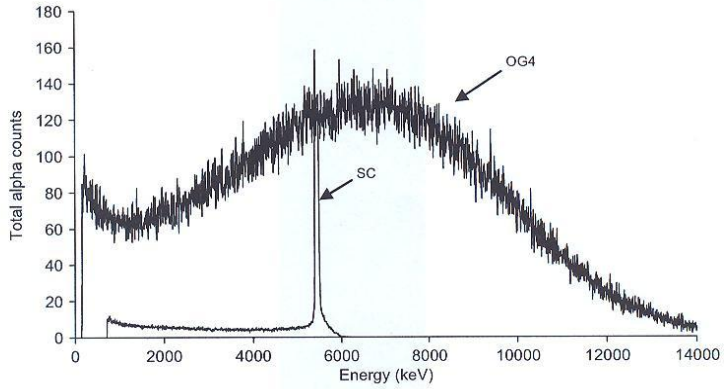


Fig. 2. Alpha spectrum from OG4 polycrystalline and single-crystal (SC) CVD diamond samples showing energy peak.

polycrystalline FWHM of between 672.5 and 7465.9 keV with an exception of one detector grade member, namely DG3 with a FWHM of 64.1 keV. This is as depicted in Fig. 2 for the single crystal and in Fig. 3 for the polycrystalline detector grade CVD diamond DG3. The alpha response of the polycrystalline also shows a difference between the detector grades (Fig. 3) and the optical grades (Fig. 2). The differences in peak resolution could partly be caused by the spread of the electric field along the material due to its polycrystalline nature having non-uniform geometry and thickness (Tromson et al., 2000). It could also be partly due to the capture/release mechanism of trapping levels inducing a space charge build-up of internal electric fields leading to the observed spectral broadening (Souw and Meilunas, 1997). The observed absolute efficiency of all optical grade detectors between 80% to about 100% is consistent with the observed broadening of their peak resolution above 100%, and this, we propose, is a result of the polarization effects causing a build-up (pile-up) of e–h pairs, coupled with the greater thickness (500 μm) of the detectors used (Souw and Meilunas, 1997; Bergonzo et al., 2001; Liechtenstein et al., 2004). This is supported by the observed drifting of the spectrum peak during spectra acquisition. Within the specimen of the optical grade detectors is their comparatively lower charge carrier effect, as observed from their TL response and higher UV absorption effect. The earlier observed better peak resolution of the detector-grade CVD diamonds was also found to be consistent with their energy peak efficiencies of 80%, and also consistent in performance with the single-crystal (80%) CVD diamond (DG3 in particular) as a spectrometer. The absolute efficiency, calculated as the ratio of the total alpha counts from the detectors to the source strength within the area of the active zone, was also used to study the characteristic performance of the CVD diamond detectors. The single crystal had fewer impurities and was least efficient absolutely (52%). The optical grade

Please cite this article as: Mavunda, R.D., et al., The presence of defects and their influence on the performance of CVD diamond as an α-particle radiation sensing element. Appl. Radiat. Isotopes (2008), doi:10.1016/j.apradiso.2008.01.006

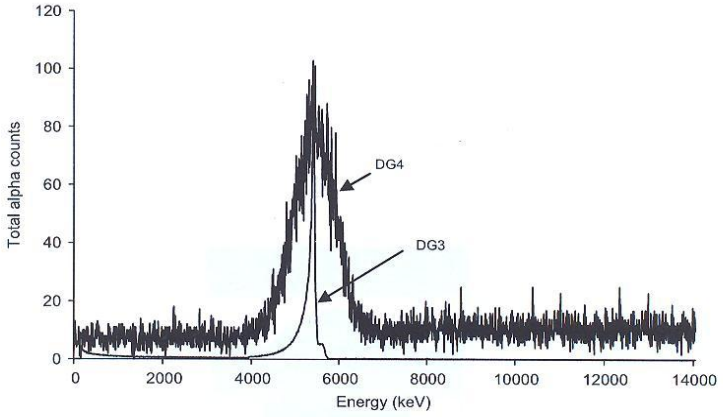


Fig. 3. Alpha spectrum from detector grade DG3 and DG4 CVD diamond samples showing the characteristic energy peak.

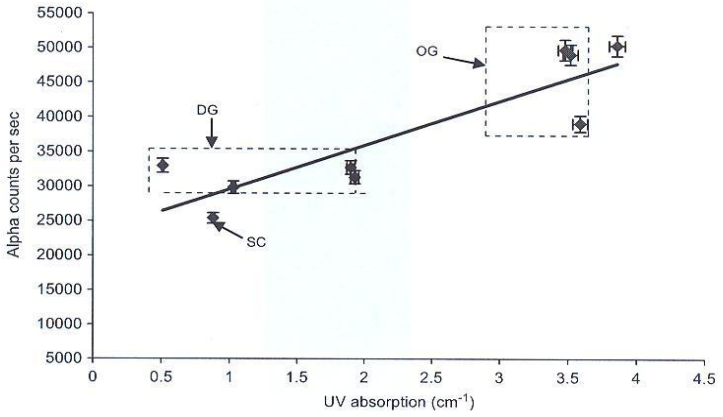


Fig. 4. Variation of total alpha counts with UV absorption for detector and optical grade CVD diamonds.

diamonds, with the relatively higher number of impurities detected by both UV and ESR, indicated a higher efficiency of between 80% to above 100%. This is consistent with the reason for their poor peak resolution as a consequence of polarization effects causing the build-up of internal electric fields. For the detector grades, the absolute efficiency of between 62% and 68% is consistent and is closely related to the single crystal in their performances. Compared to the optical grade CVD, this may be attributed to their lower defect/impurity levels with reduced resulting build-up effects. Of note is the observation that low N_s levels were found to have no significant effect on the carrier life-times (Sellin et al., 2007). In comparison to the OG, the observed lower efficiency of the single crystal (by 48%) may be due to its overall lower defect concentration (Souw and Meilunas, 1997; Bergonzo et al., 2001).

The graphical results depict the correlation of the different methods used, and an examination of the correlation between the results of the Raman broadening, TL and ESR (N_s) and with alpha counts of the CVD diamond film is reported. Fig. 4 indicates a correlation with positive gradient between the UV absorption of the diamond samples and the total alpha counts. The UV absorption of the optical grade CVD diamond was found on the average to be approximately three times greater than that of the detector grade CVD diamonds with absorption at $1.3 \pm 0.69\,\mathrm{cm}^{-1}$. An appreciable amount of non-diamond phase impurities and structural defects (nitrogen complexes or UV-related impurities) that commonly exist in CVD could be ascribed to the different absorption response of diamond to UV absorption (Wang et al., 2005). The Raman broadening due to the defect centers in each of the

Please cite this article as: Mavunda, R.D., et al., The presence of defects and their influence on the performance of CVD diamond as an α-particle radiation sensing element. Appl. Radiat. Isotopes (2008), doi:10.1016/j.apradiso.2008.01.006

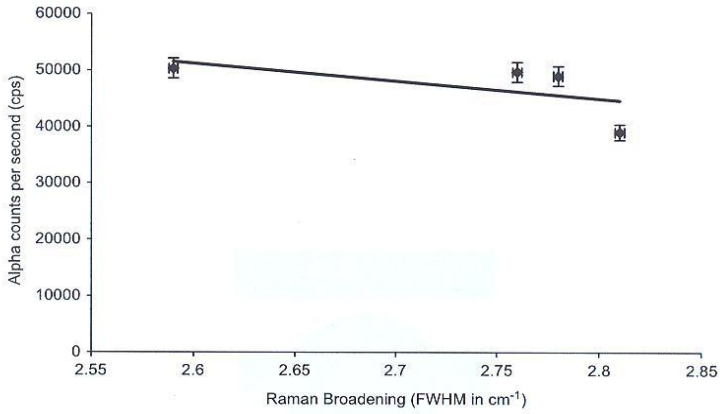


Fig. 5. Variation of total alpha counts with Raman broadening for optical grade CVD diamonds.

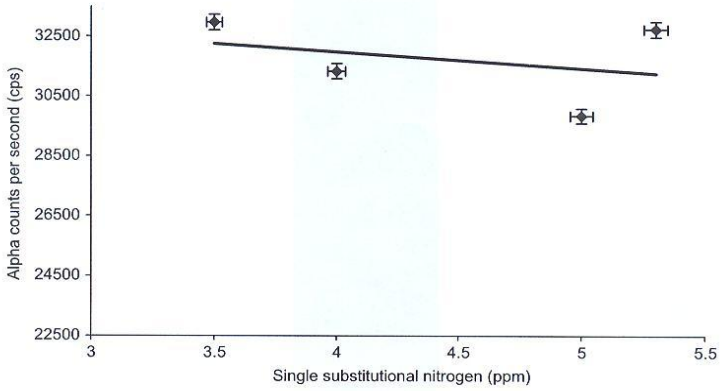


Fig. 6. Variation of total alpha counts with single substitutional nitrogen concentration (using ESR) for detector grade CVD diamonds.

optical grade samples we believe can be related to the alpha response of optical grade CVD diamond detectors. This is shown in Fig. 5, where the observed correlation which appears to be of a negative gradient is observed for the optical grade CVD diamonds. Variation of alpha counts with N_s concentration of detector grade CVD diamond samples is depicted in Fig. 6. The correlation of the alpha count with ESR (N_s concentration) is with a negative gradient. This confirms the general trend of observations by Nam et al. (1991) that, for a class of crystals, the concentration of N_s is inversely related to its response to the impinging radiation. Fig. 7 shows an inverse relationship between N_s centers and UV absorption for the optical grade CVD diamonds, implying therefore the interplaying effect of that extra nitrogen introduced in the synthesis process on the concentration of both the UV-type impurities and N_s centers (Sellin et al., 2007; Souw and Meilunas, 1997). The consequence on the optical grade detectors in particular was the observed higher alpha counts. We were informed that extra nitrogen was added to the optical grade CVD diamond used in this investigation (private communication). Fig. 8 shows a spline-function relation between the N_s concentration and the TL response of the polycrystalline CVD diamonds. Behavior similar to this was also observed by Benabdesselam et al. (2001). Fig. 8 shows that the lower N_s concentrations (ESR) result in higher TL emission. The explanation of a lower TL response of optical grade CVD diamond is however believed to be due to the higher N_s concentration which results in non-radiative recombination, and not the number of trapping levels within the samples (Nam et al., 1991). The model explains the effect of decrease in N_s concentration in diamond to TL response in

Please cite this article as: Mavunda, R.D., et al., The presence of defects and their influence on the performance of CVD diamond as an α-particle radiation sensing element. Appl. Radiat. Isotopes (2008), doi:10.1016/j.apradiso.2008.01.006

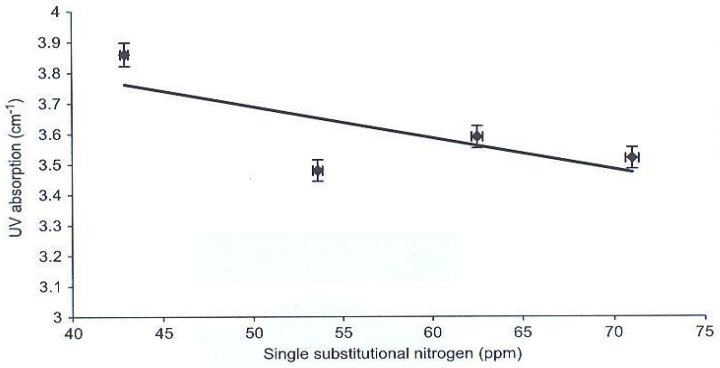


Fig. 7. Variation of UV absorption with single substitutional nitrogen concentration for optical grade CVD diamonds.

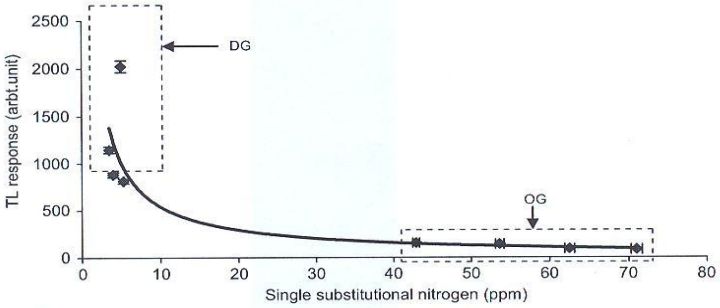


Fig. 8. Variation of thermoluminescence response with single substitutional nitrogen concentration (using ESR) for detector and optical grade CVD diamonds.

relation to other defects, traps and recombination, and the result is observed in this analysis.

The broadening of the spectrum leading to increased FWHM could be attributed to a combination of a more defective crystal lattice (trapping/de-trapping at grain boundaries) and higher concentration of nitrogen complexes (Fish et al., 1999). Fig. 9 is a plot of TL emission in relation to Raman broadening for an optical grade detector, showing that as the Raman effect increases the TL response drops. This may be due to the presence of traps and recombination at grain boundaries. The observed correlation of UV absorption and Raman broadening with FWHM of alpha peaks for all detectors (Figs. 10 and 11) relates to the contributions of the defects associated with the UV absorption and defects giving rise to the Raman broadening and to the relatively larger broadening of the alpha spectra from the optical grade CVD diamonds. This shows the overall effect of the detector with FWHM having a positive gradient to increase the N_s concentration as observed in Fig. 12 and implied in Fig. 7 with a broad spectrum of the optical grade CVD diamond detectors.

4. Summary and conclusions

It is seen that there is a consistent trend of the alpha counts having a positive gradient with UV absorption and TL emission, but a negative gradient to the Raman broadening and N_s concentration. The relatively high total alpha counts from the optical grade CVD diamond may be associated with a greater concentration of UV-related defects and build-up effect. As in the HPHT crystal, N_s in CVD diamonds acts as a recombination center. In general, the higher sensitivity (counting efficiency) is associated with a lower concentration of N_s and hence contributes to the lowering of the alpha counts as observed in the detector grade, optical grade and single-crystal CVD diamonds. For reasonable alpha spectroscopy, our study shows that the value of nitrogen concentration, UV absorption and

Please cite this article as: Mavunda, R.D., et al., The presence of defects and their influence on the performance of CVD diamond as an α-particle radiation sensing element. Appl. Radiat. Isotopes (2008), doi:10.1016/j.apradiso.2008.01.006

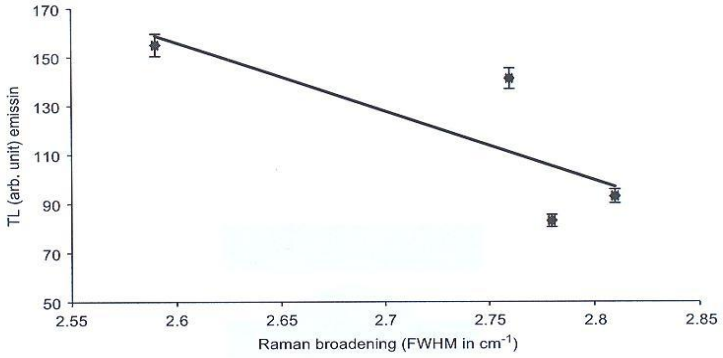


Fig. 9. Variation of TL emission with Raman broadening for optical grade CVD diamonds.

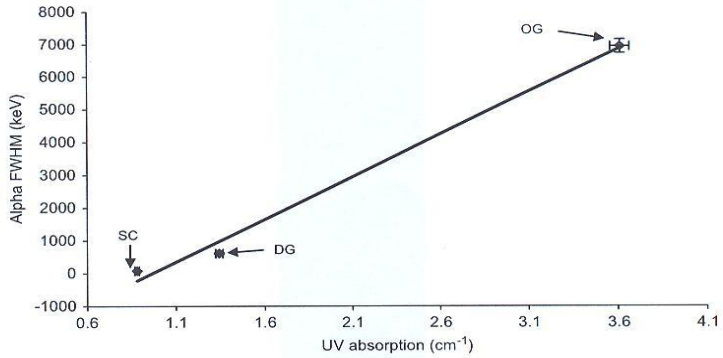


Fig. 10. Variation of FWHM of alpha counts with averaged UV absorption values for both detector and optical grade and single-crystal CVD diamonds.

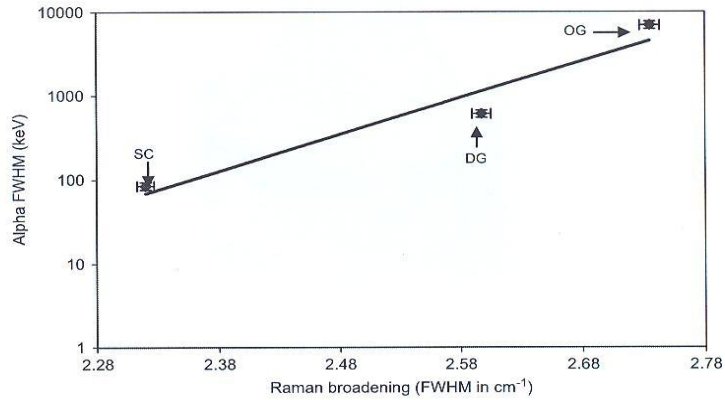


Fig. 11. Variation of FWHM of total alpha counts with averaged Raman broadening values for both detector and optical grade and single-crystal CVD diamonds.

Please cite this article as: Mavunda, R.D., et al., The presence of defects and their influence on the performance of CVD diamond as an α-particle radiation sensing element. Appl. Radiat. Isotopes (2008), doi:10.1016/j.apradiso.2008.01.006

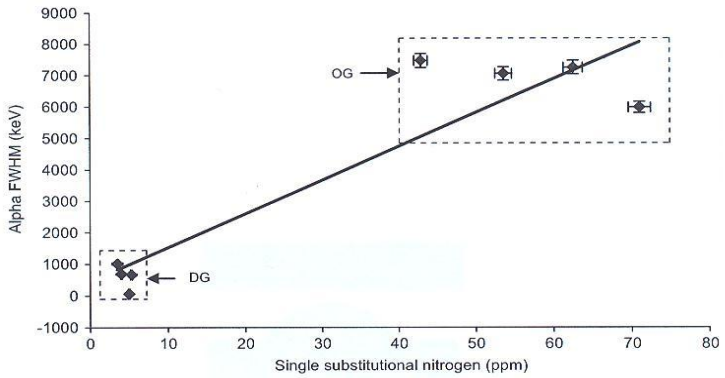


Fig. 12. Variation of alpha FWHM with single substitutional nitrogen concentration for detector and optical grade CVD diamonds.

Raman broadening must be as low as possible, but the TL value must be the highest. In general, the SC grade is the material of choice for general alpha spectroscopy (Pomorski et al., 2006). However, if one wants a detector of higher sensitivity, similar resolution, better peak efficiency and less expensive, selection of CVD materials using TL as a post-selection tool may be the route to take; otherwise, if the interest is not in spectroscopy but in merely a sensitive alpha detector, CVD diamond of the optical grade is a material of choice.

Acknowledgments

The authors would like to extend a special thanks to all the people who assisted this work: Dr. J.A. Van Wyk, for his valuable contributions to ESR studies; Mr. R.B. Erasmus, for the Raman and UV experiments and analysis of the results; Prof. M. Hayes, for making ohmic contacts to the CVD diamond samples; Mr. M. Rebak, for polishing and cleaning the CVD diamond samples; and finally to Mr. Mpho Mofokeng, whose contributions to solving computer-related problems were invaluable.

References

Araikum, S., 1993. Thermally and optically stimulated luminescence in synthetic diamond. Masters Thesis, University of the Witwatersrand, Johannesburg, South Africa.
Benabdesselam, M., Iacconi, P., Butler, J.E., Briand, D., 2001. Diamond Relat. Mater. 10, 2084.
Bergonzo, P., Tromson, D., Mer, C., Guizard, B., Foulon, F., Brambilla, A., 2001. Phys. Stat. Sol. (a) 185 (1), 167.
Davies, G., 1999. Physica B 273, 15.
Dean, P.J., 1965. Phys. Rev. 139, A588.
Doverspike, K., Butler, J.E., Freitas Jr., J.A., 1993. Diamond Relat. Mater. 2, 1078.
Fish, M.L., Massler, O., Reid, JA., MacGregor, R., Comins, J.D., 1999. Diamond Relat. Mater. 8 (8–9), 15114.
Gerrish, V.M., 1995. Semicond. Semimet. 43, 493.
Hammersberg, J., Isberg, J., Johansson, E., Lundström, T., Hjortstam, O., Bernhoff, H., 2001. Diamond Relat. Mater. 10, 574.
Hecht, K., 1932. Z. Phys. (Berlin) 235.
Herzberg, I.G., 1945. Infrared and Raman Spectra of Polyatomic Molecules. Van Nostrand Reinhold, New York.
Iakoubovskii, K., Stesmans, A., 2002. J. Phys.: Condens. Matter 14, R467.
Iakoubovskii, K., Andriaenssens, G.J., Cohra, Y.K., 2000. J. Phys.: Condens. Matter 12, L519.
Isberg, J., Hammersberg, J., Hohansson, E., Wilstrom, T., Twitchen, D.J., Whitehead, AJ., Coe, S.E., Scarsbrook, G.A., 2002. Science 297, 1670.
Kuo, M.T., May, P.W., Gunn, A., Ashford, M.N.R., Wild, R.K., 2000. Diamond Relat. Mater. 9, 1222.
Kuo, M.T., May, P.W., Ashford, M.N.R., 2001. Diamond Relat. Mater. 10, 889.
Liechtenstein, V.Kh., Eremin, N.V., Golser, R., Kutschera, W., Paskhalov, A.A., Priller, A., Steier, P., Vockenhuber, C., Winkler, S., 2004. Nucl. Instrum. Methods Phys. Res. A 521, 203.
Lin, L.T.S., Popovici, G., Mori, Y., et al., 1996. Diamond Relat. Mater. 5, 1236.
Manfredotti, C., Fizzotti, F., Polesello, P., Vittone, E., Wang, F., 1996. Phys. Stat. Sol. 154, 327.
Nam, T.L., 1989. Nuclear radiation detection properties of diamond. Ph.D Thesis, University of the Witwatersrand, Johannesburg, South Africa.
Nam, T.L., Karfunkel, U., Keddy, R.J., Every, A.G., 1991. Radiat. Eff. Defects Solids 116, 233.
Nebel, C.E., 2003. Semicond. Sci. Technol. 18, S1.
Pomorski, M., Berdermann, E., Caragheopol, A., Ciobanu, M., Kiš, M., Martemiyanov, A., Nebel, C., Moritz, P., 2006. Phys. Stat. Sol. (a) 203 (12), 3152.
Ruan, J., Kobashi, K., Choyke, W.J., 1992. Appl. Phys. Lett. 60 (25), 3138.
Schreck, M., Hörmann, F., Roll, H., Lindner, J.K.N., Stritzker, B., 2001. Appl. Phys. Lett. 78 (2), 192.
Sciortino, S., 1999. Riv. Nuovo Cimento 22, 1.
Sellin, P.J., Lohstroh, A., Davies, A.W., Galbiati, A., Parkin, J., Wang, S.G., Simon, A., 2007. Nucl. Instrum. Methods Phys. Res. B 260, 293.
Snail, K.A., Vold, C.L., Marks, C.M., Freitas Jr., J.A., 1992. Diamond Relat. Mater. 1, 180.
Souw, E.K., Meilunas, 1997. Nucl. Instrum. Methods Phys. Res. A 400, 69.
Tachibana, T., Glass, J.T., 1993. Diamond Relat. Mater. 2, 963.

Please cite this article as: Mavunda, R.D., et al., The presence of defects and their influence on the performance of CVD diamond as an α-particle radiation sensing element. Appl. Radiat. Isotopes (2008), doi:10.1016/j.apradiso.2008.01.006

Taylor, W.R., Canil, D., Milledge, H.J., 1996. Geochim. Cosmochim. Acta 60, 4725.
Tromson, D., Brambilla, A., Foulon, F., Mer, C., Guizard, B., Barrett, R., Bergonzo, P., 2000. Diamond Relat. Mater. 9, 1850.
Wang, L., Lou, Y., Su, Q., Shi, W., Xia, Y., 2005. Opt. Express. 13 (12), 8612.
Wight, D.R., Dean, P.J., Lightowlers, E.C., Mosby, C.D., 1971. J. Lumin. 4, 169.

Please cite this article as: Mavunda, R.D., et al., The presence of defects and their influence on the performance of CVD diamond as an α-particle radiation sensing element. Appl. Radiat. Isotopes (2008), doi:10.1016/j.apradiso.2008.01.006

Article submitted for publication to the journal: Applied radiation and Isotopes

Elsevier Editorial System(tm) for Applied Radiation and Isotopes
Manuscript Draft

Manuscript Number: ARI-D-08-00094

Title: Variations in CVD Diamond Detector's Responses with Crystal Defects at Low Energy Mammographic X-ray Range

Article Type: Full Length Article

Section/Category: Radioactivity and Radiation Measurements

Keywords: Keywords: ESR; Raman; Crystal defects; Thermoluminescence; UV absorption; Mammographic X-ray

Corresponding Author: Professor Tom Leong Nam, PhD

Corresponding Author's Institution: University of the Witwatersrand

First Author: Risimati D Mavunda, MSc (Med)

Order of Authors: Risimati D Mavunda, MSc (Med); Yusuf I Zakari, PhD; Tom L Nam, PhD; Rex J Keddy, PhD

Manuscript Region of Origin: SOUTH AFRICA

Abstract: ABSTRACT
The tissue equivalence of diamond allows for accurate radiation dose determination without large corrections for different attenuation values in biological tissue. The low Z value limits this advantage however, to the lower energy photons. Nine Chemical Vapour Deposition (CVD) diamonds have been analyzed for use as mammography X-ray dosimeters using the linearity, sensitivity and characteristics of the detectors to the photon interaction. The resistivity of each of the diamond grades is calculated from the I-V characteristics of the samples. The diamonds, categorized into four each of, so called, Detector and Optical grade, and a Single Crystal CVD were exposed at low X-ray peak voltage range (22 to 27 kVp) with trans-

crystal polarizing fields of 0.4kV.cm-1, 0.6kV.cm-1 and 0.8kV.cm-1. The crystals were then assayed for further physical characteristics additional to earlier cataloging of their defects reported elsewhere (Mavunda et al., 2008). The response of the CVD diamond wafer as an X-ray dosimeter within the selected energy range was evaluated with the aim of classifying the appropriate CVD type for use in the mammography X-ray energy region.